Università degli Studi di Palermo

AREA RICERCA E TRASFERIMENTO TECNOLOGICO
SETTORE DOTTORATI E CONTRATTI PER LA RICERCA
U. O. DOTTORATI DI RICERCA

Dottorato di Ricerca in Tecnologie e Scienze per la Salute dell'Uomo

Dipartimento di Scienze e Tecnologie Biologiche Chimiche e Farmaceutiche (STEBICEF)

SSD FIS/07

ENGINEERED FERRITIN NANOVECTORS FOR THERANOSTIC APPLICATIONS

LA DOTTORESSA
LUISA AFFATIGATO

IL COORDINATORE
PROF. BRUNO GIUSEPPE PIGNATARO

IL TUTOR
PROF.SSA VALERIA MILITELLO

IL CO-TUTOR
PROF. MARIANO LICCIARDI

CICLO XXXVI

ANNO CONSEGUIMENTO TITOLO 2024

Preface

The research project of this PhD thesis was in collaboration with Prof. Boffi's group of the Sapienza University and was mainly carried out in four laboratories: the Molecular Biophysics Laboratory of the Department of Physics and Chemistry-Emilio Segrè at the University of Palermo; the Preparation and Analysis of Biomaterials Laboratory of ATeN Center at the University of Palermo; the Biochemistry Laboratory of the Department of Biochemistry-A. Rossi Fanelli at the Sapienza University and the Pharmacy Laboratory of the Department of Pharmacy at the University of Copenhagen.

This thesis contains the following research publications:

Affatigato, L., Sciortino, A., Sancataldo, G., Incocciati, A., Piacentini, R., Bonamore, A., Cannas, M., Messina, F., Licciardi, M. and Militello, V. *Engineered Ferritin with Eu^{3+} as a Bright Nanovector: A Photoluminescence Study*. Photochem Photobiol 2023, 99: 1218-1224. https://doi.org/10.1111/php.13759

Affatigato, L.; Licciardi, M.; Bonamore, A.; Martorana, A.; Incocciati, A.; Boffi, A.; Militello, V. *Ferritin-Coated SPIONs as New Cancer Cell Targeted Magnetic Nanocarrier.* Molecules 2023, 28, 1163. https://doi.org/10.3390/molecules28031163

Affatigato, L.; Licciardi, M.; D'Oca M. C.; Cicero, L.; Bonamore A.; Incocciati A.; Macone A.; Buch C. D.; Piligkos S.; van de Weert M.; Foderà, V.; Militello M. *Ferritin-Coated SPIONs as a smart magnetic nanocarrier.* - submitted to Pharmaceutics.

Acknowledgements

My first thanks go to my tutor Prof.ssa Valeria Militello and my co-tutor Prof. Mariano Licciardi for the unique opportunity they gave me to carry out this PhD project under their leadership. Prof.ssa Valeria Militello, with her great scientific knowledge and humanity, always supported and encouraged me. She was my point of reference and she taught me how to discover the world of biophysics and how to connect it with my personal background as a biotechnologist. She gave me the possibility to grow and learn more than I could have imagined or thought. For these reasons, she deserves all my gratitude.

I usually define Prof. Mariano Licciardi as my "scientific father"; he was always available and trained me with patience during the laboratory activities. I will never stop thanking him for making my problems easier with his help and advises.

My next thanks go to Prof. Maurizio Leone, leader of the biophysics group of the University of Palermo, for his teachings and useful suggestions.

My heartfelt thanks go to Prof. Alberto Boffi, Prof.ssa Alessandra Bonamore and the group of the biochemistry laboratory of the Sapienza University; I think that without them I could not have started this journey. I spent two months in their laboratory, but this time was enough to appreciate how the collaboration with them was essential for the entire project. Apart from this, I thank them for their hospitality and availability to introduce me into their group.

I would also thank Dr. Alice Sciortino, Prof. Fabrizio Messina e Dr. Giuseppe Sancataldo, three of the greatest physicists I have ever known. They offered their physical knowledge and tools for the development of my project and the increase of my scientific expertises.

A very special thank goes to Prof. Vito Foderà of the University of Copenhagen, where I spent part of the last year of my PhD project. He gave me the chance to meet fantastic people, not only from a scientific point of view, but also from a human point of view. I am very grateful to all of them for the friendly and positive approach towards me.

Additionally, I would like to show my gratitude to my family, to Michele and to my friends for their daily and continuous support. Also thanks to Winny and Gigi, they taught me to be patient and resilient.

Last, but not least, I express my gratitude towards my curiosity, my desire to know and understand, which have allowed me to overcome the most difficult moments.

Index

List of abbreviations

-AC: alternating current

-AFM: atomic force microscopy

-AfFt: *Archaeglobus Fulgidus* Ferritin

-ATR-FTIR: attenuated total reflection-Fourier transform infrared

-CD: circular dichroism

-DLS: dynamic light scattering

-Dps: DNA-binding proteins from starved cells

-EDX: Energy Dispersive X-Ray

-EPR (chapter 1): enhanced permeability and retention effect

-EPR (chapter 5): electron paramagnetic resonance

-FC: field cooled

-FCC: face-centered cubic

-FDA: Food and Drug Administration

-FRET: Förster resonance energy transfer

-Ft: ferritin

-HFt-LBT: lanthanide binding H-chain ferritin

-HFt-LBT Eu^{3+}: lanthanide Eu^{3+} binding H-chain ferritin

-HFt: heavy ferritin

-HP-SEC: high-performance size-exclusion chromatography

-hTfR1 or CD71: human Transferrin Receptor 1

-HumAfFt: Humanized *Archaeoglobus fulgidus* ferritin

-IONs: irox oxide nanoparticles

-ISO: international organization for standardization

-LBT: lanthanide binding tag

-LFt: light ferritin

-LRET: luminescence resonance energy transfer

-MCF-7: Human breast adenocarcinoma

-MHT: magnetic hyperthermia treatment

-MNPs: magnetic nanoparticles

-MR: magnetic resonance

-MRI: magnetic resonance imaging

-Ms: saturation magnetization

-NHDF: normal human dermal fibroblasts

-NMR: nuclear magnetic resonance

-OLEDs: organic light emitting diodes

-PEG: poly(ethylene glycol)

-RES: reticuloendothelial system

-RF: resonant radiofrequency

-ROS: reactive oxygen species

-SEM: scanning electron microscopy

-SPIONs: superparamagnetic irox oxide nanoparticles

-TE: echo time

-TGA: thermogravimetric analysis

-TR: repetition time

-Trp: tryptophan

-XRD: X-ray diffraction

-ZFC: zero field cooled

Abstract

Nanomedicine is the biomedical application of nanoscale materials for diagnosis and therapy of diseases. Recent achievements in cancer management include the development of highly precise and specific tools for early diagnosis and smart drug delivery systems for targeted delivery into tumor cells. For this purpose, protein-based nanocages have great potential as theranostic devices, used for both diagnostic and therapeutic applications.

Among many nanovectors currently under investigation for biomedical purposes, ferritin has emerged as an excellent and promising nanocage due to its unique architecture, surface properties and high biocompatibility. It can be either genetically or chemically modified for encapsulating therapeutics or probes in its inner cavity. Ferritin H-homopolymers are naturally targeted toward TfR1 (or CD71) receptor highly expressed in iron avid, fast replicating, tumor cells. Only a few ferritin-based constructs have been devoted to design smart fluorescent probes for bioimaging, such as quantum dots gold nanoparticles. For this reason, I employed a new engineered ferritin nanoparticle to facilitate the incorporation of Eu^{3+} ions and create a nanotool with potential applications in bioimaging. Thus, the first part of this research project deals with the study of the interaction between the HFt-LBT and europium ions. HFt-LBT is an engineered H-ferritin nanoparticle carrying a lanthanide binding tag (LBT) at the C-terminal end of each subunit of the ferritin; it is a stretch of 17 aminoacids endowed with strong luminescence resonance energy transfer (LRET) sensitization properties since it has a tryptophan residue that can act as an antenna transferring the absorbed energy to the lanthanide ion. The tag has been designed to be located inside the inner cavity, so the lanthanide ions diffusing through the surface pores could bind to the LBT sequence. The construct would thus act both as carrier targeted to CD71 receptors and as a LRET sensitizer. Steady state emission measurements and time-resolved emission spectroscopy have been employed to investigate the interaction between the HFt-LBT and the Eu^{3+} ions. The results allowed me to identify the Eu^{3+} energy states involved in the process and to pave the way for the future use of HFt-LBT Eu^{3+} complex in diagnostics.

In the second part, I studied another engineered ferritin-based nanotool. It is the complex HumAfFt-SPIONs, made up of the Humanized *Archaeoglobus fulgidus* Ferritin (HumAfFt) used as a coating material for 10 nm SPIONs. Thanks to their intrinsic physicochemical

properties, SPIONs can be used simultaneously as therapeutic and diagnostic agents, and therefore they are considered as a nanotheranostic system. In particular, they attracted a great deal of attention for their potential application in biomedical fields such as cellular labeling, drug delivery, tumor treatment using magnetic hyperthermia and contrast enhancement for magnetic resonance imaging (MRI). The biocompatible coating of SPIONs is essential for most biomedical applications since this increases the stability of the iron oxide core, preventing aggregates formation and allowing functionalization of the surface of the nanoparticles with targeting ligand. For this reason, the HumAfFt was used as a coating material for SPIONs, in order to produce a new magnetic nanocarrier able to discriminate cancer cells from normal cells and maintain the potential theranostic properties of SPIONs. HumAfFt is an engineered ferritin characterized by the peculiar salt-triggered assembly-disassembly of the hyperthermophile *Archaeoglobus fulgidus* ferritin and which is endowed with the human H homopolymer recognition sequence by the CD71. Many biophysical, biological and biochemical techniques were employed to characterize the newly developed HumAfFt-SPIONs. The results indicate that they possess high stability and biocompatibility, making them an excellent theranostic nanotool.

1.Introduction

1.1 Nanomedicine and nanovectors

The development of nanotechnology for biomedical purposes has led to the modern *nanomedicine*, defined as the application of nanomaterials for diagnosis, screening, preventing and treatment of diseases at a molecular level with the help of engineered nanocarriers (Riehemann et al., 2009). It is the result of the convergence of different disciplines, such as biotechnology, medicine and bioinformatics and brought to many outstanding achievements in life science, including applications in drug delivery and *in vivo* therapeutics (H. Lu et al., 2016), diagnostic devices, biomarkers, molecular imaging, regenerative medicine, theranostics, implanted devices and biosensors (Watkins et al., 2015). Tools used in nanomedicine as carrier are called *nanovectors* since their dimensions are in the range of 0.1-100 nm (Joudeh & Linke, 2022). But in general, nanovectors with size <500 nm are considered colloidal drug carrier systems (Din et al., 2017). The reduction in magnitude leads to different, and qualitatively new and advantageous properties in the nanometer-scale materials (Ferrari, 2005; Vogelsberger, 2003; Wittmaack, 2007). Nanocarriers offer several advantages over conventional molecular agents (Peer et al., 2007). Firstly, they enable stable aqueous dispersions of active molecular agents with poor water solubility, making it possible to deliver them in the biological environment. Additionally, their composition, size, shape, and surface can be optimized for better treatment outcomes. Properties can be precisely customized so that, once introduced into the biological environment, they safeguard the encapsulated agents from degradation by several endogenous defense mechanisms (Haley & Frenkel, 2008; Torchilin, 2001). Nanovectors can be directed towards specific organs or tissues in the body, even at a cellular and subcellular level, by controlling their size, shape, and surface properties. Another significant advantage is that a nanocarrier matrix can be designed to release drugs in a controlled manner, targeting specific areas for optimal and sustained drug efficacy (Slowing et al.,

2008). New approaches using nanocarriers have overcome most of the limitations of conventional drug approaches, such as low drug stability, low solubility, short half-life, cytotoxicity, narrow therapeutic index, poor pharmacokinetic and pharmacodynamic parameters (Abuelezz et al., 2020). The first generation of nanoparticle therapeutics consists of lipid-based systems such as liposomes, which were approved by the Food and Drug Administration (FDA) more than two decades ago (Patra et al., 2018). Researchers have created a range of smart nanoparticles that are capable of targeting and regulating drug distribution through various external stimuli, such as light, temperature, or magnetic fields, as well as internal factors such as enzyme, pH, or redox signals (Bonifácio et al., 2013).

The combination of nanotechnology and imaging leads towards a revolution in the so-called *nanoimaging*, enabling the detection of a specific molecule or cell in the complex biological media (H. Lu et al., 2016). As diagnostic instruments, nanoparticles can be designed to have different contrast properties (e.g. magnetism, fluorescence, radioactivity) (Cho, 2020).

A new nanovector should be able to reach the targeted site, exploiting the biochemical and metabolic differences between "diseased" and "healthy" cells. There are two different types of targeting, the passive and the active targeting (Haley & Frenkel, 2008) (Figure 1.1). The former relates to the enhanced permeability and retention effect (EPR), that is caused by the increased angiogenesis in tumors, leading to aberrant and defective tumor vasculature (H Maeda et al., 2000; H. Maeda et al., 2009). The epithelial cells in the wall of tumor blood vessels are very sparse, which creates larger pores in the tumor epithelium than those common in the healthy blood vessels and the tumor vasculature becomes leaky (Shi et al., 2017). This provides the tumor with sufficient supply of oxygen and nutrients. Due to their small size, nanocarriers can easily enter the tumor mass through these openings in the epithelium. Additionally, many solid tumors show a notable deficiency in lymphatic vessels, this allows the nanocarriers to persist in the tumor mass for prolonged time. EPR is optimal if the nanocarriers succeed to escape the immune system and therefore circulate for a prolonged period. For this purpose, nanocarriers should have one of these three properties: (a) they should have dimensions between 10 nm and 100 nm; more specifically, they should be smaller than 500 nm to penetrate the tumor epithelium; (b) their charge surface should be neutral or negative to avoid the renal filtration; (c) they should avoid the reticuloendothelial system (RES), which destroys any foreign material (Gullotti & Yeo, 2009; Malam et al., 2009).

The EPR effect is highly dependent on the intrinsic tumor biology and in particular: (a) the degree of angiogenesis and lymphangiogenesis; (b) the degree of perivascular tumor growth

and the density of the stromal response and (c) intratumor pressure. All of these factors, together with the physicochemical features of nanocarriers, will determine its drug delivery efficiency (Gavas et al., 2021).

Instead, the active targeting is based on the decoration of the nanocarrier surfaces with ligands binding to receptors overexpressed onto the targeted cells (Gao et al., 2005). This strategy will improve the affinities of the nanocarriers for the surface of cancer cell and thus enhance the drug penetration (Byrne et al., 2008). The first evidence of this phenomenon was proposed in 1980 with antibodies grafted in the surface of liposomes, followed by other various kinds of ligands such as peptides, nucleic acids and aptamers (Heath & Bicknell, 2009). Among the common ligands, there are antibodies, sugary portions, transferrin and folate residues. The latter two are currently employed to target biological molecules towards cancerous cells, as they often exhibit an overexpression of specific receptors for folate and transferrin on their surface (Argenziano et al., 2021). When designing ligand-functionalized targeted nanovectors, it is important to consider the essential ligand parameters, including molecular weight (MW), targeting affinity and biocompatibility (D. Fan et al., 2023). The latter is a crucial parameter because many active targeting nanovectors are highly effective *in vitro*, but they do not always increase drug accumulation in tumors when applied *in vivo*.

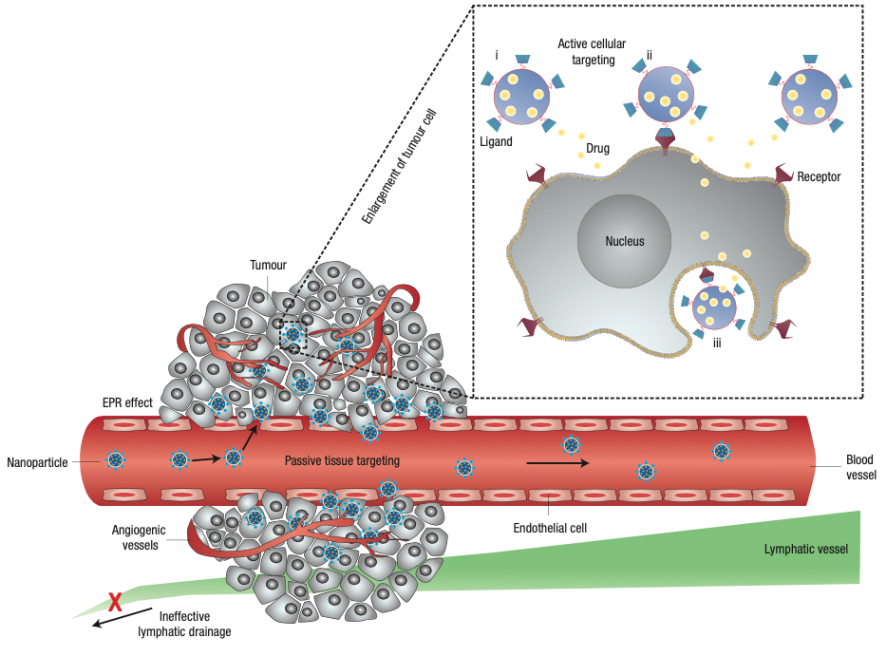

Figure 1.1 Schematic representation of passive and active tissue targeting. In the passive cellular targeting, nanoparticles enter the tumor mass through the increased permeability of the tumor vasculature and ineffective lymphatic drainage (EPR effect). Instead, active cellular targeting (inset) can be achieved by functionalizing

the surface of nanoparticles with ligands that promote cell-specific recognition and binding (adapted from (Peer et al., 2007)).

1.2 Types of nanovectors

Based on the discovery of all advantages that nanocarriers can provide for personalized treatment, a widespread search has ensued to find the ideal nanocarrier. A range of materials has been investigated with varied levels of success, including both inorganic and organic materials, as well as natural and synthetic ones. Owing to their high surface-area-to-volume ratio, it is possible to achieve high ligand density on the surface for targeting purposes. Nanocarriers can also be used to increase local drug concentration by carrying the drug within and control-releasing it when bound to the targets. Currently, natural and synthetic polymers and lipids are typically used as drug delivery vectors. The family of nanovectors includes polymer conjugates, polymeric nanoparticles, lipid-based carriers such as liposomes and micelles, dendrimers, carbon nanotubes, and gold nanoparticles, including nanoshells and nanocages (Figure 1.2).

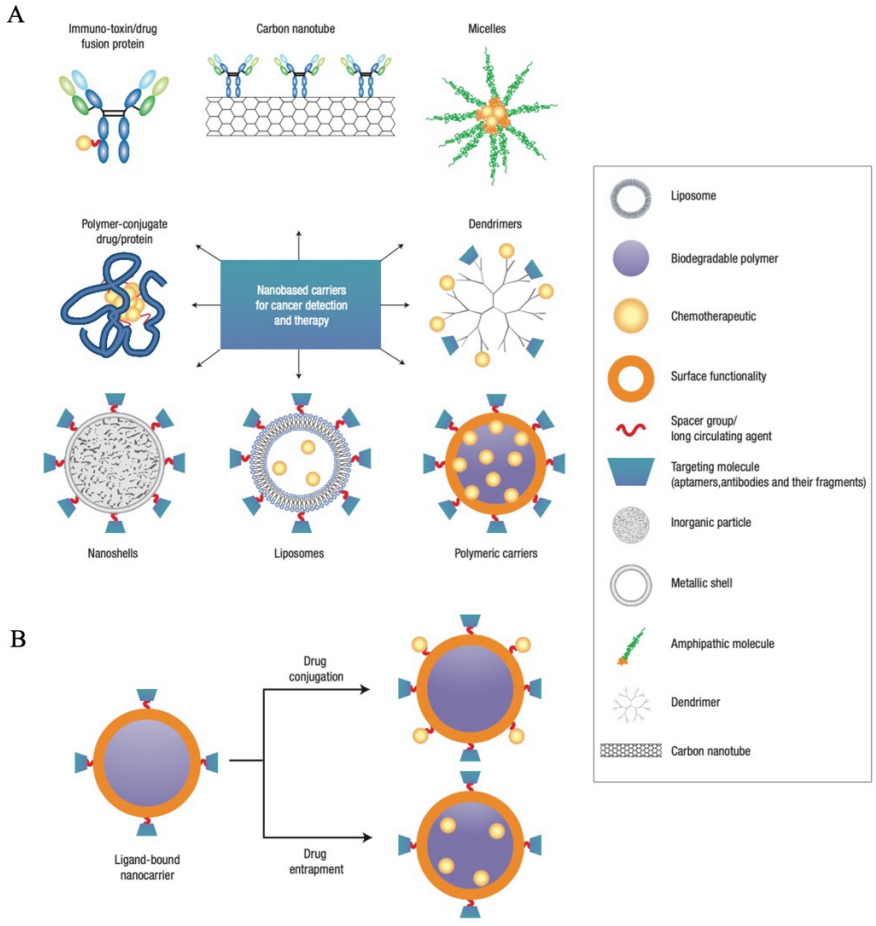

Figure 1.2 Examples of nanocarriers for targeting cancer. (A) A whole range of delivery agents are possible, but the main components typically include a nanocarrier, a targeting moiety conjugated to the nanocarrier,

and a cargo. (B) Schematic diagram of the drug conjugation and entrapment processes. The cargo could be bound to the nanocarrier, as in the use of polymer–drug conjugates, dendrimers and some particulate carriers, or they could be entrapped inside the nanocarrier (adapted from (Peer et al., 2007)).

These nanocarriers have been explored for a variety of applications such as drug delivery, imaging, photothermal ablation of tumors, radiation sensitizers, detection of apoptosis, and sentinel lymphnode mapping (Duncan, 2006; Ferrari, 2005; LaVan et al., 2003).
Nanovectors in which the lengths of the longest and the shortest axes do not differ significantly are defined nanoparticles by the International Organization for Standardization (ISO). Based on their composition, nanoparticles are generally placed into three classes: organic, carbon-based, and inorganic (Ealias & Saravanakumar, 2017). Organic nanoparticles are made of lipids, carbohydrates, proteins, polymers or any other organic compounds (K. Pan & Zhong, 2016). Examples of this class of nanoparticles are liposomes, micelles, dendrimers and protein complexes such as ferritin (Figure 1.3). These nanoparticles are generally non-toxic, biodegradable and, in some cases, have a hollow core. They are susceptible to thermal and electromagnetic radiation, such as heat and light (Ealias & Saravanakumar, 2017). Different parameters determine the potential applications of organic nanoparticles, such as stability, composition, surface morphology, carrying capacity. Organic nanoparticles are currently widely used in the biomedical field for cancer therapy (Gujrati et al., 2014) and targeted drug delivery.

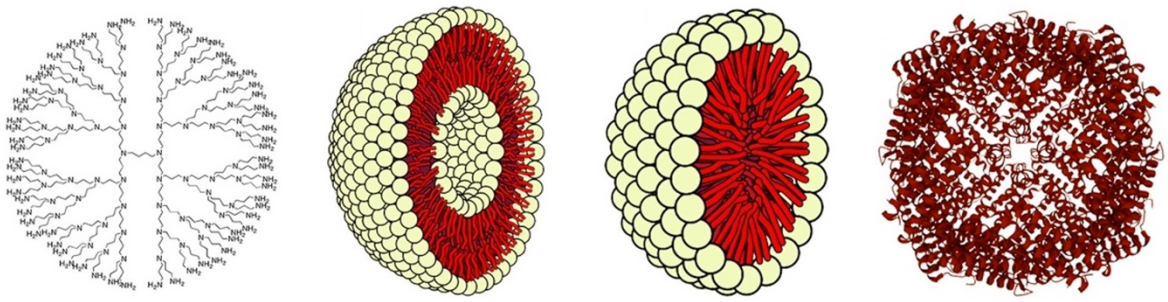

Figure 1.3 Types of organic nanoparticles (from left to right): dendrimers; liposomes; micelles and ferritin (adapted from (Joudeh & Linke, 2022)).

Carbon-based nanoparticles include nanoparticles made exclusively from carbon atoms. Well-known examples of this class are fullerenes, carbon black nanoparticles, and carbon quantum dots (Figure 1.4). Fullerenes are carbon molecules with a symmetrical closed-cage structure (Long et al., 2013). Carbon black nanoparticles consist of grape-like clusters of

closely fused spherical particles (Yuan et al., 2019). Carbon quantum dots are composed of discrete, quasi-spherical carbon nanoparticles with sizes below than 10 nm (K. Q. Lu et al., 2016). They have unique electrical conductivity, high strength, electron affinity, optical, thermal and sorption properties (Khan et al., 2019; Mauter & Elimelech, 2008), so they are used in a wide range of application, such as bioimaging (Chandra et al., 2011), drug delivery (Oh et al., 2010), energy storage (Liu et al., 2018), photovoltaic devices and environmental sensing applications used to monitor both microbial ecology and detect microbial pathogens (Mauter & Elimelech, 2008).

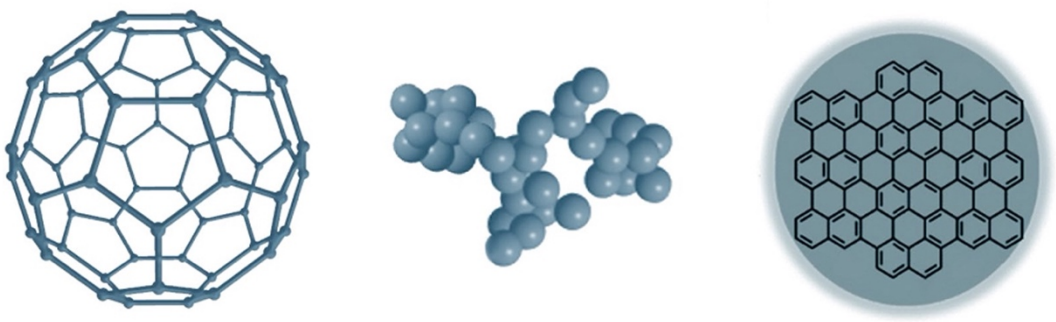

Figure 1.4 Different types of carbon-based nanoparticles (from left to right): C_{60} fullerene; carbon black nanoparticles; and carbon quantum dots (adapted from (Joudeh & Linke, 2022)).

Inorganic nanoparticles comprise nanoparticles that are not composed of carbon or organic materials. Metal, ceramic, and semiconductor nanoparticles are representative examples. Metal nanoparticles are entirely made of metal precursors and can be monometallic, bimetallic (Toshima & Yonezawa, 1998) or polymetallic (Nascimento et al., 2018). Owing to their localized surface plasmon resonance features, these nanoparticles possess distinctive optical and electrical properties (Khan et al., 2019). Furthermore, some metal nanoparticles exhibit unique thermal, magnetic and biological characteristics (Ealias & Saravanakumar, 2017), thereby making them important materials for nanodevice development in a variety of physical, chemical, biological, biomedical and pharmaceutical applications (Mody et al., 2010). Currently, the controlled synthesis of metal nanoparticles is crucial for making advanced materials. Semiconductor nanoparticles are composed of semiconductor materials that possess properties located between metals and non-metals. These particles own distinct wide bandgaps and display notable changes in their properties with bandgap tuning compared to bulk semiconductor materials (Khan et al., 2019). For these reasons, they are important materials in photocatalysis, optic and electronic devices (S. Sun et al., 2000).

Ceramic nanoparticles are inorganic solids composed of carbonates, carbides, phosphates and oxides of metals and metalloids, such as titanium and calcium. They are usually synthesized through heating and gradual cooling and they can be found in dense, polycrystalline, amorphous, porous or hollow forms. They have a primary application in biomedical settings due to their exceptional stability and high load capacity (Moreno-Vega et al., 2012). However, they also find employ in fields such as catalysis, degradation of dyes, photonics, and optoelectronics (D'Amato et al., 2013).

1.3 Theranostics

The application of nanomedicine has gained significant interest as a versatile strategy for selective drug delivery and diagnostic purposes. The encouraging results obtained with monofunctional nanomedicines have directed scientists' efforts towards the creation of "nanotheranostics" (theranostic nanomedicines) that integrate imaging and therapeutic functions in a single platform (Ryu et al., 2014). Nanotheranostics hold great promises because they combine the simultaneous non-invasive diagnosis and treatment of diseases with the exciting possibility to monitor in real time drug release and distribution, thus predicting and validating the effectiveness of the therapy (Figure 1.5). Due to these features, nanotheranostics are extremely attractive for optimizing treatment outcomes in cancer and other severe diseases. Although theranostic nanomaterials share the same goal, they can have different features due to their physical-chemical, optoelectronic and magnetic properties, as well as the precise design of the smart nanodevice. Among the most promising theranostic tools proposed in recent literature panorama, gold nanoparticles, superparamagnetic iron oxide nanoparticles (SPIONs), carbon nanodots and graphene oxide have shown intriguing features exploitable in biomedicine and especially in cancer theranostics. SPIONs have been explored as efficient contrast agents in cancer magnetic resonance imaging (MRI) combined to chemo- and magnetotherapy (Hayashi et al., 2013). The viewpoint is that SPIONs can be accumulated into the tumor mass through magnetic targeting under the guidance of external static magnetic fields, and simultaneously used to release anti-cancer drugs and heat by using alternated magnetic fields directly in the site of action.

Polymer-coated iron oxide nanoparticles (IONs) are one of the few FDA-approved nanomaterials that have been used in humans as MRI contrast agents (L. Johnson et al., 2013). With appropriate targeting ligands and surface modifications, an enhanced accumulation of IONPs in tumor tissues by passive or active targeting has been shown in

animal tumor models while significantly reducing nonspecific accumulation in the liver and spleen (Chen et al., 2013; Yu et al., 2012). Therefore, IONPs are excellent candidates for the development of new tumor imaging, targeted drug delivery and image-guided therapy that have the potential for novel clinical applications.

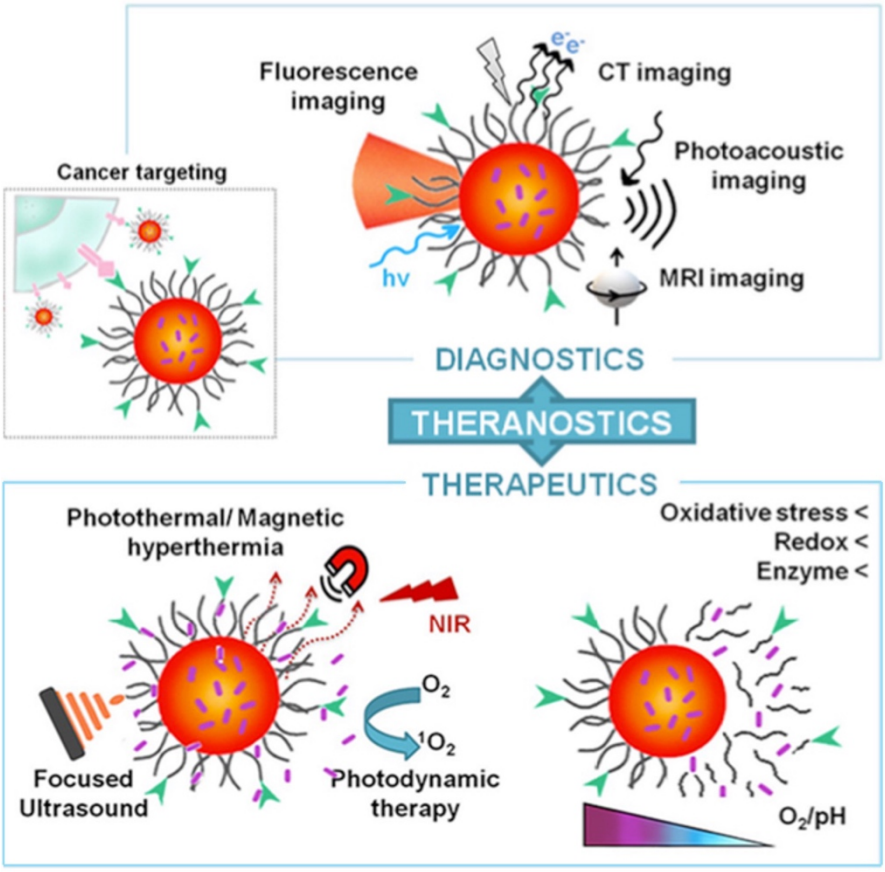

Figure 1.5 Schematic representation of the "theranostics". Nanoparticles with theranostic properties are designed to be accumulated at the target site for imaging, monitoring, and treatment of the disease. Various therapeutic and diagnostic approaches can be combined for multimodal clinical diagnosis and precise treatment (adapted from (Mauro et al., 2021)).

1.4 Iron Oxide Nanoparticles (IONs)

Inorganic nanoparticles combine chemical accessibility in solution with the physical properties of the bulk phase, acting as intermediates between the molecular and solid states. They are therefore perfect elements for the creation of nanostructured materials and devices with adjustable physical and chemical properties.

The application of small iron oxide nanoparticles in in vitro diagnostics has been practiced for nearly 40 years. Over the past decade, many investigations with several types of iron oxides have been carried out in the field of nanosized magnetic particles, focusing on

maghemite (Fe_2O_3) and magnetite (Fe_3O_4), among which magnetite is a very promising candidate since its biocompatibility has already proven (Gupta et al., 2007). Magnetite is a common magnetic iron oxide that has a cubic inverse spinel structure with oxygen forming a face-centered cubic (fcc) closed packing and Fe cations occupying interstitial tetrahedral sites and octahedral sites (Mahmoudi et al., 2011) (Figure 1.6).

The electrons are capable of transitioning between Fe^{2+} and Fe^{3+} ions in the octahedral sites at room temperature, making magnetite an important class of half-metallic materials.

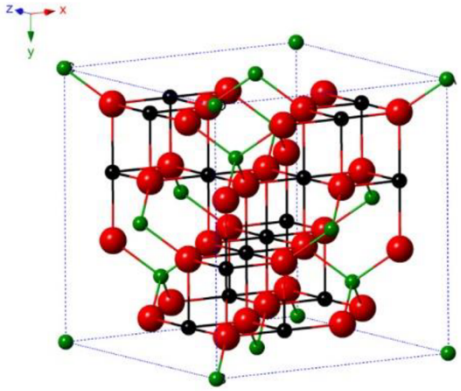

Figure 1.6 Crystal structure of magnetite.

With the appropriate surface coating, magnetic nanoparticles can be dispersed into suitable solvents, resulting in homogeneous suspensions known as ferrofluids (Babincová et al., 2001; Sharifi et al., 2015; Y. X. J. Wang et al., 2001). This suspension can interact with an external magnetic field and be positioned in a specific area, which can facilitate magnetic resonance imaging for medical diagnosis and alternating current (AC) magnetic field-assisted cancer therapy (Bonnemain, 1998).

Iron oxide particle materials are classified by their response to an externally applied magnetic field. Description of orientations of the magnetic moments in a particle helps to identify different types of magnetism observed in nature. The magnetic properties of these particles can be described by the dependence of the magnetic induction B on the magnetic field H (Gupta & Gupta, 2005). Some materials such as iron exhibit *ferromagnetism*, in that they can be permanently magnetized. In most materials the relation between B and H is linear: $B=\mu H$, where μ is the magnetic permeability of the particles. Iron oxide particles exhibit *paramagnetism* if $\mu>1$ and diamagnetism if $\mu<1$. In vacuum, $\mu=1$. One significant advantage of magnetic nanoparticles is their *superparamagnetism*, which allows their stability and dispersion after the magnetic field has been removed as there are no residual magnetic forces between the particles. With particles smaller than 15 nm the cooperative phenomenon of

ferromagnetism is no longer observed, resulting in a lack of permanent magnetization after exposure to an external magnetic field. However, the particles retain highly strong paramagnetic characteristics with a very large susceptibility. Superparamagnetic iron oxide nanoparticles with higher saturation magnetization have better sensitivity for the Magnetic Resonance Imaging (MRI) detection, given stronger contrast enhancement, typically, sharply reducing the transverse relaxation time, or T_2, of the surrounding water.

Ferromagnetic particles are those whose unpaired electron spins spontaneously align, allowing the material to exhibit magnetization without requiring a magnetic field. Ferromagnetism is a cooperative phenomenon, as individual atoms are unable to exhibit ferromagnetism. However, when a specific number of atoms are bound together in solid form, ferromagnetic properties emerge. Once the ferromagnetic particles are removed from the field, they display permanent magnetization. Upon field reversal, the ferromagnetic material will initially resist the change field. However, many domains will switch their magnetization vectors, resulting in the attainment of the same reverse magnetization. When ferromagnetic materials are ground down to particle sizes smaller than a certain domain, they no longer exhibit ferromagnetism. Instead, they show superparamagnetism. When dealing with paramagnetic particles, any magnetic materials present within the magnetic field will alter it. If a particle has magnetic moments that can be aligned within an external magnetic field, this will amplify the field. These types of substances demonstrate the property of paramagnetism. Unlike ferromagnetic materials, paramagnetic materials do not retain a permanent magnetization when they are removed from the magnetic field. Paramagnetism can be understood by postulating permanent atomic magnetic moments that can be reoriented in an external field. The torque exerted by an external magnetic field on these moments will tend to align them parallel to the field, thereby strengthening it. Particles composed of iron oxide exhibit distinct behavior in the presence of a magnetic field depending on their size. Many researchers have previously reported that modifications in the magnetic properties of these particles tend to occur upon reducing their size to the nanometer range from micrometers (Bedanta & Kleemann, 2009; Lefebure et al., 2014). For instance, particles exhibit superparamagnetic behavior when their size is sufficiently small (6-15 nm), whereas they behave as ferromagnetic when the grain size is in the micrometer range. The magnetic behavior is dependent on the blocking temperature of the particles, which in turn depends on their size (Chatterjee et al., 2003). The blocking temperature represents the transition temperature between the ferrimagnetic and superparamagnetic states and is directly proportional to the size of the particle. Particles possessing a lower blocking

temperature show superparamagnetic properties, whereas the higher blocking temperature of the particles display the ferromagnetic behavior of the particles. Although the superparamagnetic behavior of particles increases with decreasing particle size, various authors have observed a decrease in absolute saturation magnetization (Ms) values when the particles are reduced to less than 10 nm (Han et al., 1994; Y. Li et al., 2002). Surface modification of iron oxide nanoparticles often results in the creation of a non-magnetic shell, due to the formation of an outer particle layer, typically with a thickness ranging from 1-20 nm (Tourinho et al., 1990). Coating particles with non-magnetic materials can lead to a decrease in Ms values (Gómez-Lopera et al., 2001). Some researchers found that surface coverage of the iron oxide with certain types of polymers resulted in decreased saturation magnetization values of the particles. They also noted that the magnetization data yielded smaller particle size values compared to those obtained through XRD and TEM measurements. This difference may be due to the presence of a magnetically inefficient layer on the surface of the particles (Sjgren et al., 1997).

1.4.1 Applications of Superparamagnetic iron oxide nanoparticles (SPIONs)

Thanks to their unique physical, chemical, thermal, and mechanical properties, superparamagnetic nanoparticles offer a high potential for several biomedical applications, such as (Arbab et al., 2003; Pankhurst et al., 2003): cell labeling and targeting to separate and purify certain cell populations; tissue repair; drug delivery; magnetic resonance imaging (MRI); hyperthermia and magnetofection (Figure 1.7).

Cell labelling with ferro/paramagnetic substances is becoming a more prevalent technique for *in vivo* cell separation (Olsvik et al., 1994), as the labelled cells can be identified via MRI (Yeh & Zhang, 1993). Most current labelling methods employ either of two approaches: (a) attaching magnetic particles to the cell surface (Handgretinger et al., 1998), or (b) internalizing biocompatible magnetic particles through receptor-mediated endocytosis (Schoepf et al., 1998). One approach for efficient and specific cell labelling of magnetic particles is to modify the nanoparticle surface using a ligand that is effectively internalized by target cells through receptor-mediated endocytosis. A range of ligands have been attached to the surfaces of nanoparticles to promote receptor-mediated endocytosis of the particles, including monoclonal antibodies (Weissleder et al., 2005). Targeting agents such as transferrin, lactoferrin, albumin, insulin, and growth factors have been shown to preferentially target the cell surface since the receptors for these ligands are frequently

expressed on the surface of mammalian cells (Ming Qian & Sun, 2002). These receptors are not only cellular markers, but they have also demonstrated an efficient internalization of molecules that are linked to these receptors.

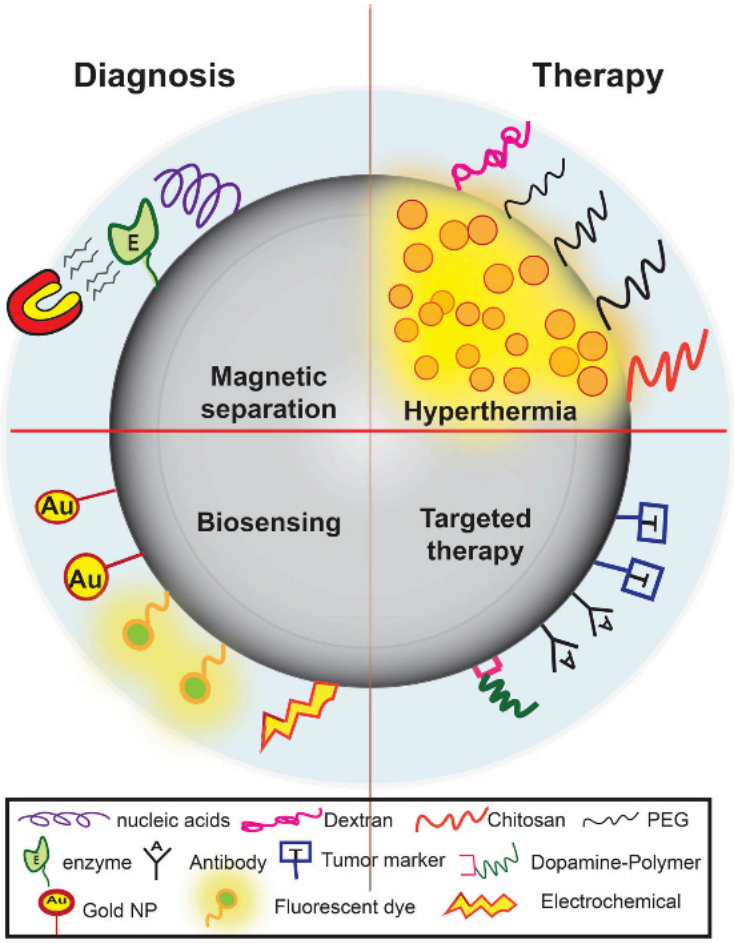

Figure 1.7 Different applications of magnetic nanoparticles in nanomedicine fields such as selective separation of specific cells, treatment with hyperthermia, surface functionalization for targeted drug delivery and incorporation with enzymes and gold nanoparticles for diagnosis (adapted from (Abdel-Mageed et al., 2021)).

Another promising application of these colloidal magnetic nanoparticles is drug delivery, acting as carriers for site-specific drug delivery. They could carry on their surface or in their bulk a pharmaceutical drug which could then be transported to the target organ and released there. For these applications, the properties of the nanoparticles, such as the size, the charge and surface chemistry are very important, since they strongly affect both the blood circulation time and the bioavailability of the particles in the body (Choulyt et al., 1996). Furthermore, magnetic properties and internalization of particles are greatly influenced by the size of the magnetic particles (Chatterjee et al., 2003). For example, particles with diameters larger than 200 nm are captured by the spleen via mechanical filtration and are

subsequently cleared by the phagocyte system, leading to reduced blood circulation times. Instead, smaller particles with diameters of less than 10 nm are quickly eliminated via extravasations and renal clearance. Particles ranging from approximately 10 to 100 nm are the most suitable for intravenous injection and exhibit the longest blood circulation times. Particles in this size range are small enough to avoid the reticuloendothelial system (RES) of the body and penetrate the tiny capillaries within the body tissues, allowing for optimal distribution in specific tissues (Pratsinis & Vemury, 1996). Small SPIONs are easily produced and coated with different types of polymers, providing convenient, readily targetable magnetic resonance imaging agents. Due to the high surface area to volume ratio, magnetic nanoparticles tend to agglomerate and adsorb plasma proteins. The RES of the body, particularly the Kupffer cells in the liver, usually uptake these nanoparticles because of their hydrophobic surface. Surface coverage with amphiphilic polymeric surfactants including poloxamers, poloxamines and poly(ethylene glycol) (PEG) derivatives on the nanoparticles significantly enhances blood circulation time by reducing or eliminating protein adsorption to the nanoparticles (Storm et al., 1995). Different methods for preparing colloidal particles formed by a magnetite nucleus and a biodegradable polymer coating have been developed. The aim in all cases was to obtain, in a reproducible and rather simple way, colloidal particles that were both magnetic field responsive, and useful as drug delivery systems. For this purpose, the structure, chemical composition, and surface properties of the composite particles have been compared with those of the nucleus and the coating material. Considerable works that demonstrate that biodegradable polymers are ideal as drug carriers because of their minimum toxicity and immunological response have been performed (Chilkoti et al., 2002; Najafi & Sarbolouki, 2003; Otsuka et al., 2003).

SPIONs play an important role as MRI contrast agents. MRI uses nuclear magnetic resonance (NMR) to produce high-resolution images of the internal structure of the body. Every tissue contains 70 to 90 percent water which in turn contains hydrogen proton molecules; the protons are randomly oriented in the absence of an external magnetic field. Most diseases are associated with an increase in the water content of the body. So, MRI is a sensitive test for the detection of disease. To obtain an image, a patient or biomedical sample is placed inside the MR scanner. An MRI system consists of a main magnet, gradient coils, radio frequency coils and a computer system that controls and interfaces various components. The object placed inside the scanner is exposed to an external magnetic field, typically ranging from 0.5 to 3 Tesla in clinical settings and up to 10.5 Tesla in research studies. This process aligns the magnetic poles of water protons with the field. The images

are created by determining proton relaxation in the presence of an external magnetic field. The orientation of the hydrogen nuclear spins in the presence of a strong magnetic field is parallel or antiparallel to the direction of the magnetic field. Resonant radiofrequency (RF) irradiation increases the number of protons in the high-energy state by transferring energy to them. After the pulsing field stops, the magnetic moments (spin) of protons return to their original state, a process known as relaxation (Nelson et al., 2020).

Transverse magnetization decay (T_2-decay) and longitudinal magnetization recovery (T_1-recovery) are two distinct relaxation processes. T_1 is the amount of time required for the longitudinal magnetization to return to equilibrium, whereas T_2 is the amount of time required for the transverse magnetization to exponentially decrease to 37% of its initial magnitude. In other words, the T_1 relaxation time refers to the rate at which excited spinning protons return to equilibrium and realign with the external magnetic field. The T_2 relaxation time is the rate at which excited protons lose coherence with each other. Repetition time (TR, or the amount of time between radiofrequency pulse replication) and echo time (TE, time between the radiofrequency pulse and the first signal measurement) are two crucial variables that influence signal intensity and image contrast. Keeping TR and TE values appropriate can help produce clearer images. It is important to ensure that the TR and TE values are set correctly to achieve the desired image quality. For T_1-weighted images, short times are considered to be TE (<10 ms) and TR (<250 ms), while long TE (>60 ms) and long TR (>2000 ms) are used to create images for the T_2 state.

Different tissues have different contrasts (Zarepour et al., 2017). Tissues with a short T_1 appear bright in MRI images, while those with a short T_2 appear dark. A T_1-weighted scan displays all fat deposits as high-intensity pixels in the image. A T_2-weighted scan displays all fat and water as high-intensity pixels. These two types of images are used together to map organs and diagnose diseases. Most tissues do not have enough inherent T_1 and T_2 relaxation capabilities, and this can affect the quality of the images. For this reason, exogenous contrast agents are used to enhance the relaxation time and improve image visibility. Relaxivity (R_1 and R_2) is a feature that has an impact on the effectiveness of a contrast agent and is defined as the change in the relaxation rate of solvent water protons ($R_1 = 1/T_1$ and $R_2 = 1/T_2$) in the presence of a contrast agent. The most used contrast agents are paramagnetic compounds, particularly gadolinium. Gadolinium is a frequently used (T_1) contrast agent that shortens the T_1 relaxation period, increasing signal intensity and resulting in brighter (T_1-weighted) images (Zarepour et al., 2017). However, the low sensitivity and potential toxicity of gadolinium-based contrast agents have prompted the search for new contrast materials.

SPIONs represent the latest contrast agent combining magnetic contrast agent and nanotechnology. They are used as T_2 contrast agents, but their properties can be engineered and also used as T_1 contrast agent (Rosa et al., 2017). SPIONs with a diameter of less than 20 nm have a single domain of electrons that spin in the same direction. Instead, SPIONs larger than 20 nm contain numerous domains of electrons that spin in opposite directions (Cortajarena et al., 2014). Therefore, compared to other paramagnetic materials, SPIONs exhibit a stronger magnetic susceptibility to external magnetic fields. When the external magnetic field is removed, SPIONs also have the capability of demagnetization, which is crucial for biomedical applications. Since SPIONs produce localized heterogeneities in presence of external magnetic field, this affects the images. On T_2-weighted images, this reduces their signal, giving the IONPs to look dark (Cortajarena et al., 2014).

Magnetic hyperthermia treatment (MHT) is a promising cancer thermotherapy because magnetic materials produce heat under AC magnetic fields (Laurent et al., 2011). MHT allows the local treatment of tumors without damaging normal tissue, because tumors are more susceptible to heat and can be heated more easily than normal tissue. The number of surviving cancer cells decreases gradually below 42°C, but decreases rapidly above 42°C. When magnetic particles are subjected to an alternating magnetic field, heat is generated due to the magnetic hysteresis loss. The amount of the generated heat depends on the magnetic properties of the material and the field parameters. When exposed to an AC magnetic field, magnetic particles are absorbed by tumor cells, that heat up. The temperature reached depends on the magnetic properties of the material, the strength of the magnetic field, the oscillation frequency and the cooling capacity of the blood flow at the tumor site.

The combination of magnetic drug targeting and gene delivery is known as magnetofection, which shows great potential. This method is simple and efficient for the delivery of genetic material to cells through the use of magnetic nanoparticles that are manipulated by an external magnetic field. For this purpose, SPIONs should be coated with polycations, such as polyethylenimine (Estelrich et al., 2015). The term “magnetofection” refers to the use of a magnetic field and magnetic particles to improve the efficiency of gene delivery (Mah et al., 2002). Compared to conventional transfection based on polymers or lipids, magnetofection benefits from a number of obvious advantages, such as a higher efficiency and, consequently, a lower required dose of nucleic acid, shorter delivery time, and the ability to transfect locally and in a limited area (Castellani et al., 2016; Plank et al., 2011; Song et al., 2010). It is known that poly(lactic-co-glycolic acid) and polyethylenimine (PLGA-PEI)-coated magnetic nanoparticles as a nonviral gene vector can self-assemble DNA, and they

are more stable, easier to manipulate, and more economic than cationic liposomes (S. Pan et al., 2013).

1.5 Ferritin

Ferritin (Ft) is a globular protein ubiquitously distributed in vertebrates, invertebrates, plants and fungi; even bacterial species possess their type of Ft, although it has evolved independently. The function of Ft is centered around intracellular iron storage and transport (Bogdan et al., 2016). Iron metabolism is crucial for physiological processes, as this element has both toxic and beneficial properties for cellular health. A tightly controlled regulation of iron metabolism is vital. Iron is a cofactor for many biochemical reactions, including oxygen transportation, energy metabolism and DNA synthesis, but unbound Fe(II) is toxic (Silva & Faustino, 2015). When interacting with free oxygen, at neutral pH it generates reactive oxygen species (ROS) (Bou-Abdallah, 2010). Free ROS are destructive to cells; due to their extremely reactive nature, they can damage enzymes, membrane lipids, proteins and nucleic acids. Moreover, under physiological conditions, Fe(III) is predominantly insoluble and precipitates as Fe(III) oxide species. To prevent these harmful effects, Fe(II) is consistently bound to a protein ligand, such as Transferrin (Tf) or Ferritin (Bogdan et al., 2016). Ferritin binds and oxidizes Fe(II) to Fe(III) through the ferroxidase reaction (Bou-Abdallah, 2010). It is stored inside the internal cavity of Ft in the form of the crystalline mineral ferrihydrite: the shell can encapsulate up to 4500 Fe^{3+} atoms.

The mammalian Ft is the product of self-assembly of 24 subunits of two different types (Sammarco et al., 2008): LFt ("light" Ferritin, 20 kDa) and HFt ("heavy" Ferritin, 22 kDa). The assembled 24-mer has a total weight of ≈500 kDa with an outer diameter of roughly 12 nm and an inner diameter of 8 nm (Figure 1.8)

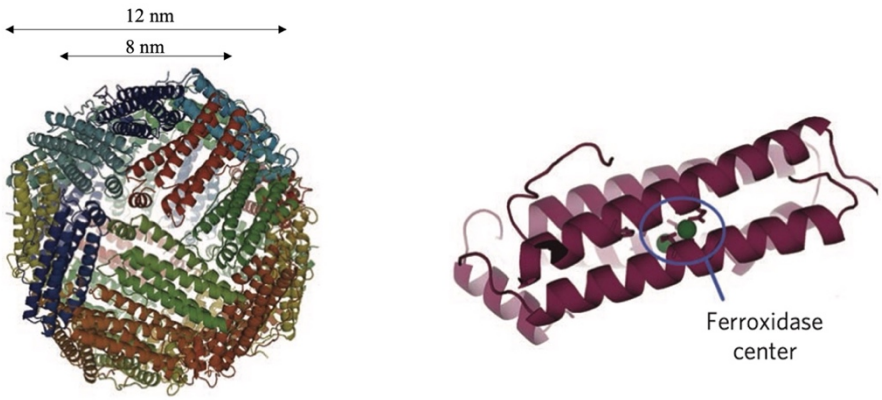

Figure 1.8 Structure of ferritin with 24 subunits and the four α-helical bundle structure of one subunit with the catalytic iron center in its middle (adapted from (Honarmand Ebrahimi et al., 2012)).

The distribution of H and L subunits in Ferritin molecules varies in different tissues: H subunits are predominantly present in the heart, during early development and in cancerous tissues, while L subunits are mainly found in the liver and spleen (Sammarco et al., 2008). It is crucial to note that only H subunits are capable of catalyzing the oxidation of Fe(II) (Honarmand Ebrahimi et al., 2012). The conformation of each subunit consists of a 4-helix bundle of alpha helices: A, B, C, D; a fifth helix, E points towards the internal cavity of the three-dimensional protein. A long loop L connects B and C helices (Figure 1.9).

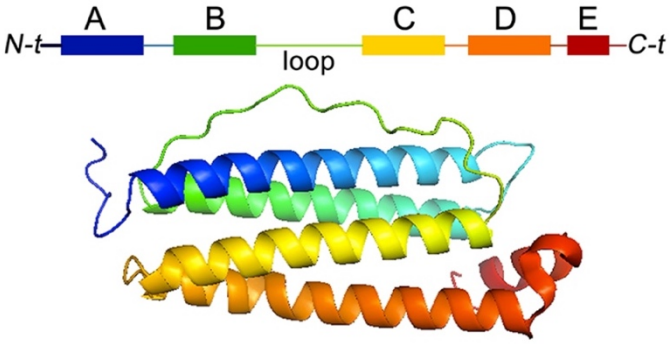

Figure 1.9 Tertiary structure of one subunit of ferritin shows four α helices forming a bundle and a short C-terminal α helix (adapted from (Honarmand Ebrahimi et al., 2015)).

The symmetrical junction of three or four monomers in the protein shell results in the formation of several channels (6 hydrophobic channels at the 4-fold symmetry axis and 8 hydrophilic canals at the 3-fold axis intersections) connecting Ft inner cavity to the outside. These channels have a broad selectivity, binding Fe^{2+} and other cations such as Tb^{3+}, Cd^{2+}, and Zn^{2+} in the 3-fold channels (Price & Joshit, 1983). Specific active sites, known as ferroxidase centers, catalyze the Fe(II) oxidation to Fe(III), and they are located in every monomer between A and B helices of the HFt (Figure 1.8). Their residues have a very high sequence homology in the three domains of nature (Honarmand Ebrahimi et al., 2012). Despite the available information regarding the amino acids involved in iron binding, the mechanism of the the ferroxidase center remains unclear. Furthermore, the method of Fe(II) translocation from the 3-fold channels to the ferroxidase site is not yet understood (Honarmand Ebrahimi et al., 2012). Thus, Ft is made up of flexible structures that allow different ions and molecules to enter and exit through the protein shell. However, this flexibility does not compromise its quaternary structure, which displays remarkable stability due to the many intersubunit interactions like salt bridges, H-bonds, and apolar interactions between the monomers. As a result, the cage is resistant to denaturants and to high temperatures (even above 80°C) (Truffi et al., 2016). Subunits can be dissociated from the tetraicosameric structure only by reaching pH values below 3 or above 10. Once the pH

returns to neutrality, the monomers reassemble spontaneously in a shape memory manner. In the self-assembly of the 24-meric shell, the initial stable intermediate appears to be a dimer (Stefanini et al., 1987), through the interaction of the respective BC loops. It has been shown that deletion of two residues in the loop prevents the formation of the whole 24-mer. Although this pH-dependent assembly is currently widely studied, the kinetic pathway from dimers to the complete 24-mer shell remains elusive (Sato et al., 2016). The dissociation of dimers is partially reversible and spontaneously occurs at highly acidic or basic pH levels, as described above.

1.5.1 H-ferritin as a smart nanovector

Among many nanovectors currently under investigation for biomedical purposes, ferritin H-chain homopolymer is one of the most versatile. Biological-derived nanoparticles are used in biomedicine due to their low toxicity and capacity to avoid the immune system. Indeed, HFt is a physiological, non-toxic protein already present in the human organism. Nanoparticles should have a diameter of 10-100 nm, as they have been shown to circulate in the blood for longer periods. Nanoparticles should not be too small (<5 nm) or too large (>150 nm) to prevent them from being filtered by the kidneys in the former case (Hoffman et al., 2014) or being entrapped in the liver/spleen in the latter. Ferritin has an outer diameter of 12 nm and its purification protocols result in high homogeneity and monodispersity levels (Z. Wang et al., 2017), key factors that increase the efficiency of a nanovector. Particles should maintain stability while in circulation to arrive in good condition at the intended disease site. The intersubunit interactions between the 24 monomers of HFt confer exceptional stability to the entire protein. As previously described, the cage is resistant to both denaturants and high temperatures (Z. Wang et al., 2017). One of the major features of the new drug delivery systems is to release the active molecule in the right organ, the unspecific uptake by healthy cells leads to serious cytotoxic side effects and low therapeutic levels at disease sites (De Jong & Borm, 2008; Ferrari, 2005). Nanoparticle-associated molecule delivery mechanisms have superior efficacy compared to conventional free drug formulations, which have a propensity to distribute indiscriminately throughout the body (Blanco et al., 2015; De Jong & Borm, 2008; Ferrari, 2005; Marcazzan et al., 2018). Therefore, nanoparticles need to be selective for specific tumor environments or possibly tumor cell types: in the case of HFt, it binds hTfR1 with nanomolar affinity (Fracasso et al.,

2016; L. Li et al., 2010). This receptor is highly overexpressed in iron-avid cancer cells and represents the ideal target for nanoparticle binding. Upon arrival at the site of disease, the nanoparticles should be internalized into cells to release the cargo (Blanco et al., 2015). In the case of HFt, the hTfR1-mediated endocytosis ensures its entry into cells (Tortorella & Karagiannis, 2014). The internal and external surfaces can be genetically and chemically modified. This allows for a wide range of molecules to be attached to the external surface or enclosed within the internal cavity, such as metals (Zhen et al., 2013), drugs (Lei et al., 2016), antibodies (Falvo et al., 2013), fluorescent molecules (C. Sun et al., 2011) and contrast agents (Lin et al., 2011). Commonly used methods for encapsulating cargo include disassembling the quaternary structure of HFt at drastic pH values and then reassembling it at a neutral pH (M. Kim et al., 2011). The limitations of this rough procedure include the possibility of a partial and incomplete reassembly of the cage and damage to the loaded compound (De Turris et al., 2017). Hence, HFts have been investigated in nanotechnology as biological nanocages for applications in targeted drug delivery (Falvo et al., 2016; Fracasso et al., 2016; X. Huang et al., 2017; Lei et al., 2016), bioimaging (Zhen et al., 2013), nanoelectronic devices (Kostiainen et al., 2013), vaccine development (Kanekiyo et al., 2013) and cancer theranostics (Cao et al., 2014; K. Fan et al., 2012; C. Sun et al., 2011), in this case, the interaction between HFt and CD71 is particularly exploited. Recent studies, carried out in vivo using paramagnetic ferritins within the context of MRI investigations in tumor models, demonstrated that HFt nanoparticles can distinguish cancerous cells from normal cells with a sensitivity of 98% and a specificity of 95% (K. Fan et al., 2012).

1.5.2 Lanthanide binding ferritin (HFt-LBT)

Besides their physiological function, the nanocage properties of ferritins have been investigated in several different biotechnological applications, such as tools for bioimaging (Kanekiyo et al., 2013; Z. Wang et al., 2017). Many studies have been carried out on quantum dots, gold nanoparticles and luminescent metal chelators (Bain & Staniland, 2015; Maity et al., 2017), whereas only a few studies have been done on ferritin-based constructs to use as smart luminescent probes. However, advanced optical imaging techniques need an expanded color palette of bright luminescent probes for biological visualization in order to enable real-time cellular imaging with high spatial resolution for close-up view into subcellular compartments, while providing consistent reduction of autofluorescence from biological specimen. In this framework, time delayed luminescence imaging techniques represent the

key tool in order to achieve high resolution and low background intensity (Bao, 2020; J. C. G. Bünzli, 2006; Handl & Gillies, 2005; Hemmilä & Laitala, 2005; Richardson, 1982). An engineered H-ferritin nanoparticle carrying a lanthanide binding tag (LBT) at the C-terminal end of each subunit was designed and synthesized (HFt-LBT). The LBT is a stretch of 17 aminoacids (YIDTNNDGWIEGDELLA) endowed with strong luminescence resonance energy transfer (LRET) sensitization properties since it has a tryptophan (Trp) residue that can act as an antenna transferring the absorbed energy to the lanthanide ion. Furthermore, the LBT shows low nanomolar affinities for the target ions and selectively binds to lanthanides as compared to over other common metal ions (Martin et al., 2007). LBT is the most convenient option for lanthanide protein labelling in that it can be directly encoded within a recombinant protein expression construct. The tag has been designed to be located inside the inner cavity, so the lanthanide ions diffusing through the surface pores could bind to the LBT sequence. LBT sequence was conceived according to the findings of Martin et al. (Martin et al., 2007), who demonstrated efficient lanthanide chelating properties of a peptide sequence derived from Ca^{2+} binding sites from Troponin C EF hand motif. Among lanthanides, I chose to use Eu^{3+} because it is particularly suitable for bioimaging thanks to its red emission that allows to reduce overlap with tissue autofluorescence and to match the biological transparency window. Europium ions (Eu^{3+}) are of strong interest in many photonic applications (J.-C. G. Bünzli & Eliseeva, 2010; Kido & Okamoto, 2002), in particular in organic light emitting diodes (OLEDs), lasers, optical communications, chemical sensor (Aulsebrook et al., 2018). Besides, the fine structure and the relative intensities of Eu^{3+} optical transitions depend on the local environmental conditions, so that they can be used for nanosensing applications.

1.5.3 *Archaeglobus fulgidus* ferritin (AfFt)

Crystal structures of ferritins from several aerobic bacteria and eukarya have been solved (Hempstead et al., 1997; Stillman et al., 2001; Takagi et al., 1998). Excluding the smaller Dps proteins that are comprised of 12 subunits, the quaternary architecture of all known ferritins is tetraeicosameric; 24 identical or similar polypeptides, each folded largely into a four-helix bundle, are arranged with octahedral (4-3-2) symmetry forming a hollow protein shell with inner and outer diameters of approximately 80 Å and 120 Å, respectively. *Archaeoglobus fulgidus* is a strictly anaerobic, hyperthermophilic, sulfate-reducing, marine

archaeon. The organism thrives in an extreme and dynamic environment located at the interface between superheated anaerobic vent fluids and frigid aerobic seawater. In contrast to most aqueous environments, vent fluids contain high concentrations of free ferrous iron ranging from micromolar to millimolar levels (Holden & Adams, 2003). However, brief exposure to oxygen or other iron-reactive compounds, such as H_2S present in the vent fluids, could be fatal to the cell or result in iron deficiency. The secondary and tertiary structures of AfFt and human HFt closely resemble, even in the metal ion binding mode, despite their low sequence similarity. Nevertheless, they deeply differ in the quaternary structure: AfFt has tetrahedral (2-3) symmetry, while HFt displays the canonical octahedral (4-3-2); instead of HFt 4-fold symmetry channels, four large (45 Å) pores open in the shell of AfFt as a result of the packing between two hexamers (Holden & Adams, 2003; E. Johnson et al., 2005) (Figure 1.10). Its oligomerization mechanism is easily controlled just by altering cations concentration in the buffer, it self-assembles from dimers to a complete 24-mer structure only at high salt concentrations (>0.3 M NaCl) (Swift et al., 2009) and does not require the harsh conditions of a pH jump needed for mammalian Fts. Nevertheless, the low (31%) sequence similarity of AfFt with mammalian Fts runs against the possibility of targeting AfFt onto hTfR1. The structural alignment of human HFt and AfFt reveals a shorter N-terminus and shorter BC loops between three of the four helices; those loops of adjacent subunits display the same geometry in both HFt and AfFt, though each couple adopts a different symmetry along the spherical surface of the protein cage, given the different dimer-dimer positioning within each complete 24-mer structure (E. Johnson et al., 2005).

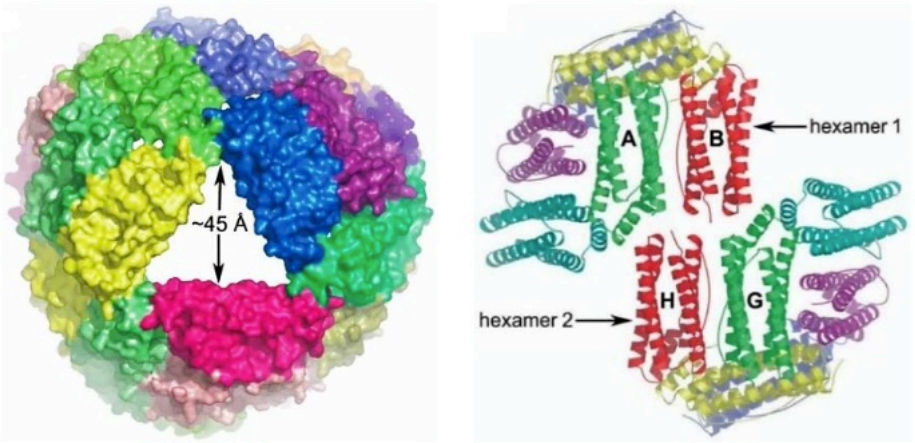

Figure 1.10 Left: Surface representation of AfFt tetraeicosameric assembly. The molecule is viewed from one of 4 large pores at a 3-fold symmetry axis. Right: ribbon model of the AfFtn asymmetric unit viewed, showing the novel 12mer interface (adapted from (E. Johnson et al., 2005)).

1.5.4 Humanized *Archaeoglobus fulgidus* ferritin (HumAfFt)

Ferritins are commonly used as nanovectors for drug delivery thanks to hTfR1 overexpression in cancer cells. The compound can be encapsulated inside the cavity through a pH jump: at extremely acidic or basic pH values, HFt disassembles into monomers, allowing the payload compound to bind to the internal cavity; then, the pH returned to neutrality, and the tetraicosameric structure is spontaneously reassembled (Crichton & Bryce, 1973). The most significant constraint in this procedure is the requirement for coarse conditions during cargo assembly. These conditions may compromise drug stability and result in an incomplete reassembly of the cage. The inevitable suboptimal load of cargo material, whose chemical structure is required to be pH resistant, often results in poor payload incorporation yields (M. Kim et al., 2011). Consequently, research efforts are focused on modifying the assembly properties of Ft nanocages either by inter-subunit interface mutagenesis or by genetic engineering of N- or C-terminal regions (S. Kim et al., 2016). Recently, ferritins from lower organisms such as bacteria and archaea endowed with different polymer association-dissociation thermodynamic and kinetic features, have emerged as possible alternatives to human HFts for applications requiring cargo material encapsulation (Sana et al., 2013). In particular, as already mentioned in paragraph 1.5.3, the ferritin from *Archaeoglobus fulgidus* (AfFt) exhibits distinctive self-assembly properties: in neutral buffers, it is present as a dimer, while in the presence of metal cations, it assembles into a non-canonical 24-mer cage with a peculiar tetrahedral geometry, having four 45 Å triangular pores on the protein shell (E. Johnson et al., 2005; Swift et al., 2009). Prof. Boffi's group of the Sapienza University in Rome, with whom I collaborated during this project, have worked to genetically modify the AfFt structure in order to have a chimeric nanoparticle characterized both by AfFt peculiar assembly/disassembly, that could lead to a completely reversible loading of a cargo, and by the recognition with hTfR1 typical of human HFt, that would allow mammalian cells internalization (De Turris et al., 2017). This objective could be achieved by inserting the HFt recognition epitopes for hTfR1 on AfFt sequence. At the time of this investigation, the binding region between CD71 and HFt was not solved yet. Therefore, they had to guess such HFt epitopes just from structural evidence. From the analysis of HFt and CD71 crystallographic structures, it was clear that the external loops of HFt are the most significant accessible area to CD71. Studies have shown that N or C-terminal deleted HFts are efficiently internalized by target cells, suggesting that these regions are not relevant for receptor recognition or uptake (Levi et al., 1988, 1989). As a consequence, the BC loop is considered the most likely candidate for hTfR1 recognition, in

addition to its known structural role in stabilizing the interdimer interface (Honarmand Ebrahimi et al., 2012, 2015). They decided to exploit this loop by mutating 9 AfFt aminoacids VKLYAVEEP (from residue 70 to 79 in AfFt numbering) into the corresponding HFt residues IFLQDIKKP: these residues are located at the center of the 12 residues long BC loop (Figure 1.11). In addition, a cysteine residue in position 54 (AfFt numbering) has been introduced by point mutation to provide a conjugation site of potential thiol reactive derivatives into the Ft cavity.

The resulting chimera was called "HumanizedAfFt" (HumAfFt) (Figure 1.12). As shown below, HumAfFt nanocarrier displays both the unique assembly/disassembly properties of the archaeal ferritin and is actively internalized by cancer cells.

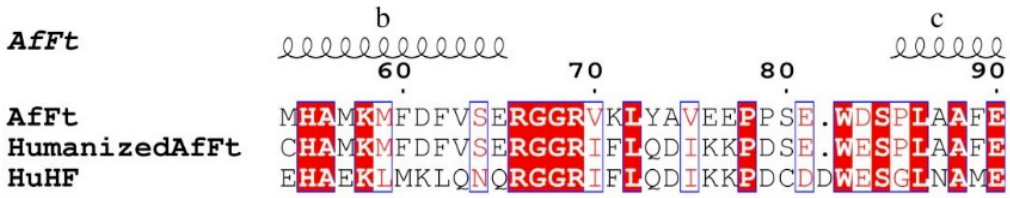

Figure 1.11 Structure-based sequence alignment of AfFt, HumAfFt, and HFt. Elements of secondary structure for the AfFt are shown on the top. White characters in a red background indicate strict conservation, residues with poor conservation are in black on a white background (adapted from (De Turris et al., 2017)).

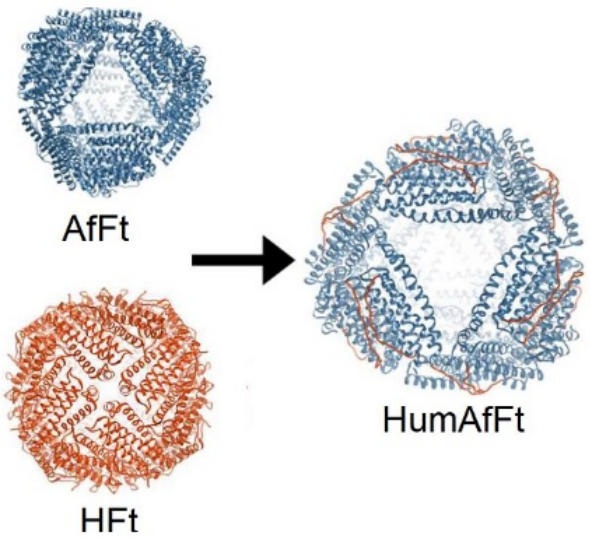

Figure 1.12 Schematic picture of the different parts constituting HumAfFt.

1.6 Lanthanides

Fluorescent probes using trivalent lanthanide ions are widely used in bioimaging thanks to their unique photophysical properties related to the *4f* orbitals (Werts, 2005): indeed, their spectra exhibit sharp peaks, their high quantum yields efficiently radiate most of the absorbed energy and their microsecond fluorescence provides the high spatiotemporal resolution required for real-time cellular imaging (Handl & Gillies, 2005). However, their small absorption cross sections pose several limits to their use in advanced optical imaging techniques, that require a bright fluorescent signal for proper biological visualization. To overcome this limitation, lanthanides are currently used in complex with small organic fluorophores which absorb a photon in the UV region and transfer it to the lanthanide, populating its excited state and allowing its emission (Moore et al., 2009). Such a luminescence resonance energy transfer (LRET) strongly depends on the proximity between the two fluorophores and can also be used as a probe of the local geometry around the lanthanide site. The lanthanides europium (Eu^{3+}) and terbium (Tb^{3+}) are unique fluorescent probes. In contrast to all fluorophores, these lanthanides display line spectra from the individual atoms (Lakowicz, 2006). The inner shell *f* orbital electrons are shielded from the environment, so that lanthanides do not display polarity-dependent spectral shifts and are not quenched by oxygen. Because of their low extinction coefficients, the lanthanides are not usually excited directly. The ions are at first bound to chelators that contain a fluorophore. The energy from the fluorophore can be efficiently transferred to the lanthanide. The energy of the excited fluorophore must be adequate to excite the lanthanide. Lanthanide-fluorophores complexes, thus, acquire peculiar photophysical properties that confer to the whole compound an improved luminescent signal. In particular, the efficiency of energy transfer between the fluorophore and the lanthanide is highly dependent on their distance (Moore et al., 2009): if they are within 5-6 Å, the low extinction coefficient of the ion can be overcome by Förster resonance energy transfer (FRET), a phenomenon referred to as "antenna effect", that allows for bright and photobleaching-less fluorescence signals (Dickson et al., 1995). Among lanthanides, Tb^{3+} and Eu^{3+} are the most used in biotechnology due to their more intense μs fluorescence in the visible region (Selvin, 2002). Lanthanide ions can also be incorporated into biomolecules for in vivo imaging applications of smart fluorescent probes internalized by cells or animals. To achieve this, a lanthanide binding sequence can be encoded within a recombinant protein expression construct using molecular biology strategies. Short polypeptides comprising 20 or fewer encoded amino acids, known as lanthanide-binding tags, have been developed (Sculimbrene & Imperiali, 2006). These

peptide sequences exhibit low-nanomolar affinities for the target ions, are selective for lanthanides over other common metal ions (Nitz et al., 2004) and can be inserted in the protein construct at the N or C-terminal domain or even at specific loops (Barb et al., 2012). The probe nature of these protein tags has been demonstrated by their use in various biotechnological applications (Goda et al., 2007). Apoferritins naturally bind more than one lanthanide ion in the ferroxidase site (Honarmand Ebrahimi et al., 2012; Stefanini et al., 1983), threefold channel and nucleation center, with considerably variable affinities (Treffry & Harrison, 1984). Lanthanides can be directly incorporated in Ferritin cavity after its pH-induced structure dissociation (Tian et al., 2015), but this method may lead to a random and inhomogeneous distribution within the inner hollow, resulting in possible aggregation-induced quenching effects and/or leakage to the outside through the iron channels. For instance, upon excitation between 280-295 nm, Tb^{3+}-ferritin complex show characteristic emission bands at 490 nm ($^5D_4$-$^7F_6$ Tb electronic transition) and at 544 nm ($^5D_4$-$^7F_5$ Tb electronic transition) due to a FRET sensitization effect provided by aromatic aminoacids (Bou-Abdallah et al., 2003). However, the distance between Terbium ions and aromatic moieties in native Fts make FRET efficiency very poor and suboptimal for any type of fluorescence/luminescence based measurement (Goda et al., 2007). To overcome the FRET inefficacy and to achieve an effective Tb^{3+} internalization in Ft, Prof. Boffi's group produced an engineered mouse HFt construct bearing a 17 aminoacids long lanthanide binding tag (LBT), genetically fused at the C-terminal end of each subunit (Calisti et al., 2018). Mouse HFt was used because its sequence is identical to the human one within the CD71 binding region and in view of more favorable immunogenic profile for forthcoming in vivo study in mice. The polypeptide has been designed to be located inside the inner cavity as a prolongation of the Ferritin E helix, in order to trap the lanthanide ions diffusing from the outside through the surface pores. They proved that this biomolecular nanosystem has high affinity for Tb^{3+} and is endowed both strong FRET sensitization and CD71 receptor binding properties (Calisti et al., 2018).

2. Aim of the thesis

Considering the importance of nanostructured supports as nanocarriers, the aim of this research project is the development of new ferritin-based nanovectors applicable in the field of theranostics. HFt nanoparticles represent one of the most suitable vectors for delivering molecules to cells due to their internalization by CD71 (L. Li et al., 2010), a transmembrane receptor that is overexpressed in most types of cancer cells (Daniels, Delgado, Helguera, et al., 2006; Daniels, Delgado, Rodriguez, et al., 2006; Daniels et al., 2012; Daniels-Wells & Penichet, 2016; Hopkins & Trowbridge, 1983). In this thesis, two ferritin-based nanovectors are studied and characterized with different approaches to pave the way for their use in biomedical fields.

The first nanocarrier is the Lanthanide binding Ferritin (HFt-LBT), in which a high Lanthanide affinity sequence has been genetically fused to the mouse H-chain Ferritin structure to provide a construct acting both as carrier targeted to CD71 and as a FRET sensitizer by an appropriate antenna effect. I studied the interaction between the Eu^{3+} ions and the HFt-LBT by means of spectroscopic techniques, in order to investigate the interaction between the protein and the lanthanide ions and to the future use of HFt-LBT Eu^{3+} complex in diagnostics. Throughout the chapter 3, steady state emission measurements clearly show the interaction between them by the huge increase of Eu^{3+} emission due to an energy transfer from the donor to the ions. Time-resolved emission spectroscopy has been employed to deeply investigate this energy transfer and allows us to discriminate the presence of two Eu^{3+}species: one bonded on the LBT and one located in the other sites of the HFt-LBT.

The second nanocarrier is the Humanized *Archaeoglobus fulgidus* Ferritin (HumAfFt), engineered to retain both the reversible, cations-induced association of the archaea ferritin and the internalization in human cells typical of HFt through CD71 recognition. I used the HumAfFt as a coating material for 10 nm SPIONs, in order to create a new magnetic nanocarrier able to discriminate cancer cells from normal cells and to be influenced by a magnetic field as well. The obtained complex (HumAfFt-SPIONs) was characterized in terms of HumAfFt and SPIONs content, morphology, size, and stability (chapter 4). Moreover, the preferential target of the HumAfFt-SPIONs towards cancer cells was demonstrated in vitro by biological assays. The biocompatible coating of SPIONs is essential for most biomedical applications since this increases the stability of the iron oxide core,

preventing aggregates formation and allowing functionalization of the surface of the nanoparticles with targeting ligand. Biological studies on normal and cancer cells have shown that HumAfFt-SPIONs do not induce toxicity in cells even at high concentrations. Furthermore, magnetization analyzes have proved that the magnetic properties of the SPIONs remain unchanged upon encapsulation in HumAfFt, this means that the HumAfFt-SPIONs can be used in the therapeutic field of hyperthermia. I also started to evaluate the ability of HumAfFt-SPIONs to act as contrast for magnetic resonance imaging (MRI). Preliminary results, as shown in chapter 5, have demonstrated that the new HumAfFt-SPIONs improve resolution in T_2-weighted images of MRI.

The conducted studies are very promising in view of the use of these new highly stable and biocompatible nanocomplexes, especially in prospective theranostic applications.

3. Engineered Ferritin with Eu^{3+} as a Bright Nanovector: A Photoluminescence Study

This chapter is adapted from the article *"Engineered Ferritin with Eu^{3+} as a Bright Nanovector: A Photoluminescence Study",* (Affatigato, Sciortino, et al., 2023).

3.1 Introduction

In collaboration with Prof. Boffi's group of the Sapienza University in Rome, I have synthesized and purified the HFt-LBT, a new engineered ferritin nanoparticle, made of the H chain mouse ferritin (HFt) fused with a specific lanthanide binding tag (LBT). The HFt-LBT has one high affinity lanthanide binding site per each of the 24 subunits and a tryptophane residue within the tag that acts as an antenna able to transfer the energy to the lanthanide ions via a LRET process. It has been characterized for its interaction with europium ions (Eu^{3+}) in view of potential applications in bioimaging. In particular, among lanthanides, I selected europium for its red emission that allows to reduce overlap with tissue autofluorescence. Steady state emission measurements and time-resolved emission spectroscopy have been employed to investigate the interaction between the HFt-LBT and the Eu^{3+} ions.

Luminescent probes based on trivalent lanthanide ions are becoming widespread due to their advantageous photophysical properties (Bao, 2020; Handl & Gillies, 2005): narrow band emission spectra, large Stokes shift (150–300 nm), and long luminescence lifetimes from micro to milliseconds (J. C. G. Bünzli, 2006; Hemmilä & Laitala, 2005). Lanthanide f-electrons can radiate most of the absorbed energy, but their small absorption cross sections hamper their practical use (Richardson, 1982). Lanthanides are usually not excited by direct light irradiation within their absorption peak, but rather excited through small organic fluorophores, that absorb in the UV region with an adequate absorption cross section and transfer the absorbed energy to the lanthanide atom (Silly et al., 2013; Yang et al., 2004). Such a luminescence resonance energy transfer (LRET) strongly depends on the proximity between the two fluorophores (Y. J. Huang et al., 2019; Sculimbrene & Imperiali, 2006) and can also be used as a probe of the local geometry around the lanthanide site.

Among lanthanides, Eu^{3+} ions are of strong interest in many photonic applications (J.-C. G. Bünzli & Eliseeva, 2010; Kido & Okamoto, 2002), in particular in organic light emitting

diodes, lasers, optical communications, chemical sensor (Aulsebrook et al., 2018). Eu^{3+} is particularly suitable for bioimaging because its red emission allows to reduce overlap with tissue autofluorescence and to match the biological transparency window. Besides, the fine structure and the relative intensities of Eu^{3+} optical transitions depend on the local environmental conditions, so that they can be used for nanosensing applications.

For the purposes of this work, I have used the H chain mouse ferritin fused with a lanthanide binding tag (LBT) on its C-terminal end to facilitate the incorporation of Eu^{3+} ions into the ferritin nanoparticle. The LBT is a stretch of 17 aminoacids (YIDTNNDGWIEGDELLA) endowed with strong LRET sensitization properties since it has a tryptophan (Trp) residue that can act as an antenna transferring the absorbed energy to the lanthanide ion. Furthermore, the LBT shows low nanomolar affinities for the target ions and selectively binds to lanthanides as compared to over other common metal ions (Martin et al., 2007). LBT is the most convenient option for lanthanide protein labelling in that it can be directly encoded within a recombinant protein expression construct. The tag has been designed to be located inside the inner cavity, so the lanthanide ions diffusing through the surface pores could bind to the LBT sequence (Figure 3.1).

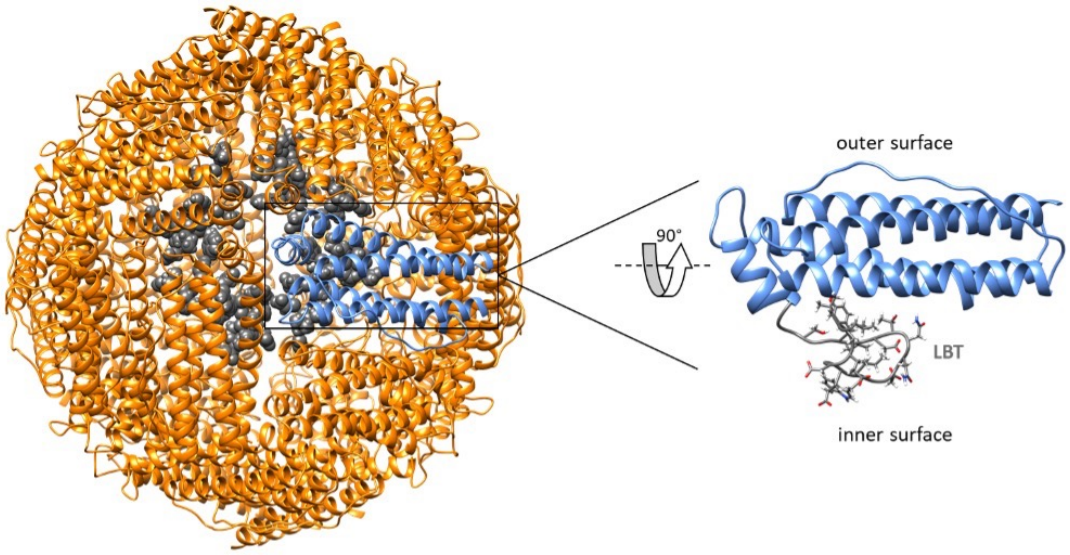

Figure 3.1. Structural model of HFt-LBT. On the left, the structure of the protein cage in which the LBT, pointing inside the cavity, is highlighted in gray and represented as spheres. On the right, detail of the monomer.

The construct would thus act both as carrier targeted to CD71 receptors and as a LRET sensitizer. Mouse ferritin was used in view of the identical sequence within the CD71 binding

region as the human ferritin sequence and because of obviously more favorable immunogenic profile for forthcoming *in vivo* study in mouse.

I studied the interaction between the Eu^{3+} ions and the HFt-LBT with spectroscopic techniques, in order to investigate the interaction between the protein and the lanthanide ions and to pave the way to the future use of HFt-LBT Eu^{3+} complex in theranostics. Steady state emission measurements clearly show the interaction between them by the huge increase of Eu^{3+} emission due to an energy transfer from the Trp to the ions. Time-resolved emission spectroscopy has been employed to deeply investigate this energy transfer and allows us to discriminate the presence of two Eu^{3+} species: one bonded on the LBT and one located in the other sites of the HFt-LBT. Moreover, I have been able to identify the Eu^{3+} energy states involved in the process, which provides evidence to attribute the LRET process to a multipolar energy transfer which prevails on FRET or Dexter-type processes.

3.2 Material and methods

Protein expression and purification

Mouse H ferritin fused with a lanthanide binding tag (HFt-LBT) was expressed in *Escherichia coli* BL21 upon induction with 1 mM IPTG (Isopropyl-β-D-1-thiogalactopyranoside) at OD_{600} = 0.6 for 16 hours. Bacterial paste from 2 L culture was resuspended and sonicated in 100 mL of 20 mM HEPES buffer, pH 7.5, containing 200 mM NaCl, 1 mM TCEP (tris(2-carboxiethyl)phosphine), and protease inhibitors. The supernatant was heated at 78 °C for 10 minutes and the denatured proteins were removed by centrifugation. The soluble fraction was treated with 50% and 70% $(NH_4)_2SO_4$ and both the pellets were resuspended in 20 mM sodium phosphate buffer pH 7.2 containing 20 mM $MgCl_2$, extensively dialyzed versus the same buffer, and then digested with 5 mg of deoxyribonuclease I for 1h at 37°C. After digestion, the protein sample was dialyzed versus 20 mM HEPES buffer pH 7.4 containing 150 mM NaCl and loaded onto a HiLoad 26/600 Superdex 200 pg column previously equilibrated in the same buffer, using an ÄKTA-Pure apparatus (Cytiva). The eluted ferritin was concentrated using Amicon Ultra-15 centrifugal filter devices (100 kDa cut-off), sterile filtered, and stored at 4 °C. Protein concentration was calculated by measuring the UV spectrum using an extinction coefficient of 32400 $M^{-1}cm^{-1}$ and protein purity was checked by SDS-PAGE. Protein yield was about 50 mg per 1 L culture.

Photoluminescence of HFt-LBT Eu^{3+}

Intrinsic luminescence emission spectra were detected using a Jasco FP-6500 equipped with a Jasco peltier thermostat; samples were positioned in a quartz cuvette of 1 cm and all emission spectra were recorded at 0.5 nm wavelength intervals with excitation and emission bandwidth of 10 nm, scan speed of 100 nm/min and integration time of 1 s upon excitation at 280 nm at 25°C. Luminescence static spectra were performed using 10 μM HFt-LBT in 3 mL HEPES 20 mM and NaCl 150 mM buffer solution pH 6.4. Luminescence spectra of the protein Eu^{3+} complexes were recorded after 30 min incubation and after addition of incremental amount of $EuCl_3$ in buffer solution in order to saturate all possible Eu^{3+} binding sites in HFt-LBT. Before recording spectra, protein solutions were exchanged with buffer (europium free) by doing dialysis using a molecular porous membrane tubing MWCO: 3.5 kD (Spectral/Por Dialysis Membrane Standard RC Tubing) in order to remove unbound and weakly bound metal ions (4 exchanges steps). Protein concentration was measured again and adjusted to the final concentration with buffer. Luminescence titrations were carried out by adding in the sample incremental amount (5 μL or multiples) of a 3 mM europium stock solution under stirring. Emission spectra were recorded 30 minutes after addition of $EuCl_3$ solution aliquots. Luminescence intensity of Hft-LBT Eu^{3+} complex as a function of the Eu^{3+}/HFt-LBT ratio has been reported. Luminescence intensity was recorded at 615 nm and 329 nm corrected for the dilution factor.

Time-resolved photoluminescence of HFt-LBT Eu^{3+}

Time-resolved photoluminescence decays were recorded using 10 μM HFt-LBT in 3 mL HEPES 20 mM and NaCl 150 mM buffer solution pH 6.4 with different concentrations of Eu^{3+}. The emission spectra were recorded by exciting the samples by 5 ns laser pulses (IRF ~2 ns) of 0.1−0.2 mJ energy derived from a tunable laser (410-700 nm) consisting of an OPO (optical parametric oscillator) pumped by the third harmonic of a pulsed Q-switched Nd:YAG laser and finally duplicated by an UV-module in order to obtain 280 nm nanosecond beam. The spectra and the kinetics were detected by an intensified CCD camera which acquires the emission spectra within a specific time frame (the duration can be set by the operator), with controlled delays with respect to the laser pulse. The time frame is fixed at 20 ms with zero delay from the laser pulse in order to obtain an equivalent of a steady state measurement. In this way, the whole emission is collected. The appropriate time frame was

set on the basis of the expected lifetime of the sample we wanted to collect. Thus far, a temporal window of 0.5 ns was set to record short lifetimes such as the one of the Trp, and a time frame of 25 μs and 100 μs to record the europium longer lifetimes. The Eu^{3+} emission decay profiles were least-squares fitted to a biexponential fitting function $I(t) = A_1 \exp\left\{-\frac{t}{\tau_1}\right\} + A_2 \exp\left\{-\frac{t}{\tau_2}\right\}$.

3.3 Results and discussion

3.3.1 Photoluminescence of HFt-LBT Eu^{3+}

The emission properties of HFt-LBT Eu^{3+} in steady-state were investigated to detect any evidence of interaction between HFt-LBT and Eu^{3+} ions, by comparison with the optical properties of free Eu^{3+} in solution. We compared steady state Eu^{3+} emission spectra at different concentrations, by photoexciting a solution of the lanthanides dissolved in the same buffer solution at 280 nm (Figure 3.2A).

As expected, the emission efficiency collected from free lanthanide ions in solution was very low, as demonstrated by the signal-to-noise ratio in (Figure 3.2A).

Despite the low signal, it is possible to recognize several sharp spectral lines as the electronic transitions typical of europium ions. Under the same experimental conditions, the luminescence of HFt-LBT Eu^{3+} complexes, at the same lanthanides concentrations, has been recorded (Figure 3.2B). Before each measurement, the samples were dialyzed with buffer (europium free) to remove unbound and weakly bound metal ions. Eu^{3+} emission efficiency was observed to be at least two orders of magnitude more intense with respect to that observed with free Eu^{3+} ions. The emission enhancement is ascribed to HFt-LBT Eu^{3+}complex formation in which Eu^{3+} is excited via LRET. This result is confirmed by comparing the excitation spectra of the HFt-LBT, Eu^{3+} and HFt-LBT Eu Eu^{3+} at a fixed concentration of HFt-LBT (10 μM) and Eu^{3+} (24 μM) (Figure 3.3).

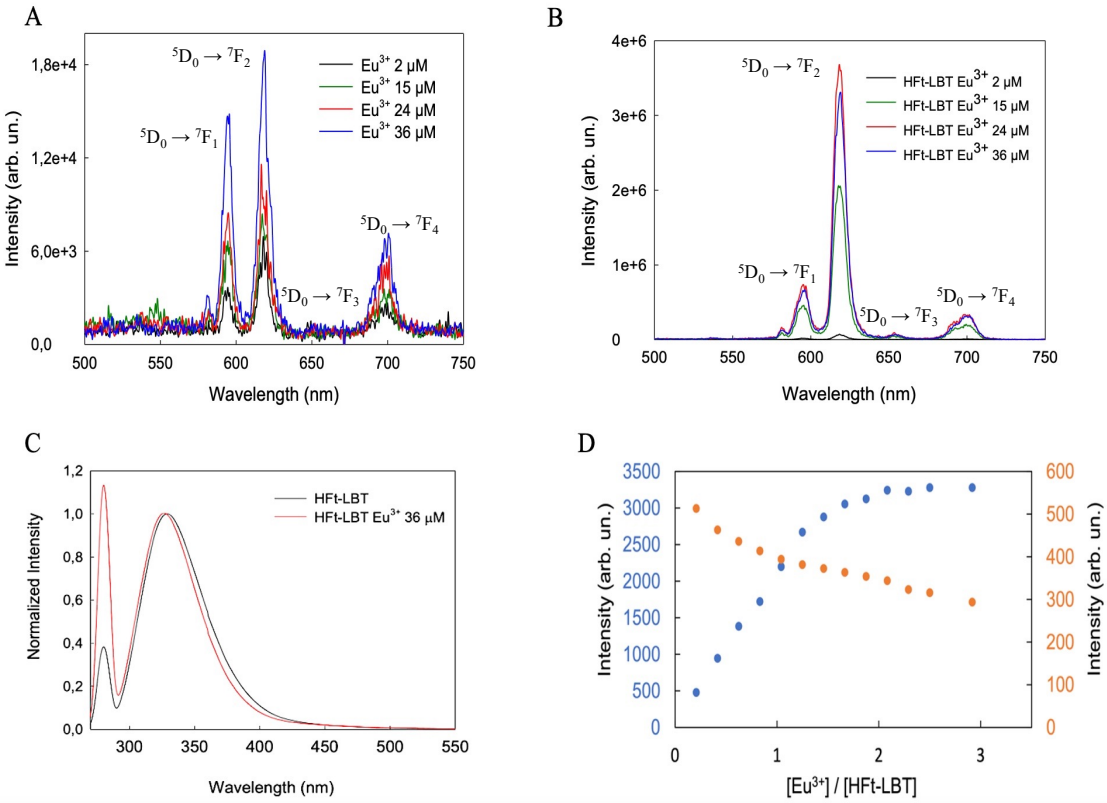

Figure 3.2 (A) Steady state emission spectra in the spectral range of europium emission, as excited at 280 nm of Eu^{3+} in buffer solution. (B) Steady state emission spectra in the spectral range of europium emission, as excited at 280 nm of the HFt-LBT Eu^{3+} complex, as obtained at four different concentrations of Eu^{3+}. (C) Normalized emission spectra in the near-UV of HFt-LBT and HFt−LBT Eu^{3+} complexes excited at 280 nm. (D) Luminescence intensity of HFt−LBT Eu^{3+} complex as a function of the Eu^{3+}/HFt-LBT ratio per subunit. Luminescence intensity shown in the graph was recorded at 615 nm (blue points) for the europium emission and at 329 nm (orange points) for protein emission.

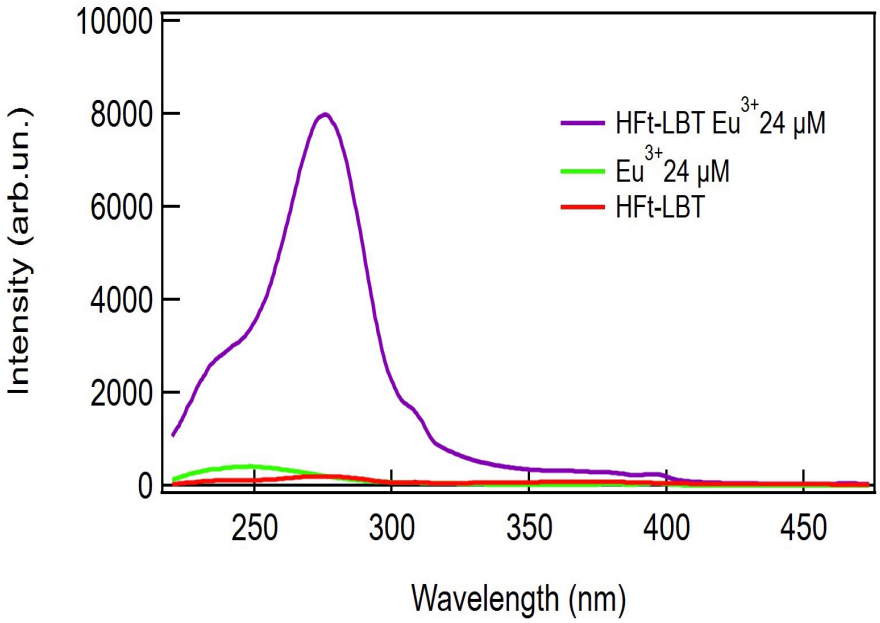

Figure 3.3 Excitation spectra of HFt-LBT, Eu^{3+} and HFt-LBT Eu^{3+}. The emission wavelength is 615 nm.

A second relevant modification is the variation of the ratio between the intensity of different electronic transitions. The $^5D_0 \rightarrow {}^7F_2$ emission line peaking at 615 nm is much more intense than the other transitions. The electric dipole (ED) $^5D_0 \rightarrow {}^7F_2$ transition is called "hypersensitive transition", which means that its intensity is more sensitive to the coordination environment around the Eu^{3+} ion, and to its geometry and symmetry, with respect to the other electronic transitions (Heffern et al., 2014). This transition is dominant in the emission spectrum of the HFt-LBT Eu^{3+} complex, and thus primarily responsible for its high emission efficiency due to the stable chemical environment around the Eu^{3+} ion (Binnemans, 2015). The intensity ratio between the peak at 615 nm ($^5D_0 \rightarrow {}^7F_2$) and the one at 580 nm ($^5D_0 \rightarrow {}^7F_1$) is found to be 1.2 in free europium and about 4 in the HFt-LBT Eu^{3+} complexes. This variation suggests a modification of the Eu^{3+} local environment, corresponding to the incorporation of the ion with a consequent perturbation of its electronic transitions.

The huge increase of Eu^{3+} emission suggests that, when the complexes are formed, the UV excitation is absorbed by the protein which acts as an antenna, and then releases the energy while exciting the europium ions. The Trp are the residues involved in the protein emission (as shown in Figure 3.2C), and, in particular after the photoexcitation, the Trp of the tag,

which is tightly bound to the lanthanide, is expected to transfer the energy to the europium, thus increasing its emission.

In order to better analyse the variations in the emission spectra of the Trp and the Eu^{3+}, and the interplay between the two, we carried out a titration by adding free Eu^{3+} ions to the HFt-LBT solution monitoring both the europium and Trp emission (Figure 3.2D). The results demonstrate a progressive increase of the intensity at 615 nm for europium and an anticorrelated quenching of the Trp luminescence at 329 nm, when the Eu^{3+}/HFt-LBT concentration ratio increases.

The titration endpoint, that is the Eu^{3+}/HFt-LBT ratio at which saturation is reached, was observed at 2 equivalent amounts of Eu^{3+} per subunit instead of the predicted 1 equivalent based on the presence of one LBT moiety per subunit. This suggests that the Trp residue of the LBT acts as an antenna not only for the very close Eu^{3+} ion, but also for a few extra Eu^{3+} atoms bound to the natural ferritin binding sites. As reported in a previous study on HFt-LBT with terbium (Calisti et al., 2018), the HFt-LBT construct is capable of: 1) high affinity binding of 24 Ln^{3+} atoms, one per each lanthanide binding tag; 2) intermediate affinity binding of 24 Ln^{3+} atoms at the ferroxidase binding site; and 3) lower affinity binding of 8 Ln^{3+} atoms at the entrance of the 3-fold channels. Hence the HFt-LBT is able to bind a total of 58 Ln^{3+} with different affinities, leading to an overall stoichiometry that approaches 2.3 Ln^{3+} atoms per subunit.

In addition to the protein emission quenching, comparison of the emission spectrum of the HFt−LBT Eu^{3+} with that of bare HFt-LBT (Figure 3.2C) shows a blue shift of the peak in the presence of ions due to the energy changes in the electronic transitions (Sindrewicz et al., 2019).

Moreover, in order to verify the predominant involvement of Trp of the LBT with respect to other possible aromatic aminoacids, I compared the steady state emission of Eu^{3+} in contact with HFt-LBT with the one of Eu^{3+} in contact with the wild-type protein (HFt) (Figure 3.4). From this comparison, it is evident that the other aromatic aminoacids which are contained in the protein do not have significant effects on the energy transfer process; in contrast, only the Trp within the tag is relevant for the observed enhancement.

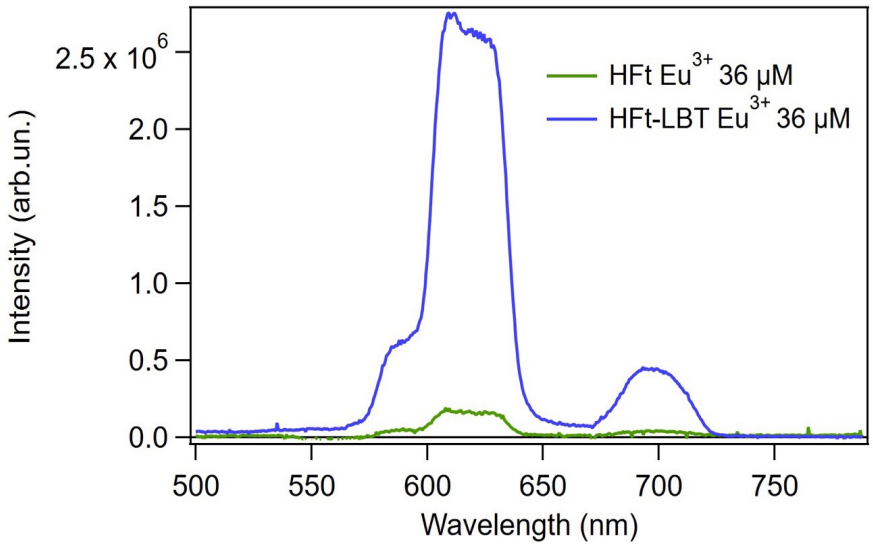

Figure 3.4 Steady state emission spectra in the spectral range of Europium emission, as excited at 280 nm of Eu^{3+} in complex with HFt and in complex with HFt-LBT.

3.3.2 Time-resolved photoluminescence of HFt-LBT Eu^{3+}

The dynamics of energy transfer in HFt-LBT Eu^{3+} were investigated by recording the emission band of both Eu^{3+} and Trp using time resolved measurements. The singlet-singlet Trp emission at 340 nm of the bare protein, excited at 280 nm, decays with a lifetime of $\tau_0 \sim$ 3.4 ns as obtained by a fitting procedure from the kinetics in Figure 3.5.

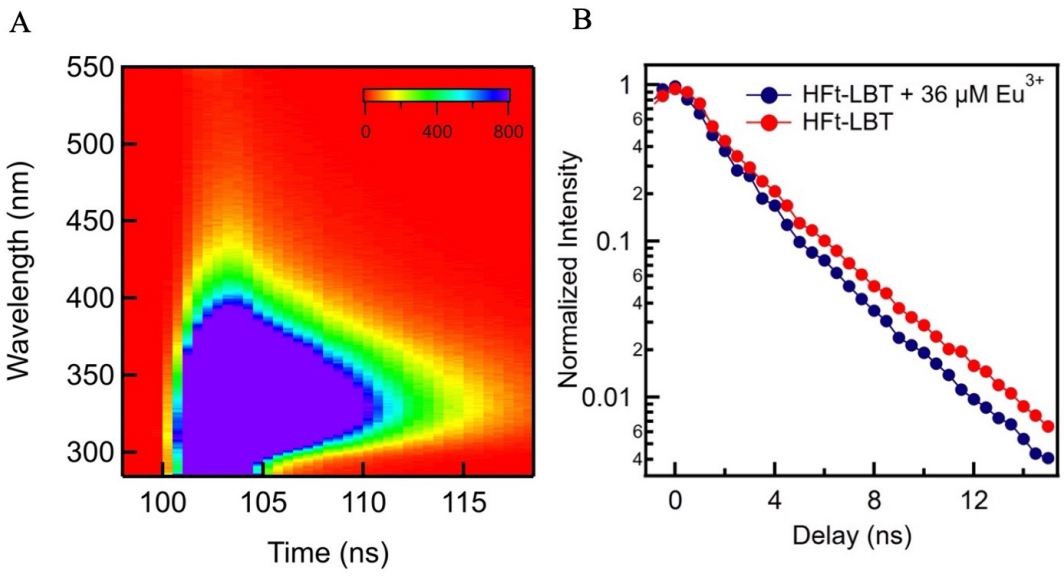

Figure 3.5 2D Fluorescence decay map of the HFt-LBT excited at 280 nm. (B) Kinetics decays at 340 nm of bare protein (red curve) and of HFt-LBT Eu^{3+} complex (blue curve) both excited at 280 nm.

This value was compared with the lifetime of the Trp in the HFt-LBT Eu^{3+}complex (Figure 3.5B). As shown in Figure 3.5B, the lifetime of the complex shortens reaching a value of τ_{Eu} ~ 3.0 ns indicating an interaction between europium ions and H-Ferritin which is consistent with an energy transfer from the S_1 state of the Trp to the electronic states of Eu^{3+} (Miyazaki et al., 2020). More precisely, from the variation of the lifetime induced by the presence of europium it is possible to directly estimate the energy transfer rate k as $\frac{1}{\tau_{Eu}} - \frac{1}{\tau_0} = 0{,}04\ ns^{-1}$.

I also analysed the luminescence decay kinetics of the bare Eu^{3+} ions (Figure 3.6) and of the ions forming complexes with the HFt-LBT protein (Figure 3.7).

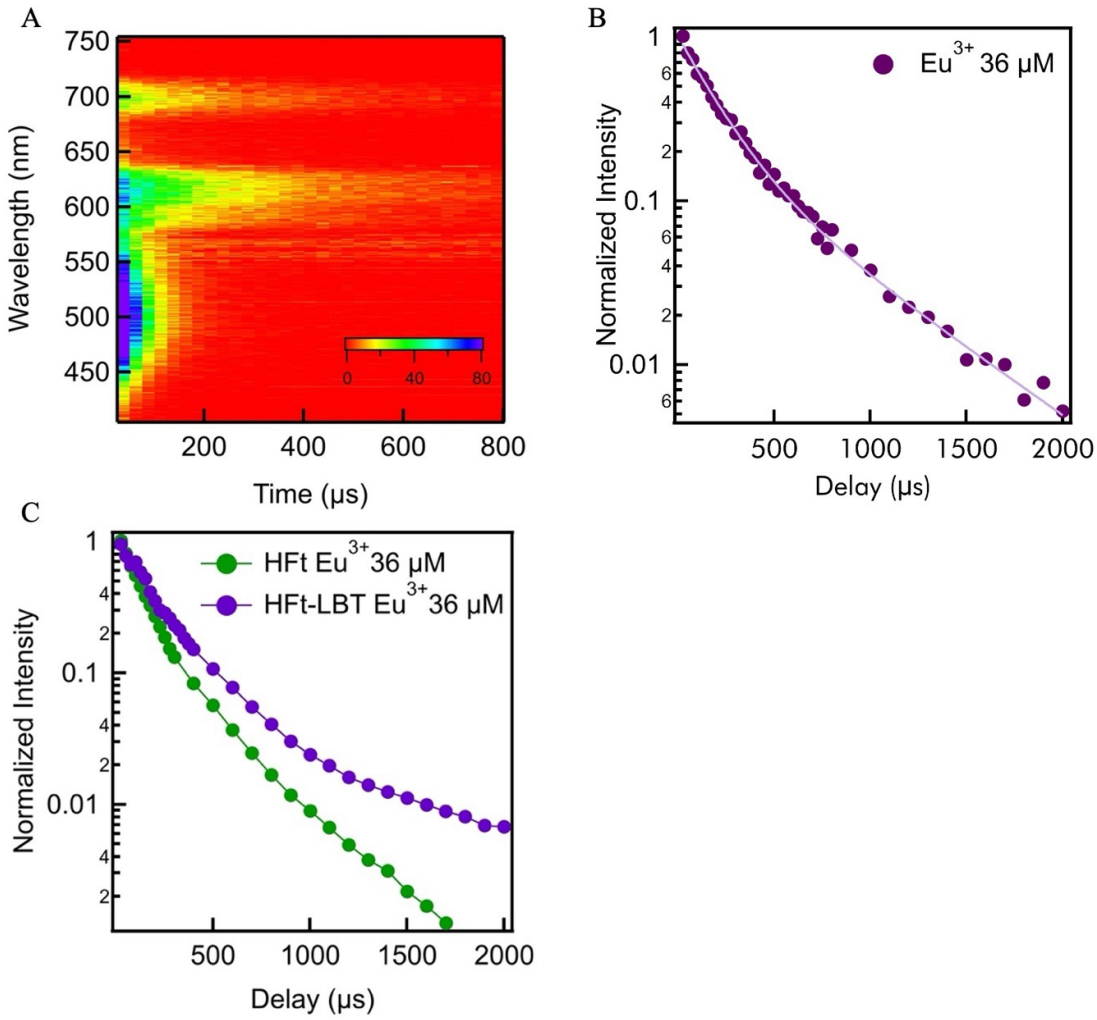

Figure 3.6 (A) 2D Fluorescence decay map of the Eu^{3+} excited at 280 nm. (B) Luminescence decay of Eu^{3+} in buffer solution. (C) Luminescence decay of Eu^{3+} in complex with HFt and with HFt-LBT.

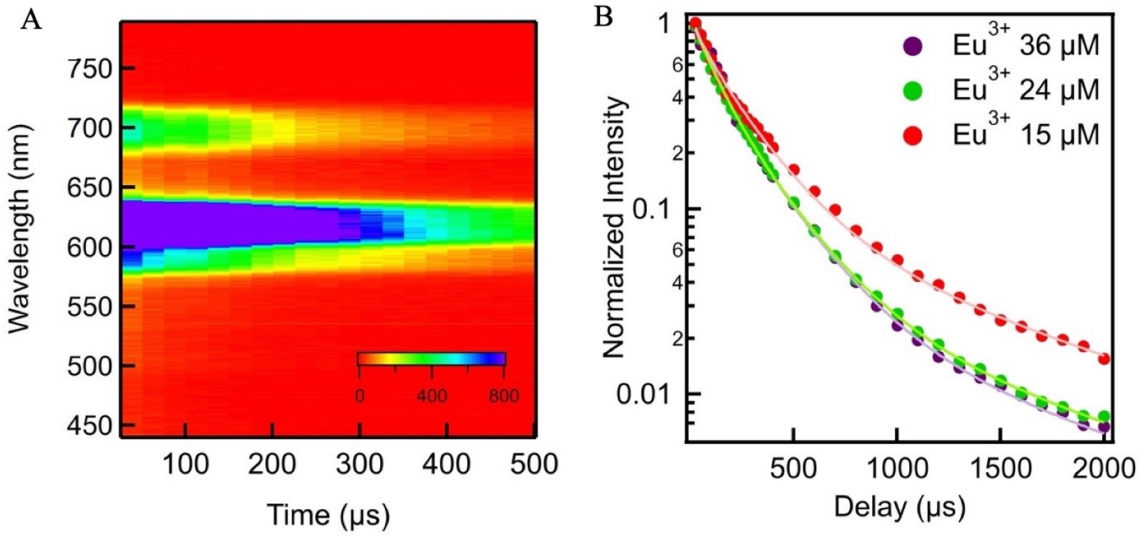

Figure 3.7 2D Fluorescence decay map of HFt-LBT Eu^{3+} excited at 280 nm and recorded in the visible range. (B) Decay kinetics at 615 nm of HFt-LBT Eu^{3+} complexes at three different Eu^{3+} concentrations.

The kinetics of the $^5D_0 \rightarrow {}^7F_2$ emission at 615 nm of bare Eu^{3+} can be described as a double exponential decay with two characteristic timescales: $\tau_1 = (175 \pm 10)$ µs and $\tau_2 = (530 \pm 20)$ µs. The presence of two timescales is related to different geometrical configurations around the solvated ions in the buffer solution (J. C. G. Bünzli et al., 2010).

When europium ions bind to HFt-LBT, the recorded kinetics change and, in addition, they depend on ions concentration (Figure 3.7B). The decay timescales of the 615 nm emission recorded after adding 15 µM of Eu^{3+} to the HFt-LBT solution were observed to be $\tau_1 = (100 \pm 10)$ µs and $\tau_2 = (250 \pm 20)$ µs, both values being very different from the ones observed for free Eu^{3+} in solution, thus demonstrating a binding interaction with HFt-LBT. Then, increasing the amount of europium from 15 µM to 24 µM, I observed that the kinetics change as shown in Figure 3.7B. A fitting procedure on these data indicates the presence of the same two timescales (100 µs and 250 µs) but with different weights (Table 3.1). Adding even more Eu^{3+} does not modify anymore the kinetics (Figure 3.7B). The results of the fitting procedures on the three decay curves are reported in Table 3.1.

Table 3.1 Decay times τ_1 and τ_2 (and their respective weights) of the Eu^{3+}, added at three different concentrations to a solution of HFt-LBT.

	HFt-LBT Eu 15 µM	HFt-LBT Eu 24 µM	HFt-LBT Eu 36 µM
$W\tau_1$	26%	44%	46%
τ_1	100 ± 10 µs	100 ± 10 µs	100 ± 10 µs
$W\tau_2$	66%	53%	52%
τ_2	250 ± 20 µs	250 ± 20 µs	250 ± 20 µs

I explained the observed changes of the kinetics with increasing europium concentration as follows. The double-exponential nature of these decay curves indicates the presence of two different protein environments corresponding to two distinct binding sites for Eu^{3+} ions. Interestingly, the amplitude of the slower kinetic component, τ_2= (250 ± 20) µs, is always higher than the first one, especially at the lowest concentration of added Eu^{3+}. Considering the high binding affinity between the ions and the LBT tag, it is thus reasonable to associate such a timescale to the electronic transition of europium ions which are coordinated to LBT. By contrast, the shorter phase, characterized by τ_1= (100 ± 10) µs, is possibly related to Eu^{3+} ions hosted within the 3-fold channels with lower binding affinity. As a control, I performed time resolved measurements on a HFt Eu^{3+} complex without the LBT. The recorded time courses are reported in C in comparison with the tagged protein. From C, it is evident that the kinetics are markedly different, indicating that the presence of the tag dramatically modifies the photon decay dynamics. The fitting procedure on HFt Eu^{3+} kinetics returns two rate constants τ_1= (110 ± 10) µs and τ_2= (330 ± 20) µs (Table 3.2).

Table 3.2 Luminescence decay times τ_1 and τ_2 of Eu^{3+} in buffer solution, in complex with HFt and in complex with HFt-LBT.

	Eu^{3+} 36 µM	HFt Eu^{3+} 36 µM	HFt-LBT Eu^{3+} 36 µM
τ_1	175 ± 10 µs	110 ± 10 µs	100 ± 10 µs
τ_2	530 ± 20 µs	330 ± 20 µs	250 ± 20 µs

The shorter time is compatible with the shorter time obtained in presence of tag. This indicates, again, that this timescale does not depend on the tag suggesting the binding of Eu^{3+} at a site of the 3-fold channel with lower binding affinity. The longer timescale, instead, is different from that one obtained in presence of the tag, thus indicating the direct involvement of the tag in the energy transfer transition.

I compare the absorption spectrum of the ion with the fluorescence spectrum of Trp in order to understand which europium transition is involved in the energy transfer (Figure 3.8).

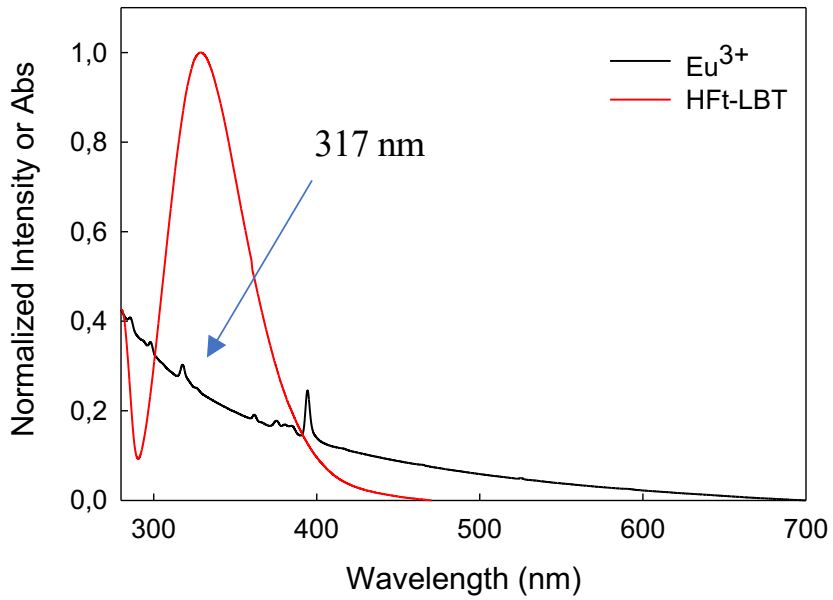

Figure 3.8 Overlapping of the emission spectrum of HFt-LBT (λ_{exc} = 280 nm) and the absorbance spectrum of Eu^{3+}.

The comparison shows that the $S_1 \rightarrow S_0$ transition of Trp spectrally overlaps with several europium electronic transitions especially with the $^7F_0 \rightarrow {}^5H_5$ which most likely plays the role of the acceptor transition.

However, a classical FRET mechanism can be ruled out as being the pathway of energy transfer. In fact, from the known rate of energy transfer of 0.04 ns^{-1} which was estimated from the changes of Trp lifetime (Figure 3.5), we tried to estimate the r_0 (Förster distance) (Lakowicz, 2006) through the known relation $k_T(r) = \frac{1}{\tau_D}\left(\frac{R_0}{r}\right)^6$. The obtained value of r = 0,13 Å, is so low that it rules out a classical FRET mechanism. Besides, FRET, which is an electric dipole driven transition, is also inconsistent with the selection rules with this donor

acceptor pair, because the acceptor transition ($^7F_0 \rightarrow {}^5H_5$) implies a change of angular momentum higher than 1 ($\Delta J>1$). Therefore, based on the literature, we propose that this energy transfer is a multipolar interaction between the Trp and the Eu^{3+} (Tanner et al., 2018). The energy transfer is followed by a fast internal conversion to $^5D_0$ energy state which decays to $^7F_2$ emitting photons in the microsecond range. A simple model of the interaction is shown in Figure 3.9.

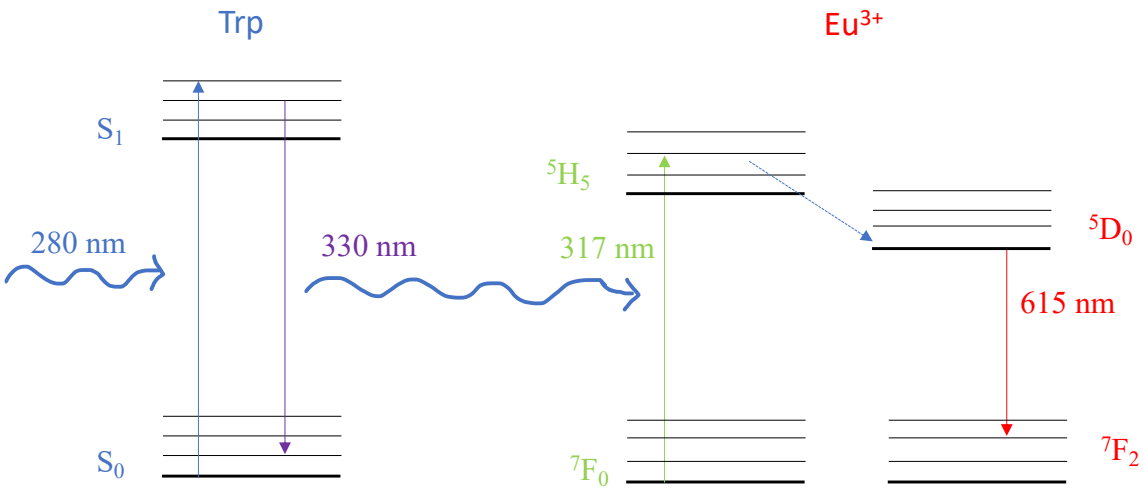

Figure 3.9 Schematic energy transfer process from the Trp residue of the tag to the Eu^{3+} ion in the complex HFt-LBT Eu^{3+}.

3.4 Conclusion

A ferritin nanocage has been designed in order to guide the allocation of metal sites inside the cavity and display the best geometry for an efficient energy transfer. Thereby, mouse ferritin endowed with a specific metal binding tag, able to act as an antenna system for europium has been obtained. Energy transfer dynamics in HFt-LBT Eu^{3+} complex after photoexcitation of the antenna moiety using photoluminescence has been observed for the first time, demonstrating the successful design of a complex capable of amplifying the emission intensity of Eu^{3+} through multipolar energy transfer from Trp to the $^7F_0 \rightarrow {}^5H_5$ accepting transition of the lanthanide ions. The detailed study of the luminescent properties

of the complex revealed two distinct lanthanide binding environments, one related to the specific coordination at the binding tag, and a secondary site with lower binding affinity associated to Eu^{3+} ions in the threefold channels on the protein surface. In this framework, the key physical properties of the tag are thus coupled to the CD71 receptor recognition properties of the ferritin in order to produce a unique luminescent nanovector capable of a strong emission at the typical Eu^{3+} peak at 615 nm upon Trp excitation at 280 nm. The results are very promising in view of the use of these nanomaterials in prospective diagnostic applications.

4. Ferritin-Coated SPIONs as New Cancer Cell Targeted Magnetic Nanocarrier

This chapter is adapted from the article *"Ferritin-Coated SPIONs as New Cancer Cell Targeted Magnetic Nanocarrier",* (Affatigato, Licciardi, et al., 2023).

4.1 Introduction

Among many drug delivery systems, magnetic nanoparticles (MNPs) have gained important attention in the last decades (Laurent et al., 2014). MNPs are a class of theragnostic nanoparticles that can be manipulated under the influence of an external magnetic field. MNPs are commonly composed of magnetic elements, such as iron, nickel, cobalt, and their oxides (Shubayev et al., 2009). As reported in paragraph 1.4, they are classified by their response to an externally applied magnetic field (Mahmoudi et al., 2011). One important advantage for the magnetic nanoparticles is their superparamagnetism which enables their stability and dispersion upon removal of the magnetic field as no residual magnetic force exists between the particles. Below approximately 15 nm, these particles are so small that the cooperative phenomenon of ferromagnetism is no longer observed and they magnetize strongly under an applied magnetic field but do not retain this property once the field is removed. Nanoparticles with this feature are called superparamagnetic particles and they are usually composed of a solid core made up of iron oxides (magnetite, Fe_3O_4, and/or maghemite, Fe_2O_3) coated with biocompatible polymers (Licciardi et al., 2019). The versatility of the superparamagnetic iron oxide nanoparticles (SPIONs) allows the production of theranostic, multimodal and multifunctional devices that can be used for simultaneous drug delivery (Guo et al., 2011) and imaging (Rastogi et al., 2011; Scialabba et al., 2017), biomolecular tracking and cellular labeling (X. Wang et al., 2012).

Although bare SPIONs exert some toxic effects, coated SPIONs have been found to be relatively nontoxic, they were approved by the US Food and Drug Administration (FDA) due to being quite benign toward humans (Zhu et al., 2017). To make SPIONs stable and suitable for biomedical applications, it is important to disperse the nanoparticles in water and modify their surface with small molecular surfactants or polymers. These surfactants or polymers protect the iron oxide core from agglomeration, to provide chemical handles for conjugation with biomolecules, and to reduce non-specific cell interactions. Additionally,

studies have shown that the iron released from degrading SPIONs is metabolized by the body, reducing the potential for long-term cytotoxicity. Various methodologies have been developed to synthesize SPIONs (Y. Lu et al., 2002; Petcharoen & Sirivat, 2012; Rajput et al., 2016; Xu et al., 2007) and to functionalize them with specific coatings (Berry & Curtis, 2003; Mauro et al., 2019). Targeting methods generally fall into one of two categories (Rosen et al., 2012): passive targeting, which relies on the physiological differences between cancerous and normal tissues; and active targeting, which relies on ligands conjugated to the surface of the SPIONs to recognize specific surface markers on cancerous tissue.

The biocompatible coating of SPIONs is essential for most biomedical applications since this increases the stability of the iron oxide core, preventing aggregates formation and allowing functionalization of the surface of the nanoparticles with targeting ligand (Licciardi et al., 2013). There are many natural and synthetic polymers that can be used, such as dextran (Hong et al., 2008, 2009), starch (D. K. Kim et al., 2003), alginate (H. L. Ma et al., 2008; H. li Ma et al., 2007), poly(D,L-lactide-co-glycolide) (Cheng et al., 2008), and poly(ethylene-glycol) (PEG) (Gupta & Curtis, 204; Gupta & Wells, 2004), but also monoclonal antibodies, folic acid, biotin, transferrin, lactoferrin, albumin, insulin, growth factors, etc (Gupta et al., 2003). Among these, I used a specific ferritin, the Humanized *Archaeoglobus fulgidus* Ferritin (HumAfFt), as a biomimetic coating for SPIONs. As explained in paragraph 1.5.4, HumAfFt is an engineered ferritin characterized by the peculiar salt-triggered assembly-disassembly of the hyperthermophile *Archaeoglobus fulgidus* ferritin and which is successfully endowed with the human H homopolymer recognition sequence by the transferrin receptor (TfR1 or CD71), overexpressed in many cancer cells in response to the increased demand of iron. The aim of this study was to use HumAfFt as a coating material for 10 nm SPIONs, in order to create a new magnetic nanocarrier able to discriminate cancer cells from normal cells and to be influenced by a magnetic field as well. The obtained complex (HumAfFt-SPIONs) was characterized in terms of HumAfFt and SPIONs content, morphology, size, and stability. Moreover, the preferential target of the HumAfFt-SPIONs towards cancer cells was demonstrated *in vitro* by biological assays.

4.2 Materials and methods

Expression and Purification of HumAfFt

The synthetic gene encoding for the HumAfFt, optimized for the expression in *Escherichia coli* cells, was synthesized by Gene Art (ThermoFisher) and subcloned into a pET22b vector

(Novagen) between NdeI and XhoI restriction sites. The recombinant plasmid was transformed into *Escherichia coli* BL21(DE3) for protein expression upon induction with 1 mM IPTG (isopropyl-β-D-1-thiogalactopyranoside) at OD_{600} = 0.6 for 16 h. After 16 h, the bacterial cells were harvested by centrifugation. The bacterial paste was resuspended in 20 mM HEPES buffer containing 50 mM $MgCl_2$ in the presence of a protease Inhibitor Cocktail (Basel, Switzerland). After sonication, the soluble fraction was subjected to two $(NH_4)_2SO_4$ precipitations (50% and 70%). The pellet from 70% $(NH_4)_2SO_4$ was recovered by centrifugation and extensively dialyzed versus 10 mM sodium phosphate buffer pH 7.2 containing 20 mM $MgCl_2$. The sample was digested with deoxyribonuclease I from bovine pancreas (Merck, Darmstadt, Germany), and DNA removal was achieved in a single step by means of crossflow ultrafiltration using a single Vivaflow 200 module (Sartorius) with a cutoff of 100 kDa, coupled to a Masterflex L/S pump system. Crossflow ultrafiltration was also used in diafiltration mode to exchange the buffer with 20 mM HEPES pH 7.4 containing 50 mM $MgCl_2$. Protein purity was monitored by SDS-PAGE (Biorad, Hercules, CA, USA). DNA removal was followed by measuring a 260/280 nm ratio using a Jasco V-650 spectrophotometer (JASCO Deutschland).

As the final purification step, the protein was loaded onto a HiLoad 26/600 Superdex 200 pg column previously equilibrated in the same buffer using an ÄKTA-Prime system (GE Healthcare) following the absorbance at 280 nm. Purified protein was concentrated to 1 mg/mL using AmiconUltra-15 centrifugal filter devices (100 kDa cut-off). Protein concentration was determined using an extinction coefficient of 32,430 $M^{-1}cm^{-1}$ at 280 nm. The protein purity was assessed by SDS-PAGE and the correct assembly by analytical size-exclusion chromatography, using an Agilent AdvanceBio SEC 300 Å, 7.8 × 150 mm, 2.7 µm, LC column in isocratic mode at a flow rate of 1 mL/min with a mobile phase composition of 20 mM HEPES 50 mM $MgCl_2$ pH 7.4 (UV detection at 220 and 280 nm).

Preparation of HumAfFt-coated SPIONs

Superparamagnetic iron oxide nanoparticles (SPIONs) (10 nm average particle size) water dispersion were purchased from Sigma Aldrich (Milan, Italy). The HumAfFt was disassembled removing $MgCl_2$ by dialysis versus demineralized water (Milli-Q quality) using a molecular porous membrane tubing MWCO: 3.5 kD (Spectral/Por Dialysis Membrane Standard RC Tubing). Finally, the HumAfFt was reassembled in the presence of the SPIONs (HumAfFt-SPION ratio=1) and by restoring the concentration of $MgCl_2$ to 50 mM. HumAfFt-SPION was collected and purified using an external magnet.

Characterization of the HumAfFt-SPIONs

Size and zeta potential values of HumAfFt, SPIONs, and the new complex HumAfFt-SPIONs were recorded by Dynamic Light Scattering (DLS) analysis (Malvern Zetasizer NanoZS, Worcestershire, UK). A complex concentration of 0.06 mg/mL at pH 7.4 was used for DLS and Z-potential measurements (mV), at 25°C using an instrument fitted with a 532 nm laser at a fixed scattering angle of 173°. Thermogravimetric analysis (TGA) was performed using a LABSYS Evo STA TGA-DSC (Caluire, France) at heating rates of 7°C/min between 30°C and 500°C and alumina crucibles were used in all experiments. Nitrogen purge gas was used with a flow rate of 5 mL/min.

An FTIR spectrometer (Bruker ATR FTIR, model ALPHA, Ettlingen, Germany) in attenuated total reflection (ATR) mode, equipped with a diamond measurement interface and controlled by OPUS software, was used to collect IR spectra. Spectra have been acquired in the range 4000–400 cm^{-1} with a resolution of 2 cm^{-1}. Each measurement is the result of the average of 64 scans. The ATR diamond crystal was cleaned with 70% ethanol/water and a background measurement was performed between each sample. Sample was compressed against the diamond to ensure good contact between sample and ATR crystal.

Scanning electron microscopy (SEM) and Energy Dispersive X-ray (EDX) analysis were performed using a scanning electron microscope, ESEM Philips XL30 (Massachusetts, USA). Samples were dusted on a double-sided adhesive tape previously applied on a stainless steel stub. The HumAfFt-SPIONs were then sputter-coated with gold prior to microscopy examination.

Atomic force microscopy (AFM) analyses were performed in Tapping mode in air by a Bruker Dimension FastScan microscope (Santa Barbara, CA, USA) equipped with closed-loop scanners. Triangular FastScan A probes (resonance frequency = 1400 KHz, Tip radius = 5 nm) were used for acquisitions. The nanosystem was dropped onto a freshly cleaved mica surface as a thin layer aqueous dispersion (0.001 $\mu g/mL^{-1}$) and dried overnight before observation.

Cytotoxicity Assay

The cytotoxicity assays were carried out by the tetrazolium salt (MTS) assay, using a commercially available kit (Cell Titer 96 Aqueous One Solution Cell Proliferation assay, Promega). Human breast adenocarcinoma (MCF7) and normal human dermal fibroblast (NHDF) cell lines were used for the experiments.

MCF7 and NHDF cell lines were obtained from the Laboratory of Cell Cultures of Advanced Technologies Network Center (ATEN Center) of the University of Palermo. Cells were seeded at a density of 2.5 × 104 cells/well in 96-well plates in Dulbecco's modified Eagle's medium (DMEM, Euroclone, Italy) containing 10 vol% fetal bovine serum (FBS), 1 mM glutamine, 1% penicillin and 2% amphotericine B (0.25 mg/mL) (Sigma-Aldrich, Italy), under standardized conditions (95% relative humidity, 5% CO_2 and 37 ◦C) and cultured for 24 h. Starting dispersions of SPIONs or HumAfFt-SPIONs (10, 50, 150 μg/mL) were prepared in the same medium, and 150 μL of each dispersion was added per well. Untreated cells were used as negative control. After 4 and 24 h of incubation, the medium was removed and cells were washed with DPBS. Then 150 μL of fresh medium and 20 μL of a MTS solution were added to each well. Plates were incubated for an additional 2 h at 37°C. Then, the absorbance at 492 nm was measured using a microplate reader (PlateReader AF2200, Eppendorf, Hamburg, Germany). MTS assay was performed in triplicate and the viability was expressed as percentage obtained from the ratio between each sample with respect to their negative control (100% of cell viability).

Uptake Studies by Fluorescence Microscopy

The uptake of HumAfFt-SPIONs was evaluated on culture of normal and cancer cell lines by fluorescence microscopy. NHDF and MCF7 cells were seeded at a density of 105 cell type/well into 8-well plates and cultured for 24 h in Dulbecco's modified Eagle's medium (DMEM, Euroclone, Italy) containing 10 vol% fetal bovine serum (FBS), 1 mM glutamine, 1% penicillin and 2% amphotericine B (0.25 mg/mL) (Sigma-Aldrich, Milan, Italy), under standardized conditions (95% relative humidity, 5% CO_2 and 37°C). The complex HumAfFt-SPIONs were labeled with the fluorescein sodium salt (Sigma-Aldrich) according to the manufacturer's standard protocol.

After 24 h, cells were incubated with 350 μL per well of cell culture medium containing HumAfFt-SPIONs at a final complex concentration per well of 150 μg/mL for 4 h and 24 h. Following, the cells were washed with DPBS and analyzed by fluorescence microscopy. The images were recorded using an Axio CamMRm (Zeiss, Jena, Germany). Untreated cells were used as negative control to set the auto-fluorescence.

Statistical Analysis

The student's two-tailed t-test was used to carry out statistical analysis. The criterion $p < 0.05$ was chosen to assign statistical significance. Data are the average of three experiments ± standard deviation.

4.3 Results and discussion

4.3.1 Preparation and characterization of HumAfFt-SPIONs

The synthetic gene encoding for HumAfFt was optimized for the expression in *Escherichia coli* BL21(DE3) cells and the recombinant protein was expressed at a very high level. The results of the purification process are shown in Figure 4.1.

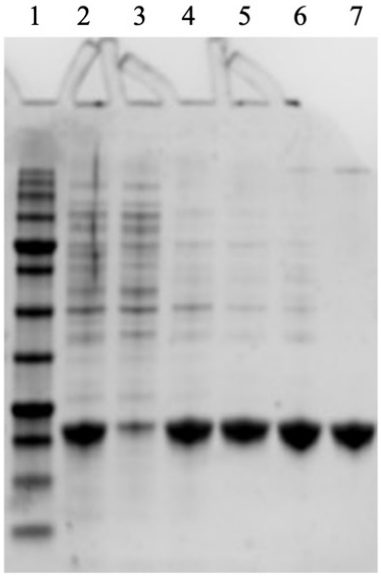

Figure 4.1 SDS-PAGE of the products of purification of HumAfFt. Line 1 is the marker; line 2 is the product after sonication; line 3 is the fraction at 50% $(NH_4)_2SO_4$; line 4 is the fraction at 70% $(NH_4)_2SO_4$; line 3 is the product after the heat treatment; line 6 is the protein pre-filtration and line 7 is protein post-filtration.

Additionally, the high purity (accounting up to 99%) was further confirmed by the HP-SEC analysis (Figure 4.2), revealing that HumAfFt eluted as a single peak. This observation provides evidence supporting the correct assembly of the ferritin in its 24-mer structure.

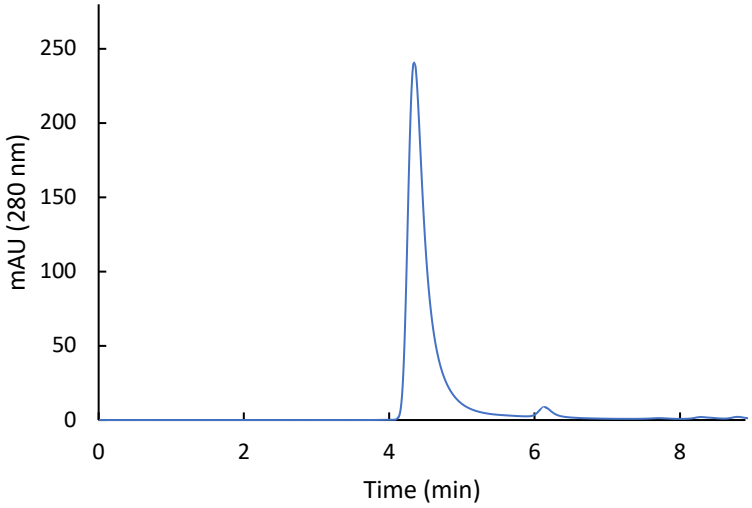

Figure 4.2 HPL-SEC chromatogram of purified HumAfFt.

The disassembled HumAfFt was incubated in the presence of the SPIONs (HumAfFt-SPION ratio = 1) and then the concentration of $MgCl_2$ was restored to 50 mM (Figure 4.3).

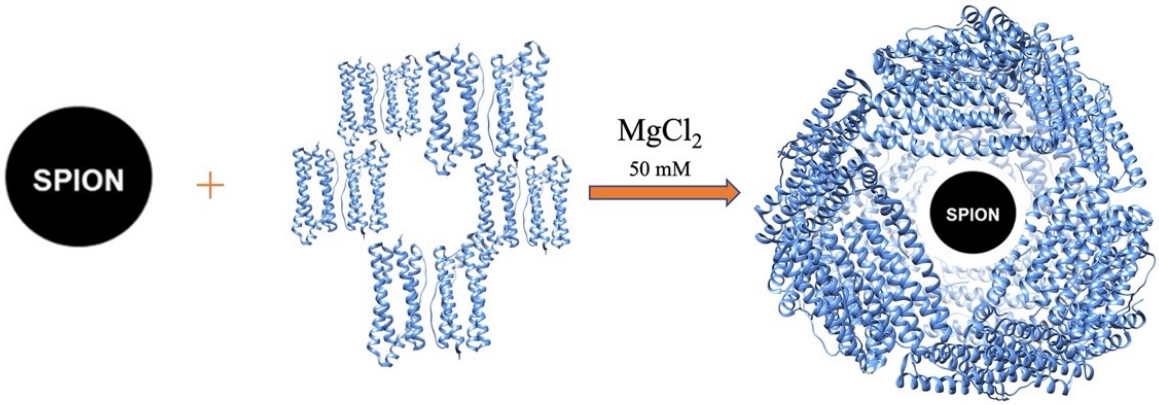

Figure 4.3 Schematic representation of the SPIONs coating with HumAfFt. The disassembled HumAfFt was incubated in the presence of the SPIONs and by restoring the concentration of $MgCl_2$ to 50 mM.

The superparamagnetic behavior of HumAfFt-SPIONs at room temperature was observed macroscopically by attracting HumAfFt-SPIONs dispersed in water with an external magnet, as shown in Figure 4.4. Upon the magnet application outside the vial, HumAfFt-SPIONs were rapidly recovered and accumulated near the magnet, whereas a homogeneous

nanoparticle dispersion was established again as the magnetic field was removed, suggesting superparamagnetic behavior and good physical stability of the coated nanoparticle. The above procedure resulted in a valid method for recovering and purifying HumAfFt-SPIONs, warranting the elimination of not assembled ferritin.

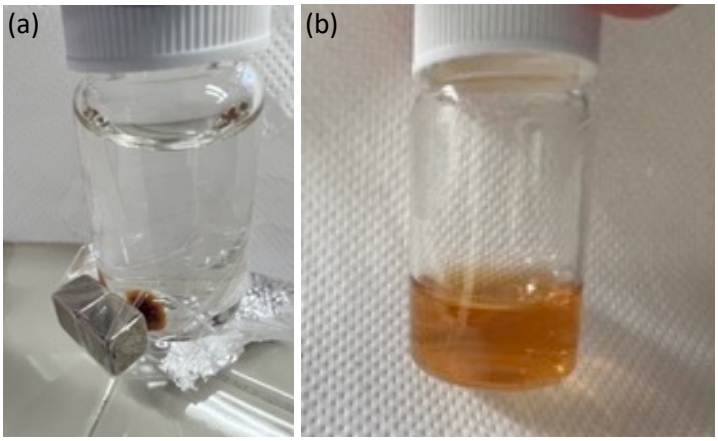

Figure 4.4 Pictures of a HumAfFt-SPIONs Milli-Q water dispersion during (a) and after (b) the application of an external magnet.

The thermogravimetric analysis of the solid residue of HumAfFt-SPIONs showed that the new nanosystem has a water content of 1% and a Fe_3O_4 content of 40%, measured as sample weight loss between 25 and 560 °C (Figure 4.5).

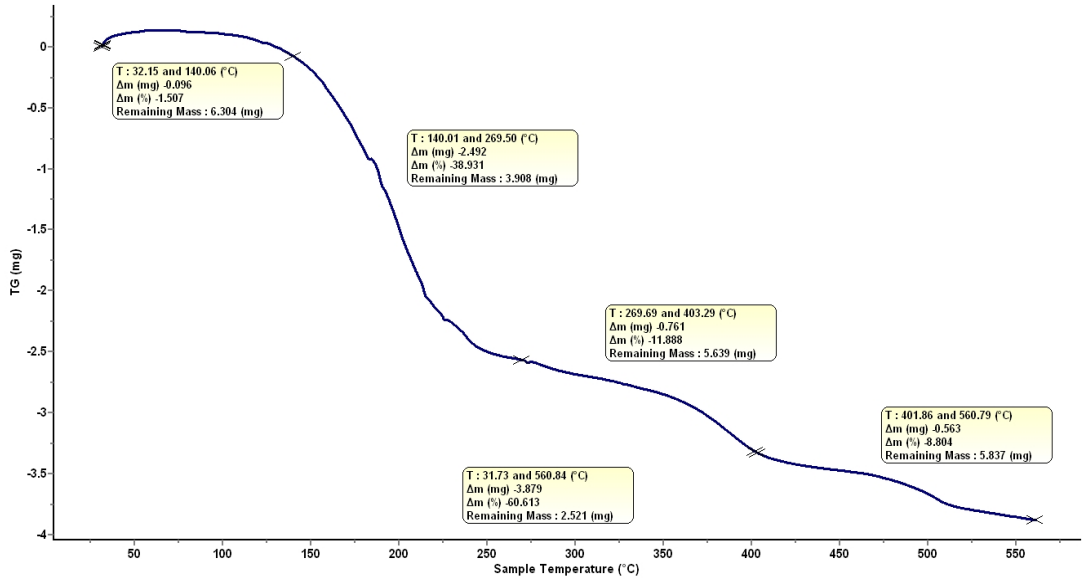

Figure 4.5 TGA analysis of HumAfFt-SPIONs.

ATR spectra acquired for each sample are reported in absorbance mode in the range 4000–400 cm^{-1} (Figure 4.6) and present expected absorption peaks previously reported in the literature (Piazza et al., 2020), confirming the composition of prepared HumAfFt-SPIONs. The peaks around 570 cm^{-1} and 630 cm^{-1} are attributed to the stretching vibrations from Fe-O and confirm the existence of nanoparticles with magnetite core (Wierzbinski et al., 2018). Broad bands at the region 3000–3600 cm^{-1} corresponding to the vibrations of the hydroxyl group (O-H) are present in HumAfFt and HumAfFt-SPIONs spectra, in these compounds the water content is higher than in the SPIONs. Sharp peaks at 1650 cm^{-1} and at 1550 cm^{-1} in the HumAfFt spectrum are assigned to the N–H bending vibration of primary amines. The bands in the range 1450 cm^{-1} and 1100 cm^{-1} were attributed to C-H deformation vibrations and the C-O stretching, respectively. The appearance of these peaks in the HumAfFt-SPIONs spectrum suggests that the HumAfFt is coating the SPION surface.

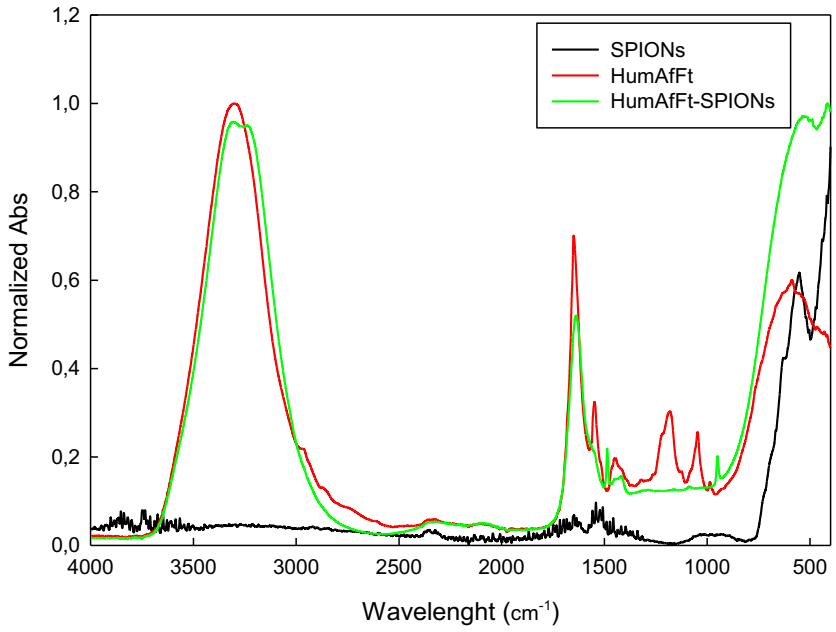

Figure 4.6 ATR-FTIR spectra of HumAfFt, SPIONs, and HumAfFt-SPIONs complex.

The morphology and the size of prepared HumAfFt-SPIONs were evaluated by AFM analysis. AFM images (Figure 4.7) clearly showed a spherical particle population with a mean diameter size between 30 and 39 nm.

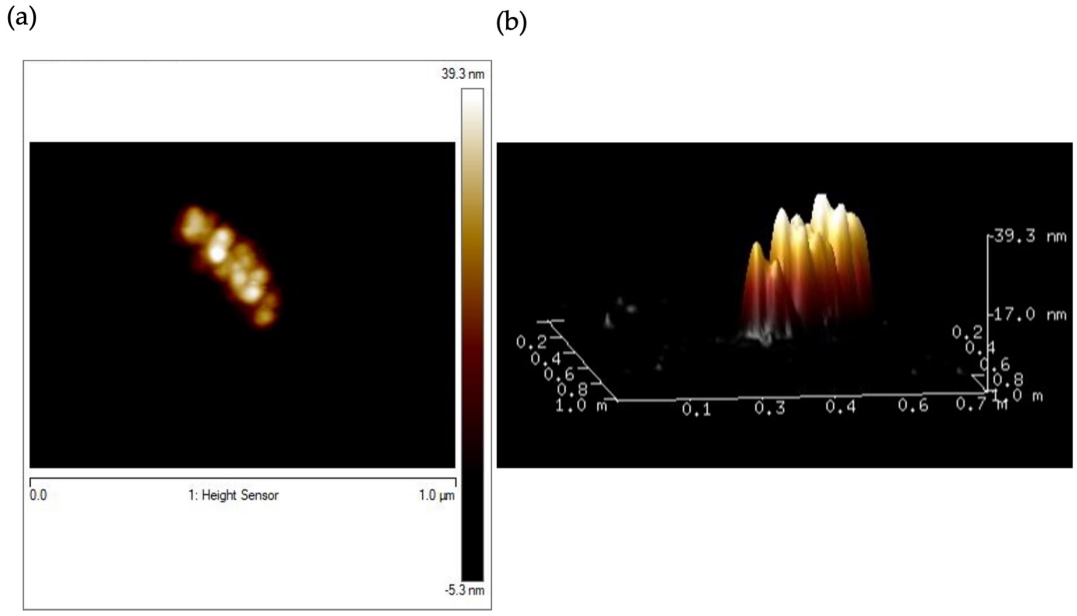

Figure 4.7 (a) 2D AFM micrograph and (b) 3D AFM image of HumAfFt-SPIONs.

With the aim of confirming the presence of a ferritin coating around HumAfFt-SPIONs, an Energy Dispersive X-Ray (EDX) analysis was performed by SEM analysis (Mauro et al., 2019) (Figure4.8a-d). It revealed that HumAfFt-SPIONs aggregates are coated with oxygen and carbon-bearing organic material, such as ferritin; no iron is visible on the surface, demonstrating that the SPIONs constitute the core of the nanostructure. As a control, an elemental analysis of uncoated SPIONs was performed (Figure 4.8e). Differently, this analysis demonstrated that the same SPIONs without coating are composed of iron and oxygen in the ratio 89.8% and 10.2%, respectively.

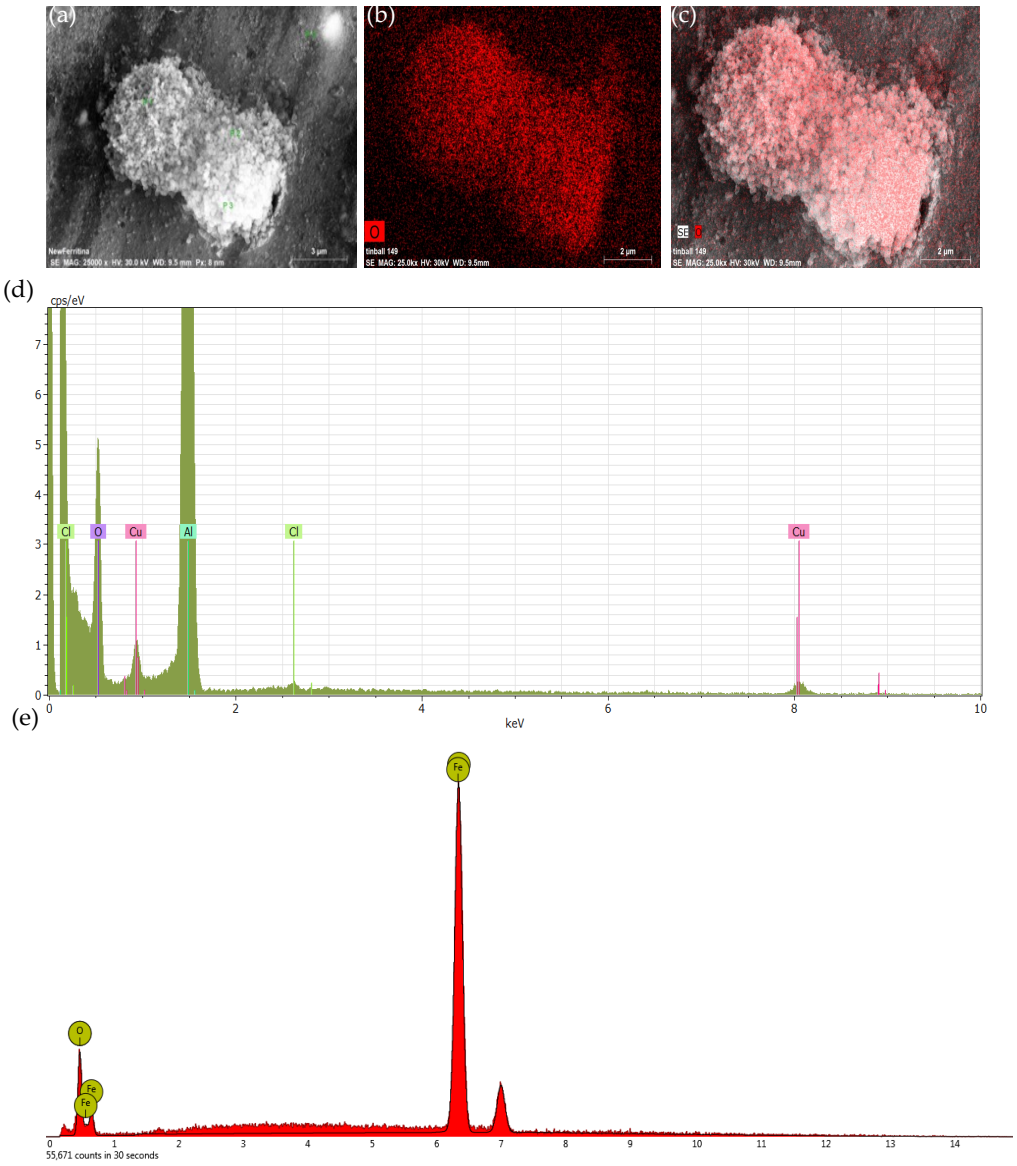

Figure 4.8 EDX analysis of the HumAfFt-SPIONs complex aggregates: (a) bright, (b, c) mapping of carbon and oxygen (red), (d) elemental analysis graph of HumAfFt-SPIONs, (e) elemental analysis graph of uncoated SPIONs.

4.3.2 Stability Studies of the HumAfFt-SPIONs

The stability of nanoparticles is an important parameter concerning applications of nanovectors. These should be stable in terms of size when dispersed in a physiological medium avoiding aggregation phenomena. Therefore, the stability of the HumAfFt-SPIONs was studied by measuring the hydrodynamic diameter and zeta potential by DLS analysis. As shown in Table 4.1, HumAfFt-SPIONs were found to be stable with low PDI maintaining

a hydrodynamic diameter size below 150 nm in the hydrated state (Licciardi et al., 2022). This characteristic was maintained for up to one month, when the analysis was repeated. Furthermore, the surface potential (Zp) of SPIONs was found to be negative (−31.3) before coating, then, decreases to −5.1 when they are coated by the HumAfFt. This finding is strictly coherent with the deposition of ferritin units around the SPIONs surface. The lowering of the polydispersity index (PDI) value further demonstrates the formation of a homogeneous and stable nanosystem.

Table 4.1 DLS data (zeta average and polydispersity index) and Z-potential values of HumAfFt-SPIONs in Milli-Q water (0.06 mg/mL).

	Za (nm)	PDI	Zp (mV)
HumAfFt	20.42	0.392	-4.1
SPIONs	27.65	0.295	-31.3
HumAfFt-SPION	145.8	0.202	-5.1

4.3.3 Cytotoxicity Assay

The evaluation of the cytotoxicity effect of a novel material yields important data for predicting the safety of the new system for in vivo applications. Toward this goal, the viability of two different cell lines was assessed in the presence of various concentrations of HumAfFt-SPIONs. Cell viability was estimated by the MTS assay using human breast adenocarcinoma (MCF7) and normal human dermal fibroblasts (NHDF) cell lines. MCF7 is a cancer cell line where the transferrin receptor is overexpressed, and it is used to investigate the anti-cancer activity of many drugs and the associated mechanism of action; NHDF is a non-tumoral cell line extensively used as a model of normal cells to screen cytotoxicity of novel compounds or carriers. These cells were incubated with uncoated SPIONs and HumAfFt-SPIONs at three different concentrations of 10, 50, and 150 μg/mL, for 4 and 24 h. The results, in terms of cell viability (%) as a function of sample concentration, are shown in Figure 4.9. These results show that the viability of both normal and cancer cells was always above 80% for all the tested concentrations, both after 4 and 24 h of incubation, indicating a good cytocompatibility of the new vector HumAfF-SPIONs. No statistical significance was revealed in the cell viability of all tested samples at the same concentration and incubation time ($p > 0.05$).

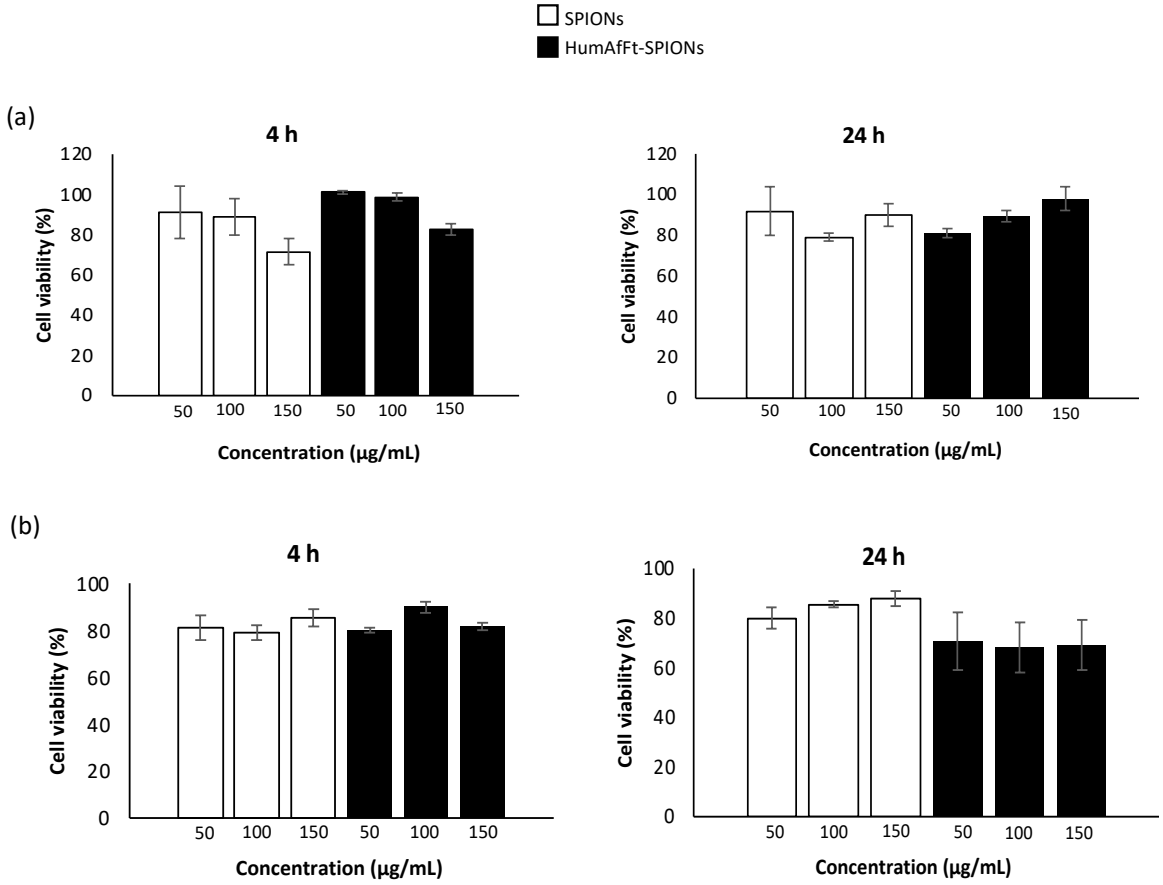

Figure 4.9 Cell viability of SPIONs (white) and HumAfFt-SPIONs (black) in MCF7 (a) and NHDF (b) cells after 4 and 24 h of incubation. Statistical significance (Student's two-tailed t-test): $p > 0.05$ for all samples at the same concentration and incubation time.

4.3.4 Uptake Studies in Cell Culture Experiments by Fluorescence Microscopy

To further investigate the preferential targeting of HumAfFt-SPIONs into tumor cells, uptake experiments of cancer and normal cells were performed. MCF7 and NHDF cell lines were incubated with fluorescein labelled HumAfFt-SPIONs for 4 and 24 h; then particle internalization was investigated by fluorescence microscopy. Analysing the obtained images (Figure 4.10), the internalization of HumAfFt-SPIONs is markedly higher in MCF7 cells in comparison with NHDF, endorsing the excellent capacity of HumAfFt-SPIONs to discriminate between cancer and normal cells. It was noticed that the ability of magnetic

nanoparticles to discriminate their uptake between tumoral and non-tumoral cells strongly depends on the presence of HumAfFt that improves the nanoparticles internalization; this result is supported by the fact that the transferrin receptors are overexpressed on the cancer cell membranes (De Turris et al., 2017). Finally, the merge images (c, f, i, and l) confirmed that the HumAfFt-SPIONs predominantly have a cytoplasmic localization in MCF7 cells (images i and l) starting from 4 h post incubation.

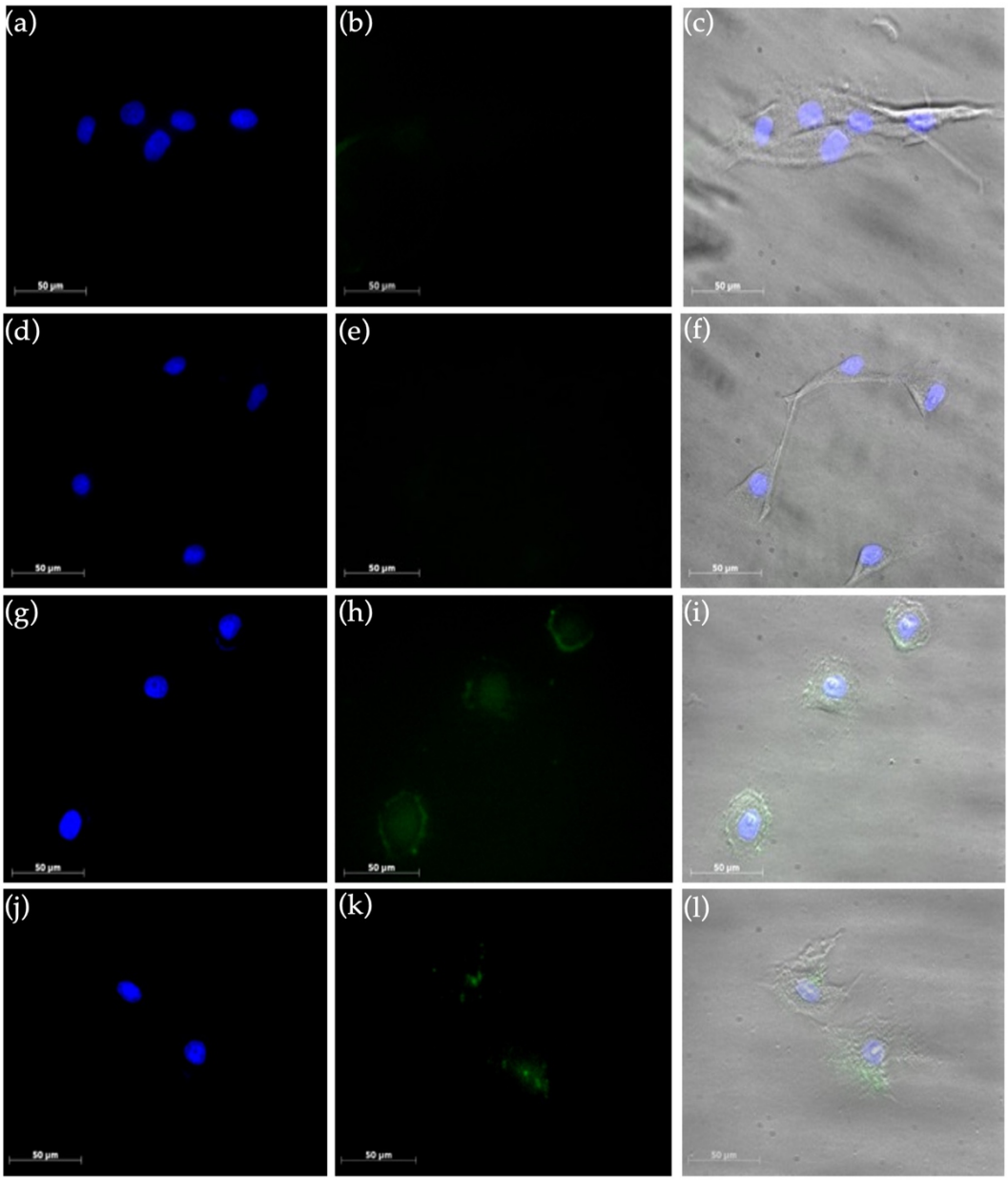

Figure 4.10 Uptake of HumAfFt-SPIONs in NHDF (images a-f) and MCF7 (images g-l) after 4 h (a-c,g-i) and 24 h (d-f, j-l) of incubation. Cell nuclei were stained with DAPI (blue in images a,d,g and j) and Fluorescein-labelled HumAfFt-SPIONs are visualized in green (images b,e,h,k).

4.4 Conclusion

A new magnetic nanocarrier targeted toward cancer cells was developed. In detail, an engineered ferritin was synthetized and used as a coating material for 10 nm SPIONs. For this purpose, the engineered ferritin was the humanized Archaeoglobus fulgidus ferritin (HumAfFt) characterized by the peculiar salt-triggered assembly-disassembly of the hyperthermophile *Archaeoglobus fulgidus* ferritin and which is successfully endowed with the human H homopolymer recognition sequence by the transferrin receptor (TfR1 or CD71), overexpressed in many cancer cells in response to the increased demand of iron. The newly engineered ferritin assembled in a distinctive tetrahedral geometry as a result of a particular packing between four hexameric units into a unique 24-mer structure, representing an ideal scaffold to host molecules or nanoparticles within the internal cavity. Thanks to the salt-triggered assembly mechanism and to the 24-mer typical structure of the ferritin, 10 nm diameter SPIONs were successfully coated with the HumAfFt.

The new complex HumAfFt-SPIONs formation was confirmed by ATR-FTIR and EDX techniques. HumAfFt-SPIONs were found to be stable with low PDI and a hydrodynamic diameter size below 150 nm in the hydrated state and about 40 nm in the dry state. The obtained complex maintained the superparamagnetic property of SPIONs and the presence of ferritin coating was confirmed using the EDX analysis.

Biological studies on MCF7 and NHDF cell lines have shown that HumAfFt-SPIONs do not induce toxicity in cells even at high concentrations. Uptake assay confirmed the magnetic nanocarrier's ability to preferentially accumulate into MCF7 cancer cells versus NHDF (non-tumoral cells), in agreement with the fact that the TfR1 is overexpressed in a cancer cell. After only 4 h post incubation, the HumAfFt-SPIONs predominantly have a cytoplasmic localization in MCF7 cells. Therefore, HumAfFt-SPIONs represent an excellent theranostic tool with high stability and biocompatibility. The obtained results stimulate further exploration of cancer-targeted therapies.

5. Ferritin-Coated SPIONs as a smart magnetic nanocarrier

5.1 Introduction

Among various types of nanomaterials, SPIONs have been extensively investigated and used in numerous in vivo applications (Hola et al., 2015; Laurent et al., 2014; Vangijzegem et al., 2019; Zhu et al., 2017). They are usually composed of a solid core made up of iron oxides (magnetite, Fe_3O_4, and/or maghemite, Fe_2O_3) coated with biocompatible polymers (Licciardi et al., 2019). After the intracellular uptake, SPIONs are metabolized in the lysosomes into a soluble, non-superparamagnetic form of iron that becomes part of the normal iron pool (e.g., ferritin, hemoglobin) (Y.-X. J. Wang, 2011). In the field of medical imaging, SPIONs are recognized for their role as contrast agents in MRI (Estelrich et al., 2015; Scialabba et al., 2017; Wierzbinski et al., 2018). Under standard magnetic field strengths used in MRI scanners, SPIONs within the specified region can become magnetically saturated, resulting in a significant locally perturbing dipolar field. As a result, there is a noticeable reduction in proton relaxation (T_2 relaxation) during the MRI process, resulting in a 'darker' image of the targeted area in contrast to the biological background (Mao et al., 2016).

Besides their use in MRI, SPIONs also have great potential for therapeutic applications (Mauro et al., 2019). They can induce local heat enhancement when exposed to an alternating magnetic field, leading to what is known as magnetic hyperthermia (Kumar & Mohammad, 2011). This feature is highly effective for eradicating cancer cells, as they are unable to withstand temperatures between 42-49°C – a range that healthy cells can tolerate (Pham et al., 2017). Other biomedical applications concern tissue repair, immunoassays, drug delivery and cell separation (Gupta & Gupta, 2005). For any of these types of applications, the properties of SPIONs strongly depend on their size and shape (Laurent et al., 2008). Typically, biomedical applications require inorganic cores with sizes below 100 nm and special consideration should be given to selecting a coating that ensures excellent stability and stealth of the nanoparticles in biological media. Particle coating can be achieved through two distinct methods: a) adsorption, in which small organic molecules are attached to the surface of nanoparticles using anchoring groups like silanes, carboxylates, or organophosphorus, that have a high affinity with the metal oxide surface (Mallakpour &

Madani, 2015); or b) encapsulation, where SPIONs are enclosed within a self-assembled amphiphilic structure, resulting in the formation of magnetic nanoassemblies (Gupta et al., 2007; Ling et al., 2015) that display excellent dispersibility and biocompatibility. Selecting the correct coating agent is crucial since this will affect particle cellular uptake, protein adsorption and interaction with cells and tissues, and biokinetic parameters such as biodistribution, biodegradation, metabolism and elimination. Several polymer-coated SPION-based contrast agents, such as Feridex, Resovist, Ferumoxtran-10 and Clariscan, are already in clinical use for general imaging applications (Y.-X. J. Wang, 2011). However, since these agents lack target specificity, they cannot discern between cancer and normal tissues. For this reason, I decide to use the Humanized *Archaeglobus fulgidus* ferritin (HumAfFt) as a particle coating for SPIONs (Affatigato, Licciardi, et al., 2023). HumAfFt is an engineered ferritin that exhibits distinct salt-induced assembly-disassembly features of the hyperthermophile *Archaeoglobus fulgidus* ferritin (Calisti et al., 2017) and which is successfully modified to include the human H homopolymer recognition sequence, which enables recognition by the transferrin receptor (TfR1 or CD71) (L. Li et al., 2010), overexpressed in various cancer cells that require extra iron (Chan et al., 2014; Palombarini et al., 2019). To date, the HumAfFt has demonstrated successful applications in encapsulating and delivering drugs, therapeutic proteins, and small nucleic acids to tumor cells (Incocciati et al., 2022; Macone et al., 2019; Palombarini et al., 2021).

Building on the unique properties of this nanoparticle and the obtained results, I employed the HumAfFt as a coating for SPIONs to create a new smart nanoparticle that can combine the targeted properties of HumAfFt and the theranostic applications of SPIONs. The ability of HumAfFt to direct SPIONs towards tumor cells represents the key point in the targeted use of SPIONs. Here, the new complex has been characterized in terms of size and morphology and its magnetic properties were investigated in detail by electron paramagnetic resonance (EPR) technique and thermal dependence of magnetization. A first image of the new HumAfFt-SPIONs as a contrast agent in MRI was also obtained.

5.2 Material and Methods

Expression and Purification of HumAfFt

The synthetic gene encoding for the HumAfFt, optimized for the expression in *Escherichia coli* cells, was synthesized by Gene Art (ThermoFisher) and subcloned into a pET22b vector

(Novagen) between NdeI and XhoI restriction sites. The recombinant plasmid was transformed into *Escherichia coli* BL21(DE3) for protein expression upon induction with 1 mM IPTG (isopropyl-β-D-1-thiogalactopyranoside) at OD_{600} = 0.6 for 16 h. After 16 h, the bacterial cells were harvested by centrifugation. The bacterial paste was resuspended in 20 mM HEPES buffer containing 50 mM $MgCl_2$ in the presence of a protease Inhibitor Cocktail (Basel, Switzerland). After sonication, the soluble fraction was subjected to two $(NH_4)_2SO_4$ precipitations (50% and 70%). The pellet from 70% $(NH_4)_2SO_4$ was recovered by centrifugation and extensively dialyzed versus 10 mM sodium phosphate buffer pH 7.2 containing 20 mM $MgCl_2$. The sample was digested with deoxyribonuclease I from bovine pancreas (Merck, Darmstadt, Germany), and DNA removal was achieved in a single step by means of crossflow ultrafiltration using a single Vivaflow 200 module (Sartorius) with a cutoff of 100 kDa, coupled to a Masterflex L/S pump system. Crossflow ultrafiltration was also used in diafiltration mode to exchange the buffer with 20 mM HEPES pH 7.4 containing 50 mM $MgCl_2$. Protein purity was monitored by SDS-PAGE (Biorad, Hercules, CA, USA). DNA removal was followed by measuring a 260/280 nm ratio using a Jasco V-650 spectrophotometer (JASCO Deutschland).

As the final purification step, the protein was loaded onto a HiLoad 26/600 Superdex 200 pg column previously equilibrated in the same buffer using an ÄKTA-Prime system (GE Healthcare) following the absorbance at 280 nm. Purified protein was concentrated to 1 mg/mL using AmiconUltra-15 centrifugal filter devices (100 kDa cut-off). Protein concentration was determined using an extinction coefficient of 32,430 $M^{-1}cm^{-1}$ at 280 nm. The protein purity was assessed by SDS-PAGE and the correct assembly by analytical size-exclusion chromatography, using an Agilent AdvanceBio SEC 300 Å, 7.8 × 150 mm, 2.7 µm, LC column in isocratic mode at a flow rate of 1 mL/min with a mobile phase composition of 20 mM HEPES 50 mM $MgCl_2$ pH 7.4 (UV detection at 220 and 280 nm).

Preparation of HumAfFt-coated SPIONs

Superparamagnetic iron oxide nanoparticles (SPIONs) (10 nm average particle size) water dispersion were purchased from Sigma Aldrich (Milan, Italy). The HumAfFt was disassembled by dialysis with demineralized water (Milli-Q quality) using a molecular porous membrane tubing MWCO: 3.5 kD (Spectral/Por Dialysis Membrane Standard RC Tubing) pH 7.4 in order to remove the $MgCl_2$. Finally, the HumAfFt was reassembled in the

presence of the SPIONs and by restoring the concentration of $MgCl_2$ to 50 mM. HumAfFt-SPION was collected and purified using an external magnet.

Circula Dichroism

Circular Dichroism (CD) spectroscopy was performed using a Chirascan CD spectrophotometer (Applied Photophysics, Surrey, UK) with a LAAPD detector and Chirascan Spectrometer Control Panel software version 4.4 (Applied Photophysics). Far-UV CD analysis was performed from 190 to 260 nm with a 0.5 nm step size. All measurements were performed at 25° using a 1 mm precision cuvette (Hellma GmbH, Müllheim, Germany), and each sample was scanned 3 times and averaged, no smoothing was used. All sample solvents were also scanned under identical conditions and subtracted from the sample spectra. Raw data were analyzed using BeStSel – Protein Circular Dichroism Spectra Analysis (https://bestsel.elte.hu/index.php).

Absorption and emission analyses

Samples (HumAfFt-SPIONs) of 500 µL were scanned in a Cell Quartz glass cuvette with 3 x 3 mm light path (Hellma Analytics, Germany) while measuring the absorbance at 225 – 600 nm, and fluorescence at 281- 800 nm with excitation at 280 nm. The measurements were taken every 60 s for one hour to analyze the stability of the samples. The spectra were obtained using Labbot instrument (ProbationLabs, Sweden).

EPR

EPR spectra of SPIONs and HumAfFt-SPIONs transferred into sealed tubes of 5 mm internal diameter were recorded using a X band (microwave frequency ≅ 9.7 GHz) Bruker ELEXSYS E 500 (Germany) with ER 4122SHQ type cavity resonator. EPR spectra of the samples were displayed in the form of the first derivative of the absorption peak plotted against magnetic field. All measurements were made at room temperature (291 K). Spectrometer operating conditions are 9.75 GHz, 3300 field set, 100 Hz field modulation, 4G peak-to-peak modulation amplitude and 2.4 mW microwave power to determine signal linewidths, and g-values.

Magnetization

Measurements of the magnetization as a function of temperature were performed on a Quantum Design MPMS-XL superconducting quantum interference device (SQUID). For the zero field cooled (ZFC) measurements, the sample was cooled to 2 K without an applied magnetic field, and then the magnetization was recorded in the temperature range 2 – 260 K with an applied static magnetic field of 1000 Oe. For the field cooled (FC) measurements, the sample was cooled down to 2 K in an applied static magnetic field of 1000 Oe, and then the magnetization was measured in the temperature range 2 – 260 K retaining the static magnetic field.
The ZFC and FC measurements were performed on dry samples of SPIONs and HumAfFt-SPIONs; a small amount of n-hexadecane was used to fixate the samples to avoid orientation in the magnetic field.

MRI

MRI measurements of HumAfFt and HumAfFt-SPIONs in aqueous dispersion were performed with a 7 T horizontal bore PharmaScan 70/16 US scanner (Bruker, Ettlingen, Germany) using a 23 mm transmit/receive volumetric coil. A respiration-triggered gradient echo sequence (TE) = 35.0 ms and a triggered T_2_Turbo RARE sequence was selected for T_2 imaging.

4.3 Results and discussion

Preparation of HumAfFt-SPIONs

The HumAfFt was overexpressed in E. coli and purified with high yields (Figure 4.1). The resulting ferritin is correctly assembled as a 24-mer, as demonstrated by High-Performance Size Exclusion Chromatography (HP-SEC) analysis (Figure 4.2) and maintains its distinctive dissociation/association capabilities mediated by divalent cations. The combination of its negative internal charge and size renders this nanoparticle particularly well-suited for hosting superparamagnetic iron oxide nanoparticles (SPIONs) with an average size of 10 nm. To facilitate the encapsulation, the nanoparticle was dissociated by removing magnesium chloride. The disassembled HumAfFt was incubated in the presence

of tSPIONs, then the $MgCl_2$ concentration was increased to 50 mM (Figure 5.1). To purify the HumAfFt-SPIONs complex and eliminate any non-assembled ferritin, a magnet was placed outside the vial (Affatigato, Licciardi, et al., 2023). The stable HumAfFt-SPIONs complex was quickly recovered and collected near the magnet. Removal of the magnetic field resulted in the dispersion of the nanocomplex, indicating the superparamagnetic behaviour of the coated nanoparticle.

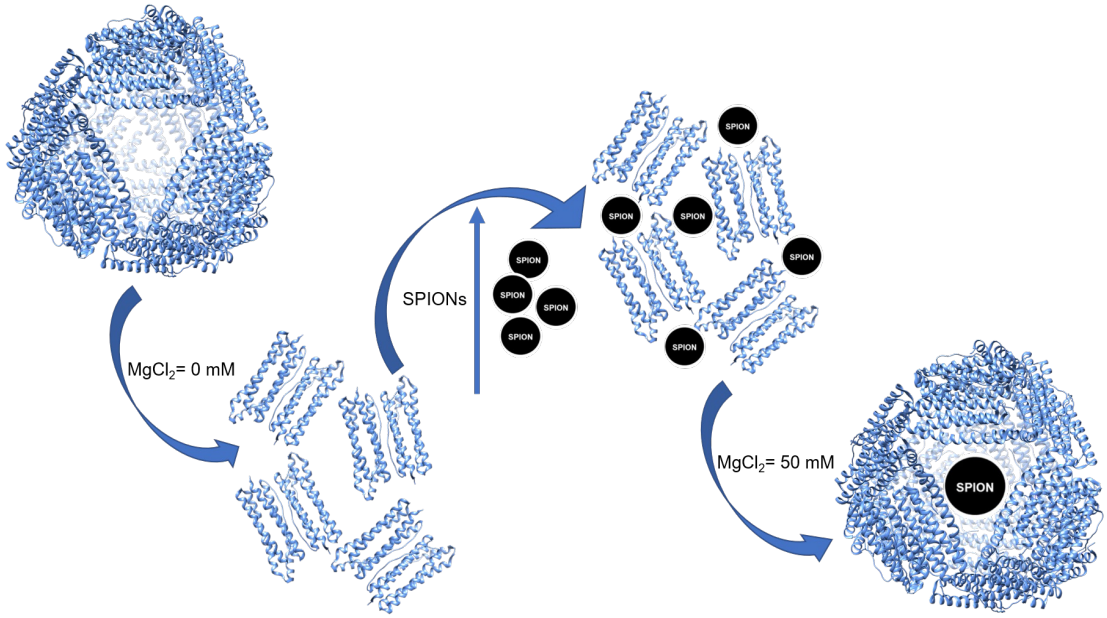

Figure 5.1 Schematic representation of the encapsulation process of the SPIONs. The disassembled HumAfFt was incubated in the presence of the SPIONs and the concentration of $MgCl_2$ was increased to 50 mM.

Circular Dichroism

CD spectroscopy was used to characterize the secondary structure of the HumAfFt in the absence and presence of SPIONs. The spectrum of the native protein is typical of a well-defined protein structure with mostly α-helical content, with two negative peaks at 208 nm and 222 nm as shown in Figure 5.2 (Incocciati et al., 2023; Miles et al., 2021; Vetri et al., 2011; Zhao et al., 2015; Zou et al., 2016). The results were analyzed and compared with the HumAfFt data from PDB (Figure 5.3). The composition of the HumAfFt comprises of 67.8% α-helix, 0% β-sheet, 5.7% β-turns, and 26.5% random coil.

Upon the exposure to SPIONs, there is a decrease of the total intensity, proportional to the increase of SPIONs concentration, that confirms the interaction between HumAfFt and

SPIONs; but the structural shape of the HumAfFt is still α-helical, therefore it did not undergo a conformational change.

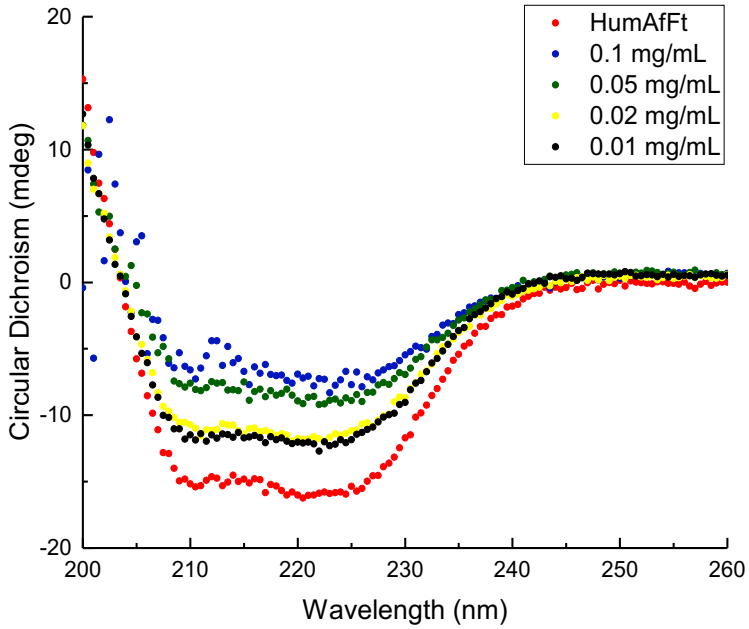

Figure 5.2 Circular Dichroism curves for HumAfFt (0.1 mg/mL) and HumAfFt-SPIONs at different concentrations of SPIONs (0.1 mg/mL; 0.05 mg/mL; 0.02 mg/mL; 0.01 mg/mL).

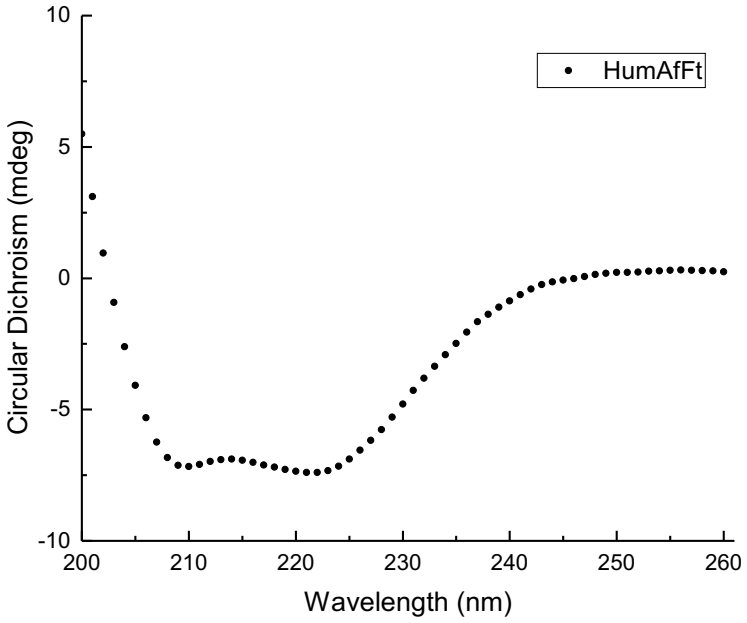

Figure 5.3 Circular Dichroism curve for HumAfFt from PDB.

As a confirmation of the stability of the analyzed samples in the time scale of the CD experiments, absorbance and fluorescence measurements of the samples were performed every five minutes for one hour. I reported in Figure 5.4 and Figure 5.5 the absorption and emission spectra of one sample of HumAfFt-SPIONs as an example. In particular, the absorption at 280 nm and 600 nm was the same for one hour. Furthermore, variations in the emission spectra during these measurements, were not observed. These results indicate that the sample is stable during the CD measurements and there is not sedimentation.

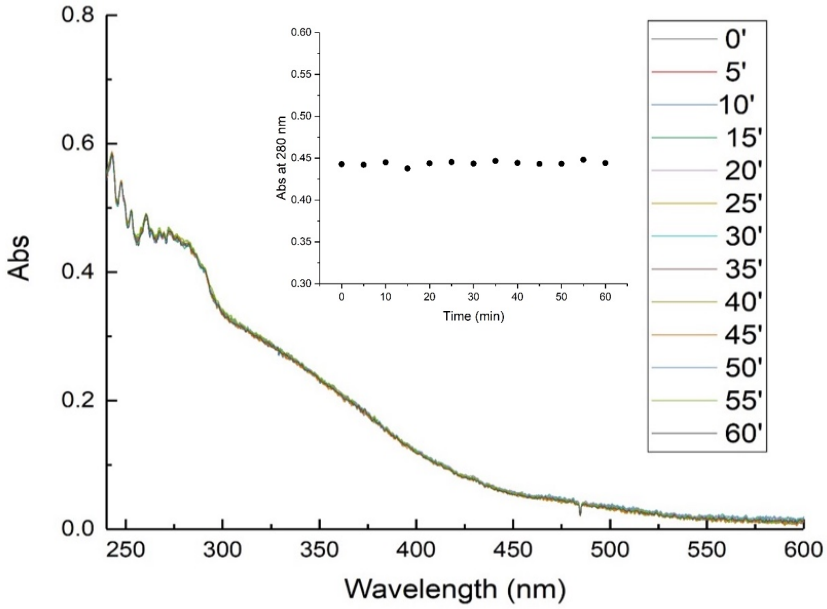

Figure 5.4 Absorption spectra of HumAfFt-SPIONs at different times (every five minutes for one hour). [HumAfFt]= 0.1 mg/mL; [SPIONs]= 0.01 mg/mL. The inset shows the absorption at 280 nm.

A

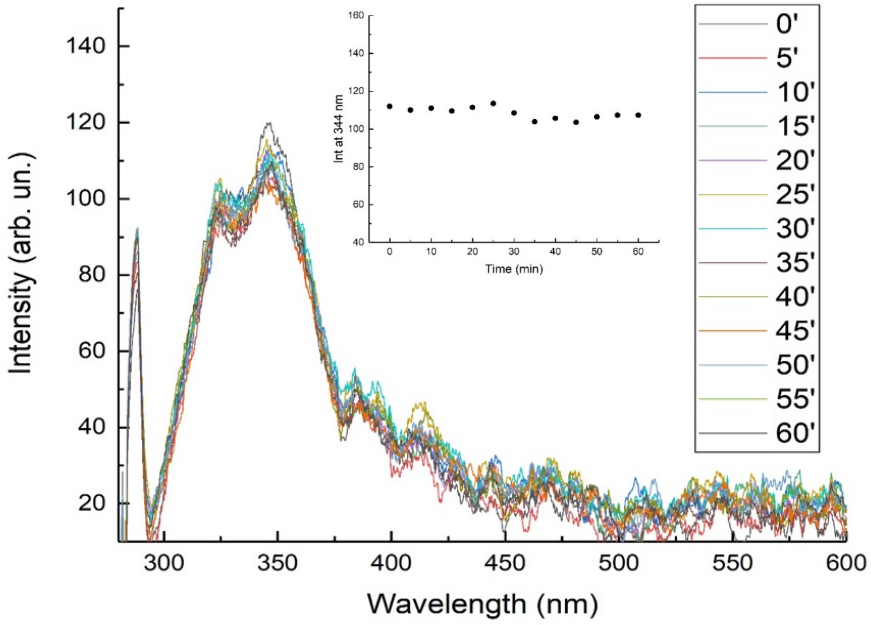

B

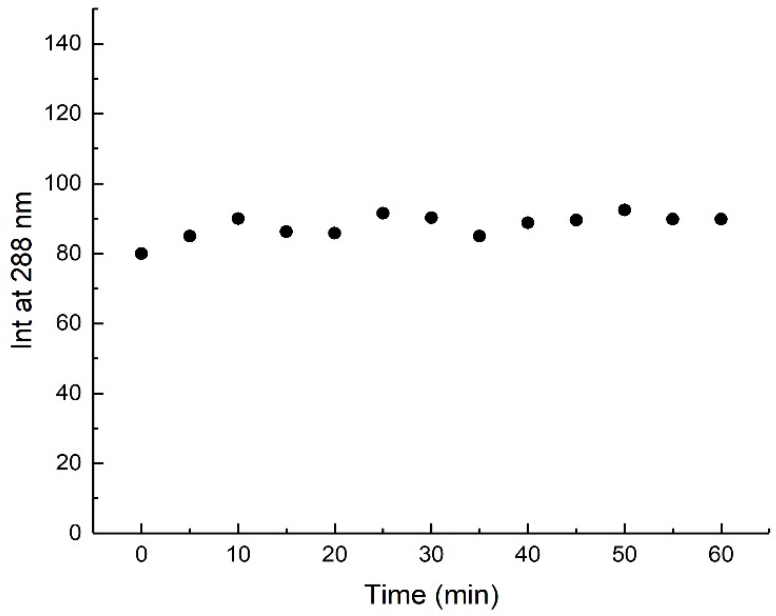

Figure 5.5 (A) Emission spectra of HumAfFt-SPIONs at different times (every five minutes for one hour). [HumAfFt]= 0.1 mg/mL; [SPIONs]= 0.01 mg/mL. The inset shows the emission at 344 nm. (B) Emission of the same sample at 288 nm.

EPR

Magnetic properties of HumAfFt-SPIONs and uncoated SPIONs were investigated by electron paramagnetic resonance (EPR) technique. Figure 5.6 shows the room temperature EPR signals for SPIONs and freeze-dried HumAfFt-SPIONs samples.

EPR Spectrum of HumAfFt-SPIONs sample was normalized to the mass of SPIONs sample. At room temperature, a very broad and strong single asymmetric microwave resonance signal is observed in EPR spectra at a field of around 2600 G, linewidths of ≅300 G and g-values of 2.7 for SPIONs. The resonance field and the linewidth of EPR signal depend on the coating material (Köseoğlu, 2006); both the resonance field and the linewidth increase due to coating: resonance field of around 2800 G, linewidths of ≅548 G and g-values of 2.4 for HumAfFt-SPIONs. The total effective magnetic moment of the SPIONs decreases due to coating, which is due to a non-collinear spin structure originated from the pinning of the surface spins and coated ferritin at the interface of nanoparticles.

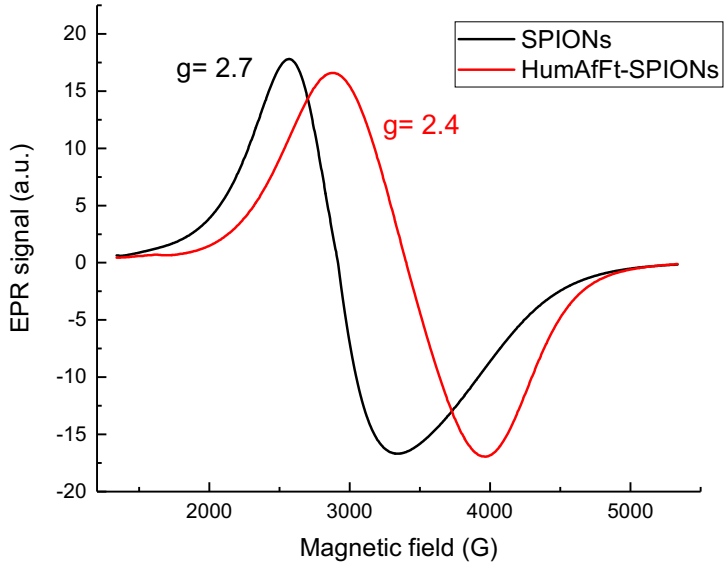

Figure 5.6 Room temperature EPR signals for SPIONs and HumAfFt-SPIONs samples.

Magnetization

Furthermore, to investigate the effect of encapsulation on the magnetic properties of the SPIONs, zero field cooled (ZFC) and field cooled (FC) magnetization curves were performed on dry samples of SPIONs and HumAfFt-SPIONs (Licciardi et al., 2013). In the whole temperature interval investigated, the FC and ZFC magnetization curves increase upon lowering the temperature. In the low temperature part of the magnetization, the ZFC and FC curves of each system do not overlap, indicating some magnetic blocking of the magnetic particles. In both systems, the ZFC and FC magnetization curves start to overlap around 70 K, indicating the transition to a superparamagnetic regime above this temperature. Upon examination of the ZFC and FC magnetization curves in Figure 5.7A, it was discovered that the magnetization curves of the HumAfFt-SPIONs demonstrated greater magnetization values at all evaluated temperatures. We attribute this difference to the samples not being completely dry. In order to better compare the behaviour of SPIONs and that of HumAfFt-SPIONs, I chose to normalize the data (Figure 5.7B). The normalized magnetization curves are fully superimposable showing that the magnetic properties of the SPIONs remain unchanged upon encapsulation in HumAfFt.

A

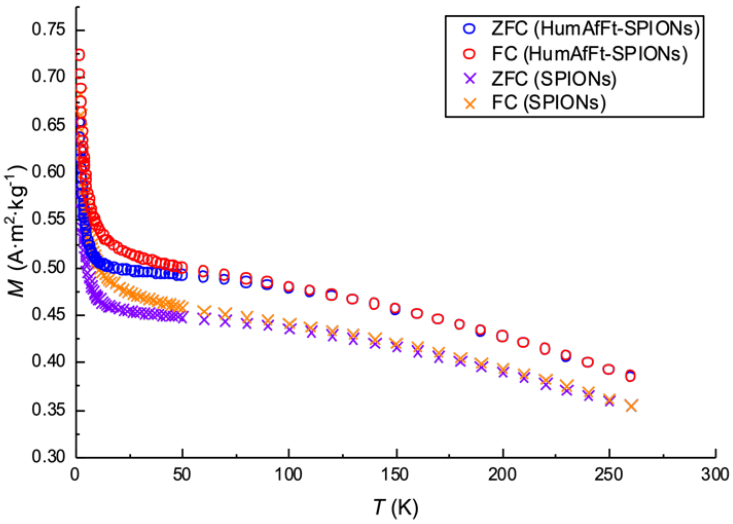

B

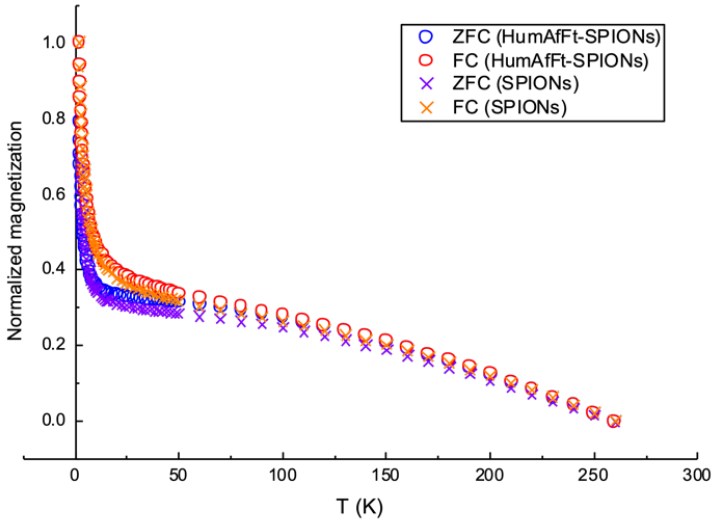

Figure 5.7 (A) ZFC and FC magnetization curves for SPIONs and HumAfFt-SPIONs. (B) Normalized ZFC and FC magnetization curves for SPIONs and HumAfFt-SPIONs.

MRI

The ability of HumAfFt-SPIONs to act as contrast for MRI was evaluated by recording T_2-weighted MRI images of nanoparticle dispersion (Sharifi et al., 2015; Wierzbinski et al., 2018; Zhang et al., 2016). I compared it with HumAfFt and the results show that the new HumAfFt-SPIONs act as a contrast agent improving resolution in T_2-weighted images (Figure 5.8). These images demonstrate the accumulation of magnetic nanoparticles by the presence of local dark spots due to high concentration of nanoparticles.

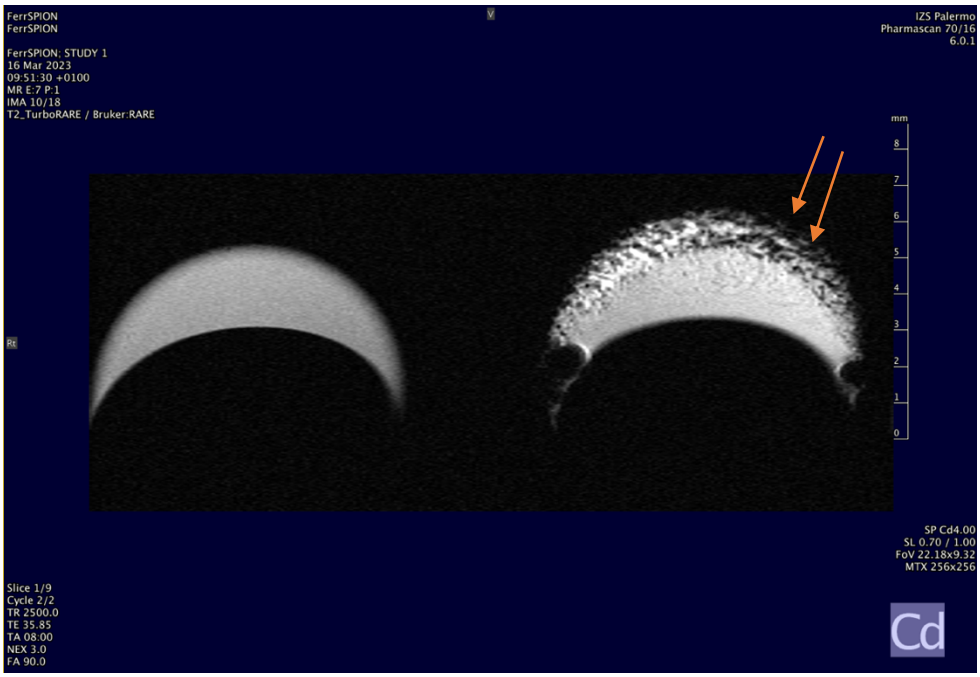

Figure 5.8 T_2-weighted images of HumAfFt (left) and HumAfFt-SPIONs (right) in aqueous dispersion. Arrows show representative zones for dark spots indicating nanoparticles accumulation.

5.4 Conclusions

I illustrated the properties of a novel superparamagnetic iron oxide nanoparticle, that can act as a contrast agent for site targeted cancer cells. In detail, I used the HumAfFt as a coating material for SPIONs to create a target-specific contrast agent. Previous results showed the stability and biocompatibility of the new complex HumAfFt-SPIONs and now I reported the structural characterization and the first analysis of it as an efficient contrast agent in conventional MRI. HumAfFt is an engineered ferritin characterized by the peculiar salt-triggered assembly-disassembly of the hyperthermophile *Archaeoglobus fulgidus* ferritin and which is successfully endowed with the human H homopolymer recognition sequence by the transferrin receptor, overexpressed in many cancer cells in response to the increased demand of iron. Using its 24-mer typical structure and the salt-triggered assembly mechanism, the HumAfFt successfully coated SPIONs. Its secondary structure is not altered upon the exposure to SPIONs and the new HumAfFt-SPIONs showed excellent magnetic properties. The MRI results demonstrated the ability of HumAfFt-SPIONs to act as an efficient contrast agent and encourage to evaluate their application *in vivo*.

6. Conclusions and perspectives

With this PhD thesis, I would like to highlight the versatility and the potentiality of the engineered ferritins. Two new engineered ferritin-based nanovectors were developed and characterized with different biophysical, biological and biochemical techniques. In particular, the HFt-LBT has been designed to produce a unique luminescent nanovector with potential applications in the diagnostic field. It contains the ligand to bind the CD71 receptor overexpressed in most cancer cells and it has been equipped with a specific metal binding tag, able to act as an antenna system for Europium. The nanotool thus acts both as a carrier targeted to tumour cells and as a LRET sensitizer. Among lanthanides, the chemical elements defined as "rare-earth metals", Europium is particularly suitable for bioimaging analysis because its red emission allows to reduce overlap with tissue autofluorescence and to match the biological transparency window. For this reason, I studied the interaction between the HFt-LBT and Europium. As illustrated in chapter 3, I firstly employed physics techniques, such as steady state emission measurements and time-resolved emission spectroscopy, to investigate this interaction. The obtained results were very promising in view of the next steps, that include the *in vitro* and *in vivo* applications of the HFt-LBT Eu^{3+} as a luminescent nanovector than can discriminate cancer cells from normal cells.

For the first time, I used the second engineered ferritin, the HumAfFt, as a biomimetic coating for SPIONs in order to produce a new magnetic nanocarrier able to distinguish cancer and normal cells and maintain the potential theranostic properties of SPIONs. Along chapters 4 and 5, I showed the characterization and the first *in vitro* analyses of the new complex HumAfFt-SPIONs, from the expression and purification of HumAfFt until the applications of HumAfFt-SPIONs. HumAfFt is an engineered ferritin made up of the *Archaeoglobus fulgidus* ferritin, that was genetically modified both to retain the AfFt peculiar assembly/disassembly, that could lead to a completely reversible loading of a cargo, and to have the human H homopolymer recognition sequence by the transferrin receptor, overexpressed in many cancer cells in response to the increased demand of iron. For this reason, I decided to use the HumAfFt as a coating material for SPIONs. The versality of SPIONs is widely known, they are used as theranostic, multimodal and multifunctional devises for simultaneous drug delivery and imaging, biomolecular tracking and cellular labelling; but to make SPIONs stable and suitable for biomedical applications, it is important to disperse the nanoparticles in water and modify their surface with small molecular

surfactants or polymers. The new complex HumAfFt-SPIONs was characterized in terms of size, morphology, composition and cytotoxicity. I illustrated the magnetic properties of HumAfFt-SPIONs and their ability to act as an efficient contrast agent in MRI. The *in vitro* analysis confirmed the preferential uptake of cancer cells toward the complex. Therefore, I managed to design a new theranostic nanovector ready to be tested *in vivo.*

7. Bibliography

Abdel-Mageed, H. M., AbuelEzz, N. Z., Radwan, R. A., & Mohamed, S. A. (2021). Nanoparticles in nanomedicine: a comprehensive updated review on current status, challenges and emerging opportunities. In *Journal of Microencapsulation* (Vol. 38, Issue 6, pp. 414–436). https://doi.org/10.1080/02652048.2021.1942275

Abuelezz, N. Z., Shabana, M. E., Abdel-Mageed, H. M., Rashed, L., & Morcos, G. N. B. (2020). Nanocurcumin alleviates insulin resistance and pancreatic deficits in polycystic ovary syndrome rats: Insights on PI3K/AkT/mTOR and TNF-α modulations. *Life Sciences*, *256*. https://doi.org/10.1016/j.lfs.2020.118003

Affatigato, L., Licciardi, M., Bonamore, A., Martorana, A., Incocciati, A., Boffi, A., & Militello, V. (2023). Ferritin-Coated SPIONs as New Cancer Cell Targeted Magnetic Nanocarrier. *Molecules*, *28*(3), 1163. https://doi.org/10.3390/molecules28031163

Affatigato, L., Sciortino, A., Sancataldo, G., Incocciati, A., Piacentini, R., Bonamore, A., Cannas, M., Messina, F., Licciardi, M., & Militello, V. (2023). Engineered Ferritin with Eu^{3+} as a Bright Nanovector: A Photoluminescence Study. *Photochemistry and Photobiology*, 99, 1218-1224. https://doi.org/10.1111/php.13759

Arbab, A. S., Bashaw, L. A., Miller, B. R., Jordan, E. K., Lewis, B. K., Kalish, H., & Frank, J. A. (2003). Characterization of Biophysical and Metabolic Properties of Cells Labeled with Superparamagnetic Iron Oxide Nanoparticles and Transfection Agent for Cellular MR Imaging. *Radiology*, *229*(3), 838–846. https://doi.org/10.1148/radiol.2293021215

Argenziano, M., Arpicco, S., Brusa, P., Cavalli, R., Chirio, D., Dosio, F., Gallarate, M., Peira, E., Stella, B., & Ugazio, E. (2021). Developing actively targeted nanoparticles to fight cancer: Focus on italian research. In *Pharmaceutics* (Vol. 13, Issue 10). MDPI. https://doi.org/10.3390/pharmaceutics13101538

Aulsebrook, M. L., Graham, B., Grace, M. R., & Tuck, K. L. (2018). Lanthanide complexes for luminescence-based sensing of low molecular weight analytes. In *Coordination Chemistry Reviews* (Vol. 375, pp. 191–220). Elsevier B.V. https://doi.org/10.1016/j.ccr.2017.11.018

Babincová M, Babinec P & Bergemann C. (2001) High-gradient magnetic capture of ferrofluids: implications for drug targeting and tumor embolization. *Z Naturforsch C J Biosci.* 2001 Sep-Oct;56(9-10):909-11. https://10.1515/znc-2001-9-1039.

Bain, J., & Staniland, S. S. (2015). Bioinspired nanoreactors for the biomineralisation of metallic-based nanoparticles for nanomedicine. In *Physical Chemistry Chemical Physics* (Vol. 17, Issue 24, pp. 15508–15521). Royal Society of Chemistry. https://doi.org/10.1039/c5cp00375j

Bao, G. (2020). Lanthanide complexes for drug delivery and therapeutics. In *Journal of Luminescence* (Vol. 228). Elsevier B.V. https://doi.org/10.1016/j.jlumin.2020.117622

Barb, A. W., Ho, T. G., Flanagan-Steet, H., & Prestegard, J. H. (2012). Lanthanide binding and IgG affinity construct: Potential applications in solution NMR, MRI, and luminescence microscopy. *Protein Science*, *21*(10), 1456–1466. https://doi.org/10.1002/pro.2133

Bedanta, S., & Kleemann, W. (2009). Supermagnetism. *Journal of Physics D: Applied Physics*, *42*(1). https://doi.org/10.1088/0022-3727/42/1/013001

Berry, C. C., & Curtis, A. S. G. (2003). Functionalisation of magnetic nanoparticles for applications in biomedicine. In *J. Phys. D: Appl. Phys* (Vol. 36). https://doi.org/10.1088/0022-3727/36/13/203

Binnemans, K. (2015). Interpretation of europium(III) spectra. In *Coordination Chemistry Reviews* (Vol. 295, pp. 1–45). Elsevier B.V. https://doi.org/10.1016/j.ccr.2015.02.015

Blanco, E., Shen, H., & Ferrari, M. (2015). Principles of nanoparticle design for overcoming biological barriers to drug delivery. In *Nature Biotechnology* (Vol. 33, Issue 9, pp. 941–951). Nature Publishing Group. https://doi.org/10.1038/nbt.3330

Bogdan, A. R., Miyazawa, M., Hashimoto, K., & Tsuji, Y. (2016). Regulators of Iron Homeostasis: New Players in Metabolism, Cell Death, and Disease. In *Trends in Biochemical Sciences* (Vol. 41, Issue 3, pp. 274–286). Elsevier Ltd. https://doi.org/10.1016/j.tibs.2015.11.012

Bonifácio, B. V., da Silva, P. B., Aparecido dos Santos Ramos, M., Maria Silveira Negri, K., Maria Bauab, T., & Chorilli, M. (2013). Nanotechnology-based drug delivery systems and herbal medicines: A review. In *International Journal of Nanomedicine* (Vol. 9, Issue 1, pp. 1–15). https://doi.org/10.2147/IJN.S52634

Bonnemain, B. (1998). Superparamagnetic Agents in Magnetic Resonance Imaging: Physicochemical Characteristics and Clinical Applications A Review. In *Journal of Drug Targeting* (Vol. 6, Issue 3). doi: 10.3109/10611869808997890.

Bou-Abdallah, F. (2010). The iron redox and hydrolysis chemistry of the ferritins. In *Biochimica et Biophysica Acta - General Subjects* (Vol. 1800, Issue 8, pp. 719–731). https://doi.org/10.1016/j.bbagen.2010.03.021

Bou-Abdallah, F., Arosio, P., Levi, S., Janus-Chandler, C., & Chasteen, N. D. (2003). Defining metal ion inhibitor interactions with recombinant human H- and L-chain ferritins and site-directed variants: An isothermal titration calorimetry study. *Journal of Biological Inorganic Chemistry*, *8*(4), 489–497. https://doi.org/10.1007/s00775-003-0455-6

Bünzli, J. C. G. (2006). Benefiting from the unique properties of lanthanide ions. In *Accounts of Chemical Research* (Vol. 39, Issue 1, pp. 53–61). https://doi.org/10.1021/ar0400894

Bünzli, J. C. G., Chauvin, A. S., Kim, H. K., Deiters, E., & Eliseeva, S. V. (2010). Lanthanide luminescence efficiency in eight- and nine-coordinate complexes: Role of the radiative lifetime. In *Coordination Chemistry Reviews* (Vol. 254, Issues 21–22, pp. 2623–2633). https://doi.org/10.1016/j.ccr.2010.04.002

Bünzli, J.-C. G., & Eliseeva, S. V. (2010). Basics of Lanthanide Photophysics. In Lanthanide Luminescence. Springer Series on Fluorescence (Vol. 7, pp. 1–45). https://doi.org/10.1007/4243_2010_3

Byrne, J. D., Betancourt, T., & Brannon-Peppas, L. (2008). Active targeting schemes for nanoparticle systems in cancer therapeutics. In *Advanced Drug Delivery Reviews* (Vol. 60, Issue 15, pp. 1615–1626). https://doi.org/10.1016/j.addr.2008.08.005

Calisti, L., Benni, I., Cardoso Trabuco, M., Baiocco, P., Ruzicka, B., Boffi, A., Falvo, E., Malatesta, F., & Bonamore, A. (2017). Probing bulky ligand entry in engineered archaeal ferritins. *Biochimica et Biophysica Acta - General Subjects*, *1861*(2), 450–456. https://doi.org/10.1016/j.bbagen.2016.10.007

Calisti, L., Trabuco, M. C., Boffi, A., Testi, C., Montemiglio, L. C., des Georges, A., Benni, I., Ilari, A., Taciak, B., Białasek, M., Rygiel, T., Król, M., Baiocco, P., & Bonamore, A. (2018). Engineered ferritin for lanthanide binding. *PLoS ONE*, *13*(8). https://doi.org/10.1371/journal.pone.0201859

Cao, C., Wang, X., Cai, Y., Sun, L., Tian, L., Wu, H., He, X., Lei, H., Liu, W., Chen, G., Zhu, R., & Pan, Y. (2014). Targeted in vivo imaging of microscopic tumors with ferritin-based nanoprobes across biological barriers. *Advanced Materials*, *26*(16), 2566–2571. https://doi.org/10.1002/adma.201304544

Castellani, S., Orlando, C., Carbone, A., Di Gioia, S., & Conese, M. (2016). Magnetofection enhances lentiviral-mediated transduction of airway epithelial cells through extracellular and cellular barriers. *Genes*, *7*(11). https://doi.org/10.3390/genes7110103

Chan, K. T., Choi, M. Y., Lai, K. K. Y., Tan, W., Tung, L. N., Lam, H. O. Y. U., Tong, D. K. H., Lee, N. P., & Law, S. (2014). Overexpression of transferrin receptor CD71 and its

tumorigenic properties in esophageal squamous cell carcinoma. *Oncology Reports*, *31*(3), 1296–1304. https://doi.org/10.3892/or.2014.2981

Chandra, S., Das, P., Bag, S., Laha, D., & Pramanik, P. (2011). Synthesis, functionalization and bioimaging applications of highly fluorescent carbon nanoparticles. *Nanoscale*, *3*(4), 1533–1540. https://doi.org/10.1039/c0nr00735h

Chatterjee, J., Haik, Y., & Chen, C.-J. (2003). Size dependent magnetic properties of iron oxide nanoparticles. In *Journal of Magnetism and Magnetic Materials* (Vol. 257 pp. 113-118) https://doi.org/10.1016/S0304-8853(02)01066-1

Chen, H., Wang, L., Yu, Q., Qian, W., Tiwari, D., Yi, H., Wang, A. Y., Huang, J., Yang, L., & Mao, H. (2013). Anti-HER2 antibody and ScFvEGFR-conjugated antifouling magnetic iron oxide nanoparticles for targeting and magnetic resonance imaging of breast cancer. *International Journal of Nanomedicine*, *8*, 3781–3794. https://doi.org/10.2147/IJN.S49069

Cheng, F. Y., Wang, S. P. H., Su, C. H., Tsai, T. L., Wu, P. C., Shieh, D. Bin, Chen, J. H., Hsieh, P. C. H., & Yeh, C. S. (2008). Stabilizer-free poly(lactide-co-glycolide) nanoparticles for multimodal biomedical probes. *Biomaterials*, *29*(13), 2104–2112. https://doi.org/10.1016/j.biomaterials.2008.01.010

Chilkoti, A., Dreher, M. R., & Meyer, D. E. (2002). Design of thermally responsive, recombinant polypeptide carriers for targeted drug delivery. In *Advanced Drug Delivery Reviews* (Vol. 54 pp. 1093-111) doi: 10.1016/s0169-409x(02)00060-1

Cho, H. J. (2020). Recent progresses in the development of hyaluronic acid-based nanosystems for tumor-targeted drug delivery and cancer imaging. In *Journal of Pharmaceutical Investigation* (Vol. 50, Issue 2, pp. 115–129). Springer. https://doi.org/10.1007/s40005-019-00448-w

Choulyt, C., Pouliquen, D., Lucet, I., Jeune, J. J., & Jallet, P. (1996). Development of superparamagnetic nanoparticles for MRI: effect of particle size, charge and surface nature on biodistribution. In *Journal of Microencapsulation,* 13:3, 245-255, doi: 10.3109/02652049609026013

Cortajarena, A. L., Ortega, D., Ocampo, S. M., Gonzalez-García, A., Couleaud, P., Miranda, R., Belda-Iniesta, C., & Ayuso-Sacido, A. (2014). Engineering Iron Oxide Nanoparticles for Clinical Settings. *Nanobiomedicine*, *1*. https://doi.org/10.5772/58841

Crichton, R. R., & Bryce, C. F. A. (1973). Subunit Interactions in Horse Spleen Apoferritin dissociation by extremes of pH. In *Biochem. J*, 133(2):289-99. doi: 10.1042/bj1330289.

D'Amato, R., Falconieri, M., Gagliardi, S., Popovici, E., Serra, E., Terranova, G., & Borsella, E. (2013). Synthesis of ceramic nanoparticles by laser pyrolysis: From research to applications. *Journal of Analytical and Applied Pyrolysis*, *104*, 461–469. https://doi.org/10.1016/j.jaap.2013.05.026

Daniels, T. R., Bernabeu, E., Rodríguez, J. A., Patel, S., Kozman, M., Chiappetta, D. A., Holler, E., Ljubimova, J. Y., Helguera, G., & Penichet, M. L. (2012). The transferrin receptor and the targeted delivery of therapeutic agents against cancer. In *Biochimica et Biophysica Acta - General Subjects* (Vol. 1820, Issue 3, pp. 291–317). https://doi.org/10.1016/j.bbagen.2011.07.016

Daniels, T. R., Delgado, T., Helguera, G., & Penichet, M. L. (2006). The transferrin receptor part II: Targeted delivery of therapeutic agents into cancer cells. In *Clinical Immunology* (Vol. 121, Issue 2, pp. 159–176). https://doi.org/10.1016/j.clim.2006.06.006

Daniels, T. R., Delgado, T., Rodriguez, J. A., Helguera, G., & Penichet, M. L. (2006). The transferrin receptor part I: Biology and targeting with cytotoxic antibodies for the treatment of cancer. In *Clinical Immunology* (Vol. 121, Issue 2, pp. 144–158). https://doi.org/10.1016/j.clim.2006.06.010

Daniels-Wells, T. R., & Penichet, M. L. (2016). Transferrin receptor 1: A target for antibody-mediated cancer therapy. In *Immunotherapy* (Vol. 8, Issue 9, pp. 991–994). Future Medicine Ltd. https://doi.org/10.2217/imt-2016-0050

De Jong, W. H., & Borm, P. J. (2008). Drug delivery and nanoparticles: Applications and hazards. In *International Journal of Nanomedicine,* 3(2):133-49. doi: 10.2147/ijn.s596.

De Turris, V., Cardoso Trabuco, M., Peruzzi, G., Boffi, A., Testi, C., Vallone, B., Celeste Montemiglio, L., Georges, A. Des, Calisti, L., Benni, I., Bonamore, A., & Baiocco, P. (2017). Humanized archaeal ferritin as a tool for cell targeted delivery. *Nanoscale*, *9*(2), 647–655. https://doi.org/10.1039/c6nr07129e

Dickson, E. F. G., Pollak, A., & Diamandis, E. P. (1995). Time-resolved detection of lanthanide luminescence ultrasensitive bioanalytical assays for. In *Journal of Photochemistry and Photobioiogy B: Biology* (Vol. 27).

Din, F. U., Aman, W., Ullah, I., Qureshi, O. S., Mustapha, O., Shafique, S., & Zeb, A. (2017). Effective use of nanocarriers as drug delivery systems for the treatment of selected tumors. In *International Journal of Nanomedicine* (Vol. 12, pp. 7291–7309). Dove Medical Press Ltd. https://doi.org/10.2147/IJN.S146315

Duncan, R. (2006). Polymer conjugates as anticancer nanomedicines. In *Nature Reviews Cancer* (Vol. 6, Issue 9, pp. 688–701). https://doi.org/10.1038/nrc1958

Ealias, A. M., & Saravanakumar, M. P. (2017). A review on the classification, characterisation, synthesis of nanoparticles and their application. *IOP Conference Series: Materials Science and Engineering*, *263*(3). https://doi.org/10.1088/1757-899X/263/3/032019

Estelrich, J., Escribano, E., Queralt, J., & Busquets, M. A. (2015). Iron oxide nanoparticles for magnetically-guided and magnetically-responsive drug delivery. In *International Journal of Molecular Sciences* (Vol. 16, Issue 4, pp. 8070–8101). MDPI AG. https://doi.org/10.3390/ijms16048070

Falvo, E., Tremante, E., Arcovito, A., Papi, M., Elad, N., Boffi, A., Morea, V., Conti, G., Toffoli, G., Fracasso, G., Giacomini, P., & Ceci, P. (2016). Improved Doxorubicin Encapsulation and Pharmacokinetics of Ferritin-Fusion Protein Nanocarriers Bearing Proline, Serine, and Alanine Elements. *Biomacromolecules*, *17*(2), 514–522. https://doi.org/10.1021/acs.biomac.5b01446

Falvo, E., Tremante, E., Fraioli, R., Leonetti, C., Zamparelli, C., Boffi, A., Morea, V., Ceci, P., & Giacomini, P. (2013). Antibody-drug conjugates: Targeting melanoma with cisplatin encapsulated in protein-cage nanoparticles based on human ferritin. *Nanoscale*, *5*(24), 12278–12285. https://doi.org/10.1039/c3nr04268e

Fan, D., Cao, Y., Cao, M., Wang, Y., Cao, Y., & Gong, T. (2023). Nanomedicine in cancer therapy. In *Signal Transduction and Targeted Therapy* (Vol. 8, Issue 1). Springer Nature. https://doi.org/10.1038/s41392-023-01536-y

Fan, K., Cao, C., Pan, Y., Lu, D., Yang, D., Feng, J., Song, L., Liang, M., & Yan, X. (2012). Magnetoferritin nanoparticles for targeting and visualizing tumour tissues. *Nature Nanotechnology*, *7*(7), 459–464. https://doi.org/10.1038/nnano.2012.90

Ferrari, M. (2005). Cancer nanotechnology: Opportunities and challenges. In *Nature Reviews Cancer* (Vol. 5, Issue 3, pp. 161–171). https://doi.org/10.1038/nrc1566

Fracasso, G., Falvo, E., Colotti, G., Fazi, F., Ingegnere, T., Amalfitano, A., Doglietto, G. B., Alfieri, S., Boffi, A., Morea, V., Conti, G., Tremante, E., Giacomini, P., Arcovito, A., & Ceci, P. (2016). Selective delivery of doxorubicin by novel stimuli-sensitive nano-ferritins overcomes tumor refractoriness. *Journal of Controlled Release*, *239*, 10–18. https://doi.org/10.1016/j.jconrel.2016.08.010

Gao, Z. G., Fain, H. D., & Rapoport, N. (2005). Controlled and targeted tumor chemotherapy by micellar-encapsulated drug and ultrasound. *Journal of Controlled Release*, *102*(1), 203–222. https://doi.org/10.1016/j.jconrel.2004.09.021

Gavas, S., Quazi, S., & Karpiński, T. M. (2021). Nanoparticles for Cancer Therapy: Current Progress and Challenges. In *Nanoscale Research Letters* (Vol. 16, Issue 1). Springer. https://doi.org/10.1186/s11671-021-03628-6

Goda, N., Tenno, T., Inomata, K., Iwaya, N., Sasaki, Y., Shirakawa, M., & Hiroaki, H. (2007). LBT/PTD dual tagged vector for purification, cellular protein delivery and visualization in living cells. *Biochimica et Biophysica Acta - Molecular Cell Research*, *1773*(2), 141–146. https://doi.org/10.1016/j.bbamcr.2006.11.016

Gómez-Lopera, S. A., Plaza, R. C., & Delgado, A. V. (2001). Synthesis and characterization of spherical magnetite/biodegradable polymer composite particles. *Journal of Colloid and Interface Science*, *240*(1), 40–47. https://doi.org/10.1006/jcis.2001.7579

Gujrati, M., Malamas, A., Shin, T., Jin, E., Sun, Y., & Lu, Z. R. (2014). Multifunctional cationic lipid-based nanoparticles facilitate endosomal escape and reduction-triggered cytosolic siRNA release. *Molecular Pharmaceutics*, *11*(8), 2734–2744. https://doi.org/10.1021/mp400787s

Gullotti, E., & Yeo, Y. (2009). Extracellularly activated nanocarriers: A new paradigm of tumor targeted drug delivery. In *Molecular Pharmaceutics* (Vol. 6, Issue 4, pp. 1041–1051). https://doi.org/10.1021/mp900090z

Guo, M., Que, C., Wang, C., Liu, X., Yan, H., & Liu, K. (2011). Multifunctional superparamagnetic nanocarriers with folate-mediated and pH-responsive targeting properties for anticancer drug delivery. *Biomaterials*, *32*(1), 185–194. https://doi.org/10.1016/j.biomaterials.2010.09.077

Gupta, A. K., Berry, C., Gupta, M., & Curtis, A. (2003). Receptor-mediated targeting of magnetic nanoparticles using insulin as a surface ligand to prevent endocytosis. *IEEE Transactions on Nanobioscience*, *2*(4), 255–261. https://doi.org/10.1109/TNB.2003.820279

Gupta, A. K., & Curtis, A. S. G. (2004). *Surface modified superparamagnetic nanoparticles for drug delivery: Interaction studies with human fibroblasts in culture. Journal of Materials Science: Materials in Medicine, 15, 493–496. https://doi.org/10.1023/B:JMSM.0000021126.32934.20*

Gupta, A. K., & Gupta, M. (2005). Synthesis and surface engineering of iron oxide nanoparticles for biomedical applications. In *Biomaterials* (Vol. 26, Issue 18, pp. 3995–4021). https://doi.org/10.1016/j.biomaterials.2004.10.012

Gupta, A. K., Naregalkar, R. R., Vaidya, V. D., & Gupta, M. (2007). Recent advances on surface engineering of magnetic iron oxide nanoparticles and their biomedical

applications. In *Nanomedicine* (Vol. 2, Issue 1, pp. 23–39). https://doi.org/10.2217/17435889.2.1.23

Gupta, A. K., & Wells, S. (2004). Surface-Modified Superparamagnetic Nanoparticles for Drug Delivery: Preparation, Characterization, and Cytotoxicity Studies. *IEEE Transactions on Nanobioscience*, *3*(1), 66–73. https://doi.org/10.1109/TNB.2003.820277

Haley, B., & Frenkel, E. (2008). Nanoparticles for drug delivery in cancer treatment. In *Urologic Oncology: Seminars and Original Investigations* (Vol. 26, Issue 1, pp. 57–64). https://doi.org/10.1016/j.urolonc.2007.03.015

Han, D. H., Wang, J. P., & Luo, H. L. (1994). Crystallite size effect on saturation magnetization of fine ferrimagnetic particles. In *Journal of Magnetism and Magnetic Materials* (Vol. 136, Issue 1-2, pp. 176-182). https://doi.org/10.1016/0304-8853(94)90462-6.

Handgretinger, R., Lang, P., Schumm, M., Taylor, G., Neu, S., Koscielnak, E., Niethammer, D., & Klingebiel, T. (1998). Isolation and transplantation of autologous peripheral CD34 progenitor cells highly purified by magnetic-activated cell sorting. In *Bone Marrow Transplantation* (Vol. 21, pp. 987-93) doi: 10.1038/sj.bmt.1701228.

Handl, H. L., & Gillies, R. J. (2005). Lanthanide-based luminescent assays for ligand-receptor interactions. In *Life Sciences* (Vol. 77, Issue 4, pp. 361–371). Elsevier Inc. https://doi.org/10.1016/j.lfs.2005.01.009

Hayashi, K., Nakamura, M., Sakamoto, W., Yogo, T., Miki, H., Ozaki, S., Abe, M., Matsumoto, T., & Ishimura, K. (2013). Superparamagnetic nanoparticle clusters for cancer theranostics combining magnetic resonance imaging and hyperthermia treatment. *Theranostics*, *3*(6), 366–376. https://doi.org/10.7150/thno.5860

Heath, V. L., & Bicknell, R. (2009). Anticancer strategies involving the vasculature. In *Nature Reviews Clinical Oncology* (Vol. 6, Issue 7, pp. 395–404). https://doi.org/10.1038/nrclinonc.2009.52

Heffern, M. C., Matosziuk, L. M., & Meade, T. J. (2014). Lanthanide probes for bioresponsive imaging. In *Chemical Reviews* (Vol. 114, Issue 8, pp. 4496–4539). American Chemical Society. https://doi.org/10.1021/cr400477t

Hemmilä, I., & Laitala, V. (2005). Progress in lanthanides as luminescent probes. *Journal of Fluorescence*, *15*(4), 529–542. https://doi.org/10.1007/s10895-005-2826-6

Hempstead, P. D., Yewdall, S. J., Fernie, A. R., Lawson, D. M., Artymiuk, P. J., Rice, D. W., Ford, G. C., & Harrison, P. M. (1997). *Comparison of the Three-dimensional Structures*

of Recombinant Human H and Horse L Ferritins at High Resolution (Vol. 268, pp. 424-48) doi: 10.1006/jmbi.1997.0970.

Hoffman, J. B., Choi, H., & Kamat, P. V. (2014). Size-dependent energy transfer pathways in CdSe quantum dot-squaraine light-harvesting assemblies: Förster versus dexter. *Journal of Physical Chemistry C*, *118*(32), 18453–18461. https://doi.org/10.1021/jp506757a

Hola, K., Markova, Z., Zoppellaro, G., Tucek, J., & Zboril, R. (2015). Tailored functionalization of iron oxide nanoparticles for MRI, drug delivery, magnetic separation and immobilization of biosubstances. In *Biotechnology Advances* (Vol. 33, Issue 6, pp. 1162–1176). Elsevier Inc. https://doi.org/10.1016/j.biotechadv.2015.02.003

Holden, J. F., & Adams, M. W. W. (2003). Microbe-metal interactions in marine hydrothermal environments. In *Current Opinion in Chemical Biology* (Vol. 7, Issue 2, pp. 160–165). Elsevier Ltd. https://doi.org/10.1016/S1367-5931(03)00026-7

Honarmand Ebrahimi, K., Bill, E., Hagedoorn, P. L., & Hagen, W. R. (2012). The catalytic center of ferritin regulates iron storage via Fe(II)-Fe(III) displacement. *Nature Chemical Biology*, *8*(11), 941–948. https://doi.org/10.1038/nchembio.1071

Honarmand Ebrahimi, K., Hagedoorn, P. L., & Hagen, W. R. (2015). Unity in the biochemistry of the iron-storage proteins ferritin and bacterioferritin. In *Chemical Reviews* (Vol. 115, Issue 1, pp. 295–326). American Chemical Society. https://doi.org/10.1021/cr5004908

Hong, R. Y., Feng, B., Chen, L. L., Liu, G. H., Li, H. Z., Zheng, Y., & Wei, D. G. (2008). Synthesis, characterization and MRI application of dextran-coated Fe_3O_4 magnetic nanoparticles. *Biochemical Engineering Journal*, *42*(3), 290–300. https://doi.org/10.1016/j.bej.2008.07.009

Hong, R. Y., Li, J. H., Qu, J. M., Chen, L. L., & Li, H. Z. (2009). Preparation and characterization of magnetite/dextran nanocomposite used as a precursor of magnetic fluid. *Chemical Engineering Journal*, *150*(2–3), 572–580. https://doi.org/10.1016/j.cej.2009.03.034

Hopkins, C. R., & Trowbridge, I. S. (1983). *Internalization and Processing of Transferrin and the Transferrin Receptor in Human Carcinoma A431 Cells*. In *J Cell Biol.* (Vol. 2, pp. 508-21) doi: 10.1083/jcb.97.2.508.

Huang, X., Chisholm, J., Zhuang, J., Xiao, Y., Duncan, G., Chen, X., Suk, J. S., & Hanes, J. (2017). Protein nanocages that penetrate airway mucus and tumor tissue. *Proceedings*

of the National Academy of Sciences of the United States of America, *114*(32), E6595–E6602. https://doi.org/10.1073/pnas.1705407114

Huang, Y. J., Ke, C., Fu, L. M., Li, Y., Wang, S. F., Ma, Y. C., Zhang, J. P., & Wang, Y. (2019). Excitation Energy-Transfer Processes in the Sensitization Luminescence of Europium in a Highly Luminescent Complex. *ChemistryOpen*, *8*(3), 388–392. https://doi.org/10.1002/open.201900012

Incocciati, A., Bertuccini, L., Boffi, A., Macone, A., & Bonamore, A. (2022). Unlocking the Treasure Box: The Role of HEPES Buffer in Disassembling an Uncommon Ferritin Nanoparticle. *Separations*, *9*(8). https://doi.org/10.3390/separations9080222

Incocciati, A., Kubeš, J., Piacentini, R., Cappelletti, C., Botta, S., Bertuccini, L., Šimůnek, T., Boffi, A., Macone, A., & Bonamore, A. (2023). Hydrophobicity-enhanced ferritin nanoparticles for efficient encapsulation and targeted delivery of hydrophobic drugs to tumor cells. *Protein Science*, *32*(12). https://doi.org/10.1002/pro.4819

Johnson, E., Cascio, D., Sawaya, M. R., Gingery, M., & Schröder, I. (2005). Crystal structures of a tetrahedral open pore ferritin from the hyperthermophilic Archaeon Archaeoglobus fulgidus. *Structure*, *13*(4), 637–648. https://doi.org/10.1016/j.str.2005.01.019

Johnson, L., Pinder, S. E., & Douek, M. (2013). Deposition of superparamagnetic iron-oxide nanoparticles in axillary sentinel lymph nodes following subcutaneous injection. *Histopathology*, *62*(3), 481–486. https://doi.org/10.1111/his.12019

Joudeh, N., & Linke, D. (2022). Nanoparticle classification, physicochemical properties, characterization, and applications: a comprehensive review for biologists. In *Journal of Nanobiotechnology* (Vol. 20, Issue 1). BioMed Central Ltd. https://doi.org/10.1186/s12951-022-01477-8

Kanekiyo, M., Wei, C. J., Yassine, H. M., McTamney, P. M., Boyington, J. C., Whittle, J. R. R., Rao, S. S., Kong, W. P., Wang, L., & Nabel, G. J. (2013). Self-assembling influenza nanoparticle vaccines elicit broadly neutralizing H1N1 antibodies. *Nature*, *499*(7456), 102–106. https://doi.org/10.1038/nature12202

Khan, I., Saeed, K., & Khan, I. (2019). Nanoparticles: Properties, applications and toxicities. In *Arabian Journal of Chemistry* (Vol. 12, Issue 7, pp. 908–931). Elsevier B.V. https://doi.org/10.1016/j.arabjc.2017.05.011

Kido, J., & Okamoto, Y. (2002). Organo lanthanide metal complexes for electroluminescent materials. *Chemical Reviews*, *102*(6), 2357–2368. https://doi.org/10.1021/cr010448y

Kim, D. K., Mikhaylova, M., Wang, F. H., Kehr, J., Bjelke, B., Zhang, Y., Tsakalakos, T., & Muhammed, M. (2003). Starch-Coated Superparamagnetic Nanoparticles as MR Contrast Agents. *Chemistry of Materials*, *15*(23), 4343–4351. https://doi.org/10.1021/cm031104m

Kim, M., Rho, Y., Jin, K. S., Ahn, B., Jung, S., Kim, H., & Ree, M. (2011). PH-dependent structures of ferritin and apoferritin in solution: Disassembly and reassembly. *Biomacromolecules*, *12*(5), 1629–1640. https://doi.org/10.1021/bm200026v

Kim, S., Jeon, J. O., Jun, E., Jee, J. G., Jung, H. K., Lee, B. H., Kim, I. S., & Kim, S. (2016). Designing Peptide Bunches on Nanocage for Bispecific or Superaffinity Targeting. *Biomacromolecules*, *17*(3), 1150–1159. https://doi.org/10.1021/acs.biomac.5b01753

Köseoğlu, Y. (2006). Effect of surfactant coating on magnetic properties of Fe3O 4 nanoparticles: ESR study. *Journal of Magnetism and Magnetic Materials*, *300*(1). https://doi.org/10.1016/j.jmmm.2005.10.112

Kostiainen, M. A., Hiekkataipale, P., Laiho, A., Lemieux, V., Seitsonen, J., Ruokolainen, J., & Ceci, P. (2013). Electrostatic assembly of binary nanoparticle superlattices using protein cages. *Nature Nanotechnology*, *8*(1), 52–56. https://doi.org/10.1038/nnano.2012.220

Kumar, C. S. S. R., & Mohammad, F. (2011). Magnetic nanomaterials for hyperthermia-based therapy and controlled drug delivery. In *Advanced Drug Delivery Reviews* (Vol. 63, Issue 9, pp. 789–808). https://doi.org/10.1016/j.addr.2011.03.008

Lakowicz, J. R. (2006). *Principles of fluorescence spectroscopy*. Springer.

Laurent, S., Dutz, S., Häfeli, U. O., & Mahmoudi, M. (2011). Magnetic fluid hyperthermia: Focus on superparamagnetic iron oxide nanoparticles. In *Advances in Colloid and Interface Science* (Vol. 166, Issues 1–2, pp. 8–23). https://doi.org/10.1016/j.cis.2011.04.003

Laurent, S., Forge, D., Port, M., Roch, A., Robic, C., Vander Elst, L., & Muller, R. N. (2008). Magnetic iron oxide nanoparticles: Synthesis, stabilization, vectorization, physicochemical characterizations and biological applications. *Chemical Reviews*, *108*(6), 2064–2110. https://doi.org/10.1021/cr068445e

Laurent, S., Saei, A. A., Behzadi, S., Panahifar, A., & Mahmoudi, M. (2014). Superparamagnetic iron oxide nanoparticles for delivery of therapeutic agents: Opportunities and challenges. In *Expert Opinion on Drug Delivery* (Vol. 11, Issue 9, pp. 1449–1470). Informa Healthcare. https://doi.org/10.1517/17425247.2014.924501

LaVan, D. A., McGuire, T., & Langer, R. (2003). Small-scale systems for in vivo drug delivery. In *Nature Biotechnology* (Vol. 21, Issue 10, pp. 1184–1191). https://doi.org/10.1038/nbt876

Lefebure, S., Dubois, E., Cabuil, V., Neveu, S, & Massart, R. (2014). Monodisperse magnetic nanoparticles: Preparation and dispersion in water and oils. In *Journal of Materials Research,* 13(10):2975-2981 doi:10.1557/JMR.1998.0407

Lei, Y., Hamada, Y., Li, J., Cong, L., Wang, N., Li, Y., Zheng, W., & Jiang, X. (2016). Targeted tumor delivery and controlled release of neuronal drugs with ferritin nanoparticles to regulate pancreatic cancer progression. *Journal of Controlled Release*, *232*, 131–142. https://doi.org/10.1016/j.jconrel.2016.03.023

Levi, S., Luzzago, A., Cesareni, G., Cozzi, A., Franceschinelli, F., Albertini, A., & Arosio, P. (1988). Mechanism of ferritin iron uptake: Activity of the H-chain and deletion mapping of the ferro-oxidase site. A study of iron uptake and ferro-oxidase activity of human liver, recombinant H-chain ferritins, and of two H-chain deletion mutants. *Journal of Biological Chemistry*, *263*(34), 18086–18092. https://doi.org/10.1016/s0021-9258(19)81326-1

Levi, S., Luzzago, A., Franceschinelli, F., Santambrogio, P., Cesarenitl, G., & Arosio, P. (1989). Mutational analysis of the channel and loop sequences of human ferritin H-chain. In *Biochem. J* (Vol. 264, pp. 381-8) doi: 10.1042/bj2640381

Li, L., Fang, C. J., Ryan, J. C., Niemi, E. C., Lebrón, J. A., Björkman, P. J., Arase, H., Torti, F. M., Torti, S. V., Nakamura, M. C., & Seaman, W. E. (2010). Binding and uptake of H-ferritin are mediated by human transferrin receptor-1. *Proceedings of the National Academy of Sciences of the United States of America*, *107*(8), 3505–3510. https://doi.org/10.1073/pnas.0913192107

Li, Y., Xiong, P., Von Molnár, S., Wirth, S., Ohno, Y., & Ohno, H. (2002). Hall magnetometry on a single iron nanoparticle. *Applied Physics Letters*, *80*(24), 4644–4646. https://doi.org/10.1063/1.1487921

Licciardi, M., Scialabba, C., Cavallaro, G., Sangregorio, C., Fantechi, E., & Giammona, G. (2013). Cell uptake enhancement of folate targeted polymer coated magnetic nanoparticles. *Journal of Biomedical Nanotechnology*, *9*(6), 949–964. https://doi.org/10.1166/jbn.2013.1606

Licciardi, M., Scialabba, C., Puleio, R., Cassata, G., Cicero, L., Cavallaro, G., & Giammona, G. (2019). Smart copolymer coated SPIONs for colon cancer chemotherapy.

International Journal of Pharmaceutics, *556*, 57–67. https://doi.org/10.1016/j.ijpharm.2018.11.069

Licciardi, M., Varvarà, P., Tranchina, L., Puleio, R., Cicero, L., Cassata, G., & Giammona, G. (2022). In vivo efficacy of verteporfin loaded gold nanorods for combined photothermal/photodynamic colon cancer therapy. *International Journal of Pharmaceutics*, *625*. https://doi.org/10.1016/j.ijpharm.2022.122134

Lin, X., Xie, J., Niu, G., Zhang, F., Gao, H., Yang, M., Quan, Q., Aronova, M. A., Zhang, G., Lee, S., Leapman, R., & Chen, X. (2011). Chimeric ferritin nanocages for multiple function loading and multimodal imaging. *Nano Letters*, *11*(2), 814–819. https://doi.org/10.1021/nl104141g

Ling, D., Lee, N., & Hyeon, T. (2015). Chemical synthesis and assembly of uniformly sized iron oxide nanoparticles for medical applications. *Accounts of Chemical Research*, *48*(5), 1276–1285. https://doi.org/10.1021/acs.accounts.5b00038

Liu, M., Zhao, F., Zhu, D., Duan, H., Lv, Y., Li, L., & Gan, L. (2018). Ultramicroporous carbon nanoparticles derived from metal–organic framework nanoparticles for high-performance supercapacitors. *Materials Chemistry and Physics*, *211*, 234–241. https://doi.org/10.1016/j.matchemphys.2018.02.030

Long, C. M., Nascarella, M. A., & Valberg, P. A. (2013). Carbon black vs. black carbon and other airborne materials containing elemental carbon: Physical and chemical distinctions. In *Environmental Pollution* (Vol. 181, pp. 271–286). Elsevier Ltd. https://doi.org/10.1016/j.envpol.2013.06.009

Lu, H., Wang, J., Wang, T., Zhong, J., Bao, Y., & Hao, H. (2016). Recent Progress on Nanostructures for Drug Delivery Applications. In *Journal of Nanomaterials* (Vol. 2016). Hindawi Limited. https://doi.org/10.1155/2016/5762431

Lu, K. Q., Quan, Q., Zhang, N., & Xu, Y. J. (2016). Multifarious roles of carbon quantum dots in heterogeneous photocatalysis. In *Journal of Energy Chemistry* (Vol. 25, Issue 6, pp. 927–935). Elsevier B.V. https://doi.org/10.1016/j.jechem.2016.09.015

Lu, Y., Yin, Y., Mayers, B. T., & Xia, Y. (2002). Modifying the Surface Properties of Superparamagnetic Iron Oxide Nanoparticles through a Sol-Gel Approach. *Nano Letters*, *2*(3), 183–186. https://doi.org/10.1021/nl015681q

Ma, H. L., Xu, Y. F., Qi, X. R., Maitani, Y., & Nagai, T. (2008). Superparamagnetic iron oxide nanoparticles stabilized by alginate: Pharmacokinetics, tissue distribution, and applications in detecting liver cancers. *International Journal of Pharmaceutics*, *354*(1–2), 217–226. https://doi.org/10.1016/j.ijpharm.2007.11.036

Ma, H. li, Qi, X. rong, Maitani, Y., & Nagai, T. (2007). Preparation and characterization of superparamagnetic iron oxide nanoparticles stabilized by alginate. *International Journal of Pharmaceutics*, *333*(1–2), 177–186. https://doi.org/10.1016/j.ijpharm.2006.10.006

Macone, A., Masciarelli, S., Palombarini, F., Quaglio, D., Boffi, A., Trabuco, M. C., Baiocco, P., Fazi, F., & Bonamore, A. (2019). Ferritin nanovehicle for targeted delivery of cytochrome C to cancer cells. *Scientific Reports*, *9*(1). https://doi.org/10.1038/s41598-019-48037-z

Maeda, H, Wu, J., Sawa, T., Matsumura, Y., & Hori, K. (2000). Tumor vascular permeability and the EPR effect in macromolecular therapeutics: a review. In *Journal of Controlled Release* (Vol. 65, pp. 271-84) doi: 10.1016/s0168-3659(99)00248-5

Maeda, H., Bharate, G. Y., & Daruwalla, J. (2009). Polymeric drugs for efficient tumor-targeted drug delivery based on EPR-effect. In *European Journal of Pharmaceutics and Biopharmaceutics* (Vol. 71, Issue 3, pp. 409–419). https://doi.org/10.1016/j.ejpb.2008.11.010

Mah, C., Fraites, T. J., Zolotukhin, I., Song, S., Flotte, T. R., Dobson, J., Batich, C., & Byrne, B. J. (2002). Improved method of recombinant AAV2 delivery for systemic targeted gene therapy. *Molecular Therapy*, *6*(1), 106–112. https://doi.org/10.1006/mthe.2001.0636

Mahmoudi, M., Sant, S., Wang, B., Laurent, S., & Sen, T. (2011). Superparamagnetic iron oxide nanoparticles (SPIONs): Development, surface modification and applications in chemotherapy. In *Advanced Drug Delivery Reviews* (Vol. 63, Issues 1–2, pp. 24–46). https://doi.org/10.1016/j.addr.2010.05.006

Maity, B., Abe, S., & Ueno, T. (2017). Observation of gold sub-nanocluster nucleation within a crystalline protein cage. *Nature Communications*, *8*. https://doi.org/10.1038/ncomms14820

Malam, Y., Loizidou, M., & Seifalian, A. M. (2009). Liposomes and nanoparticles: nanosized vehicles for drug delivery in cancer. In *Trends in Pharmacological Sciences* (Vol. 30, Issue 11, pp. 592–599). https://doi.org/10.1016/j.tips.2009.08.004

Mallakpour, S., & Madani, M. (2015). A review of current coupling agents for modification of metal oxide nanoparticles. In *Progress in Organic Coatings* (Vol. 86, pp. 194–207). Elsevier B.V. https://doi.org/10.1016/j.porgcoat.2015.05.023

Mao, X., Xu, J., & Cui, H. (2016). Functional nanoparticles for magnetic resonance imaging. In *Wiley Interdisciplinary Reviews: Nanomedicine and Nanobiotechnology* (Vol. 8, Issue 6, pp. 814–841). Wiley-Blackwell. https://doi.org/10.1002/wnan.1400

Marcazzan, S., Varoni, E. M., Blanco, E., Lodi, G., & Ferrari, M. (2018). Nanomedicine, an emerging therapeutic strategy for oral cancer therapy. In *Oral Oncology* (Vol. 76, pp. 1–7). Elsevier Ltd. https://doi.org/10.1016/j.oraloncology.2017.11.014

Martin, L. J., Hähnke, M. J., Nitz, M., Wöhnert, J., Silvaggi, N. R., Allen, K. N., Schwalbe, H., & Imperiali, B. (2007). Double-lanthanide-binding tags: Design, photophysical properties, and NMR applications. *Journal of the American Chemical Society*, *129*(22), 7106–7113. https://doi.org/10.1021/ja070480v

Mauro, N., Scialabba, C., Puleio, R., Varvarà, P., Licciardi, M., Cavallaro, G., & Giammona, G. (2019). SPIONs embedded in polyamino acid nanogels to synergistically treat tumor microenvironment and breast cancer cells. *International Journal of Pharmaceutics*, *555*, 207–219. https://doi.org/10.1016/j.ijpharm.2018.11.046

Mauro, N., Utzeri, M. A., Varvarà, P., & Cavallaro, G. (2021). Functionalization of metal and carbon nanoparticles with potential in cancer theranostics. *Molecules*, *26*(11). https://doi.org/10.3390/molecules26113085

Mauter, M. S., & Elimelech, M. (2008). Environmental applications of carbon-based nanomaterials. In *Environmental Science and Technology* (Vol. 42, Issue 16, pp. 5843–5859). https://doi.org/10.1021/es8006904

Miles, A. J., Janes, R. W., & Wallace, B. A. (2021). Tools and methods for circular dichroism spectroscopy of proteins: A tutorial review. In *Chemical Society Reviews* (Vol. 50, Issue 15, pp. 8400–8413). Royal Society of Chemistry. https://doi.org/10.1039/d0cs00558d

Ming Qian, Z., & Sun, H. (2002). Targeted Drug Delivery via the Transferrin Receptor-Mediated Endocytosis Pathway. *In Pharmacol Rev.* (V. 4, pp. 561-87) doi: 10.1124/pr.54.4.561.

Miyazaki, S., Miyata, K., Sakamoto, H., Suzue, F., Kitagawa, Y., Hasegawa, Y., & Onda, K. (2020). Dual Energy Transfer Pathways from an Antenna Ligand to Lanthanide Ion in Trivalent Europium Complexes with Phosphine-Oxide Bridges. *Journal of Physical Chemistry A*, *124*(33), 6601–6606. https://doi.org/10.1021/acs.jpca.0c02224

Mody, V., Siwale, R., Singh, A., & Mody, H. (2010). Introduction to metallic nanoparticles. *Journal of Pharmacy And Bioallied Sciences*, *2*(4), 282. https://doi.org/10.4103/0975-7406.72127

Moore, E. G., Samuel, A. P. S., & Raymond, K. N. (2009). From antenna to assay: lessons learned in lanthanide luminescence. *Accounts of Chemical Research*, *42*(4), 542–552. https://doi.org/10.1021/ar800211j

Moreno-Vega, A. I., Gómez-Quintero, T., Nuñez-Anita, R. E., Acosta-Torres, L. S., & Castaño, V. (2012). Polymeric and ceramic nanoparticles in biomedical applications. In *Journal of Nanotechnology*. https://doi.org/10.1155/2012/936041

Najafi, F., & Sarbolouki, M. N. (2003). Biodegradable micelles/polymersomes from fumaric/sebacic acids and poly(ethylene glycol). In *Biomaterials* (Vol. 24, pp. 1175-82) doi: 10.1016/s0142-9612(02)00487-8.

Nascimento, M. A., Cruz, J. C., Rodrigues, G. D., de Oliveira, A. F., & Lopes, R. P. (2018). Synthesis of polymetallic nanoparticles from spent lithium-ion batteries and application in the removal of reactive blue 4 dye. *Journal of Cleaner Production*, *202*, 264–272. https://doi.org/10.1016/j.jclepro.2018.08.118

Nelson, N., Port, J., & Pandey, M. (2020). Use of Superparamagnetic Iron Oxide Nanoparticles (SPIONs) via Multiple Imaging Modalities and Modifications to Reduce Cytotoxicity: An Educational Review. *Journal of Nanotheranostics*, *1*(1), 105–135. https://doi.org/10.3390/jnt1010008

Nitz, M., Sherawat, M., Franz, K. J., Peisach, E., Allen, K. N., & Imperiali, B. (2004). Structural origin of the high affinity of a chemically evolved lanthanide-binding peptide. *Angewandte Chemie - International Edition*, *43*(28), 3682–3685. https://doi.org/10.1002/anie.200460028

Oh, W. K., Yoon, H., & Jang, J. (2010). Size control of magnetic carbon nanoparticles for drug delivery. *Biomaterials*, *31*(6), 1342–1348. https://doi.org/10.1016/j.biomaterials.2009.10.018

Olsvik, 0rjan, Popovic, T., Skjerve, E., Cudjoe, K. S., Hornes, E., Ugelstad, J., & Uhlen4, M. (1994). Magnetic Separation Techniques in Diagnostic Microbiology. In *Clinical Microbiology Reviews* (Vol. 7, Issue 1, pp. 43-54). doi: 10.1128/CMR.7.1.43.

Otsuka, H., Nagasaki, Y., & Kataoka, K. (2003). PEGylated nanoparticles for biological and pharmaceutical applications. In *Advanced Drug Delivery Reviews* (Vol. 55, Issue 3, pp. 403–419). Elsevier. https://doi.org/10.1016/S0169-409X(02)00226-0

Palombarini, F., Ghirga, F., Boffi, A., Macone, A., & Bonamore, A. (2019). Application of crossflow ultrafiltration for scaling up the purification of a recombinant ferritin. *Protein Expression and Purification* (V. 163). https://doi.org/10.1016/j.pep.2019.105451

Palombarini, F., Masciarelli, S., Incocciati, A., Liccardo, F., Di Fabio, E., Iazzetti, A., Fabrizi, G., Fazi, F., Macone, A., Bonamore, A., & Boffi, A. (2021). Self-assembling ferritin-dendrimer nanoparticles for targeted delivery of nucleic acids to myeloid leukemia cells. *Journal of Nanobiotechnology*, *19*(1). https://doi.org/10.1186/s12951-021-00921-5

Pan, K., & Zhong, Q. (2016). Organic Nanoparticles in Foods: Fabrication, Characterization, and Utilization. *Annual Review of Food Science and Technology*, *7*, 245–266. https://doi.org/10.1146/annurev-food-041715-033215

Pan, S., Cao, D., Huang, H., Yi, W., Qin, L., & Feng, M. (2013). A Serum-Resistant Low-Generation Polyamidoamine with PEI 423 Outer Layer for Gene Delivery Vector. *Macromolecular Bioscience*, *13*(4), 422–436. https://doi.org/10.1002/mabi.201200255

Pankhurst, Q. A., Connolly, J., Jones, S. K., & Dobson, J. (2003). Applications of magnetic nanoparticles in biomedicine. In *J. Phys. D: Appl. Phys* (Vol. 36). Doi: 10.1088/0022-3727/36/13/201

Patra, J. K., Das, G., Fraceto, L. F., Campos, E. V. R., Rodriguez-Torres, M. D. P., Acosta-Torres, L. S., Diaz-Torres, L. A., Grillo, R., Swamy, M. K., Sharma, S., Habtemariam, S., & Shin, H. S. (2018). Nano based drug delivery systems: Recent developments and future prospects. In *Journal of Nanobiotechnology* (Vol. 16, Issue 1). BioMed Central Ltd. https://doi.org/10.1186/s12951-018-0392-8

Peer, D., Karp, J. M., Hong, S., Farokhzad, C., Margalit, R., & Langer, R. (2007). Nanocarriers as an emerging platform for cancer therapy. *In Nature Nanotechnology* (V. 2 pp. 751-60) https://doi.org/10.1038/nnano.2007.387

Petcharoen, K., & Sirivat, A. (2012). Synthesis and characterization of magnetite nanoparticles via the chemical co-precipitation method. *Materials Science and Engineering B: Solid-State Materials for Advanced Technology*, *177*(5), 421–427. https://doi.org/10.1016/j.mseb.2012.01.003

Pham, H. N., Pham, T. H. G., Nguyen, D. T., Phan, Q. T., Le, T. T. H., Ha, P. T., Do, H. M., Hoang, T. M. N., & Nguyen, X. P. (2017). Magnetic inductive heating of organs of mouse models treated by copolymer coated Fe3O4 nanoparticles. *Advances in Natural Sciences: Nanoscience and Nanotechnology*, *8*(2). https://doi.org/10.1088/2043-6254/aa5e23

Piazza, R. D., Viali, W. R., Dos Santos, C. C., Nunes, E. S., Marques, R. F. C., Morais, P. C., Da Silva, S. W., Coaquira, J. A. H., & Jafelicci, M. (2020). PEGlatyon-SPION surface

functionalization with folic acid for magnetic hyperthermia applications. *Materials Research Express*, *7*(1). https://doi.org/10.1088/2053-1591/ab6700

Plank, C., Zelphati, O., & Mykhaylyk, O. (2011). Magnetically enhanced nucleic acid delivery. Ten years of magnetofection-Progress and prospects. In *Advanced Drug Delivery Reviews* (Vol. 63, Issues 14–15, pp. 1300–1331). https://doi.org/10.1016/j.addr.2011.08.002

Pratsinis, S. E., & Vemury, S. (1996). Particle formation in gases: a review. In *Powder Technology* (Vol. 88 pp. 267-273) https://doi.org/10.1016/S0032-5910(96)03130-0

Price, D. J., & Joshit, J. G. (1983). Ferritin. Binding of beryllium and other divalent metal ions. In *The Journal of Biological Chemistry* (Vol. 258, Issue 18) https://doi.org/10.1016/S0021-9258(17)44357-2

Rajput, S., Pittman, C. U., & Mohan, D. (2016). Magnetic magnetite (Fe_3O_4) nanoparticle synthesis and applications for lead (Pb^{2+}) and chromium (Cr^{6+}) removal from water. *Journal of Colloid and Interface Science*, *468*, 334–346. https://doi.org/10.1016/j.jcis.2015.12.008

Rastogi, R., Gulati, N., Kotnala, R. K., Sharma, U., Jayasundar, R., & Koul, V. (2011). Evaluation of folate conjugated pegylated thermosensitive magnetic nanocomposites for tumor imaging and therapy. *Colloids and Surfaces B: Biointerfaces*, *82*(1), 160–167. https://doi.org/10.1016/j.colsurfb.2010.08.037

Richardson, F. S. (1982). Terbium(III) and Europium(III) Ions as Luminescent Probes and Stains for Biomolecular Systems. In *Chemical Reviews* (V. 82, pp. 541-552) https://doi.org/10.1021/cr00051a004

Riehemann, K., Schneider, S. W., Luger, T. A., Godin, B., Ferrari, M., & Fuchs, H. (2009). Nanomedicine - Challenge and perspectives. In *Angewandte Chemie - International Edition* (Vol. 48, Issue 5, pp. 872–897). https://doi.org/10.1002/anie.200802585

Rosa, L., Blackledge, J., & Boretti, A. (2017). Nano-magnetic resonance imaging (Nano-MRI) gives personalized medicine a new perspective. *Biomedicines*, *5*(1). https://doi.org/10.3390/biomedicines5010007

Rosen, J. E., Chan, L., Shieh, D. Bin, & Gu, F. X. (2012). Iron oxide nanoparticles for targeted cancer imaging and diagnostics. In *Nanomedicine: Nanotechnology, Biology, and Medicine* (Vol. 8, Issue 3, pp. 275–290). https://doi.org/10.1016/j.nano.2011.08.017

Ryu, J. H., Lee, S., Son, S., Kim, S. H., Leary, J. F., Choi, K., & Kwon, I. C. (2014). Theranostic nanoparticles for future personalized medicine. In *Journal of Controlled*

Release (Vol. 190, pp. 477–484). Elsevier B.V. https://doi.org/10.1016/j.jconrel.2014.04.027

Sammarco, M. C., Ditch, S., Banerjee, A., & Grabczyk, E. (2008). Ferritin L and H subunits are differentially regulated on a post-transcriptional level. *Journal of Biological Chemistry*, *283*(8), 4578–4587. https://doi.org/10.1074/jbc.M703456200

Sana, B., Johnson, E., Magueres, P. Le, Criswell, A., Cascio, D., & Lim, S. (2013). The role of nonconserved residues of archaeoglobus fulgidus ferritin on its unique structure and biophysical properties. *Journal of Biological Chemistry*, *288*(45), 32663–32672. https://doi.org/10.1074/jbc.M113.491191

Sato, D., Ohtomo, H., Yamada, Y., Hikima, T., Kurobe, A., Fujiwara, K., & Ikeguchi, M. (2016). Ferritin Assembly Revisited: A Time-Resolved Small-Angle X-ray Scattering Study. *Biochemistry*, *55*(2), 287–293. https://doi.org/10.1021/acs.biochem.5b01152

Schoepf, U., Marecos, E. M., Melder, R. J., Jain, R. K., & Weissleder, R. (1998). Intracellular magnetic labeling of lymphocytes for in vivo trafficking studies. In *Biotechniques* (V. 24, pp. 642-651) doi: 10.2144/98244rr01.

Scialabba, C., Puleio, R., Peddis, D., Varvaro, G., Calandra, P., Cassata, G., Cicero, L., Licciardi, M., & Giammona, G. (2017). Folate targeted coated SPIONs as efficient tool for MRI. *Nano Research*, *10*(9), 3212–3227. https://doi.org/10.1007/s12274-017-1540-4

Sculimbrene, B. R., & Imperiali, B. (2006). Lanthanide-binding tags as luminescent probes for studying protein interactions. *Journal of the American Chemical Society*, *128*(22), 7346–7352. https://doi.org/10.1021/ja061188a

Selvin, P. R. (2002). Principles and biophysical applications of lanthanide-based probes. In *Annual Review of Biophysics and Biomolecular Structure* (Vol. 31, pp. 275–302). https://doi.org/10.1146/annurev.biophys.31.101101.140927

Sharifi, S., Seyednejad, H., Laurent, S., Atyabi, F., Saei, A. A., & Mahmoudi, M. (2015). Superparamagnetic iron oxide nanoparticles for in vivo molecular and cellular imaging. In *Contrast Media and Molecular Imaging* (Vol. 10, Issue 5, pp. 329–355). John Wiley and Sons Ltd. https://doi.org/10.1002/cmmi.1638

Shi, J., Kantoff, P. W., Wooster, R., & Farokhzad, O. C. (2017). Cancer nanomedicine: Progress, challenges and opportunities. In *Nature Reviews Cancer* (Vol. 17, Issue 1, pp. 20–37). Nature Publishing Group. https://doi.org/10.1038/nrc.2016.108

Shubayev, V. I., Pisanic, T. R., & Jin, S. (2009). Magnetic nanoparticles for theragnostics. In *Advanced Drug Delivery Reviews* (Vol. 61, Issue 6, pp. 467–477). https://doi.org/10.1016/j.addr.2009.03.007

Silly, M. G., Blanchandin, S., Sirotti, F., Lux, F., Chevreux, S., Lemercier, G., & Charra, F. (2013). Evidence of mixed-valence hydrated europium-chloride phase in vacuum by means of optical and electronic spectroscopies. *Journal of Physical Chemistry C*, *117*(19), 9766–9771. https://doi.org/10.1021/jp312500f

Silva, B., & Faustino, P. (2015). An overview of molecular basis of iron metabolism regulation and the associated pathologies. In *Biochimica et Biophysica Acta - Molecular Basis of Disease* (Vol. 1852, Issue 7, pp. 1347–1359). Elsevier B.V. https://doi.org/10.1016/j.bbadis.2015.03.011

Sindrewicz, P., Li, X., Yates, E. A., Turnbull, J. E., Lian, L. Y., & Yu, L. G. (2019). Intrinsic tryptophan fluorescence spectroscopy reliably determines galectin-ligand interactions. *Scientific Reports*, *9*(1). https://doi.org/10.1038/s41598-019-47658-8

Sjögren, C. E., Johansson, C., Nevestad, A., Sontum, P. C., Briley-Saebø, K., & Fahlvik, A. K. (1997). Crystal size and properties of superparamagnetic iron oxide (SPIO) particles. In *Magn Reson Imaging* (Vol. 15, Issue 1, pp. 55-67). doi: 10.1016/s0730-725x(96)00335-9.

Slowing, I. I., Vivero-Escoto, J. L., Wu, C. W., & Lin, V. S. Y. (2008). Mesoporous silica nanoparticles as controlled release drug delivery and gene transfection carriers. In *Advanced Drug Delivery Reviews* (Vol. 60, Issue 11, pp. 1278–1288). https://doi.org/10.1016/j.addr.2008.03.012

Song, H. P., Yang, J. Y., Lo, S. L., Wang, Y., Fan, W. M., Tang, X. S., Xue, J. M., & Wang, S. (2010). Gene transfer using self-assembled ternary complexes of cationic magnetic nanoparticles, plasmid DNA and cell-penetrating tat peptide. *Biomaterials*, *31*(4), 769–778. https://doi.org/10.1016/j.biomaterials.2009.09.085

Stefanini, S., Chiancone, E., Antonini, E., & Finazzi-Agrot, A. (1983). Binding of Terbium to Apoferritin: A Fluorescence Study. In *Archives of Biochemistry and Biophysics* (Vol. 222, Issue 2, pp. 430-4) doi: 10.1016/0003-9861(83)90541-6.

Stefanini, S., Vecchini, P., & Chiancone, E. (1987). On the Mechanism of Horse Spleen Apoferritin Assembly: A Sedimentation Velocity and Circular Dichroism Study. In *Biochemistry* (Vol. 26, pp. 1831-7). doi: 10.1021/bi00381a007.

Stillman, T. J., Hempstead, P. D., Artymiuk, P. J., Andrews, S. C., Hudson, A. J., Treffry, A., Guest, J. R., & Harrison, P. M. (2001). The high-resolution X-ray crystallographic

structure of the ferritin (EcFtnA) of Escherichia coli; comparison with human H ferritin (HuHF) and the structures of the Fe^{3+} and Zn^{2+} derivatives. *Journal of Molecular Biology*, *307*(2), 587–603. https://doi.org/10.1006/jmbi.2001.4475

Storm, G., Belliot, S. 0, Daemenb, T., & Lasic, D. D. (1995). Surface modification of nanoparticles to oppose uptake by the mononuclear phagocyte system. In *Advanced Drug Delivery Reviews* (Vol. 17, pp. 31-48). https://doi.org/10.1016/0169-409X(95)00039-A

Sun, C., Yang, H., Yuan, Y., Tian, X., Wang, L., Guo, Y., Xu, L., Lei, J., Gao, N., Anderson, G. J., Liang, X. J., Chen, C., Zhao, Y., & Nie, G. (2011). Controlling assembly of paired gold clusters within apoferritin nanoreactor for in vivo kidney targeting and biomedical imaging. *Journal of the American Chemical Society*, *133*(22), 8617–8624. https://doi.org/10.1021/ja200746p

Sun, S., Murray, C. B., Weller, D., Folks, L., & Moser, A. (2000). Monodisperse FePt nanoparticles and ferromagnetic FePt nanocrystal superlattices. *Science*, *287*(5460), 1989–1992. https://doi.org/10.1126/science.287.5460.1989

Swift, J., Butts, C. A., Cheung-Lau, J., Yerubandi, V., & Dmochowski, I. J. (2009). Efficient Self-Assembly of *Archaeoglobus fulgidus* ferritin around metallic cores. *Langmuir*, *25*(9), 5219–5225. https://doi.org/10.1021/la8040743

Takagi, H., Shi, D., Ha, Y., Allewell, N. M., & Theil, E. C. (1998). Localized Unfolding at the Junction of Three Ferritin Subunits. A mechanism for iron release? *In J Biol Chem.* (V. 273, pp. 18685-8) doi: 10.1074/jbc.273.30.18685.

Tanner, P. A., Zhou, L., Duan, C., & Wong, K. L. (2018). Misconceptions in electronic energy transfer: bridging the gap between chemistry and physics. *Chemical Society Reviews*, *47*(14), 5234–5265. https://doi.org/10.1039/c8cs00002f

Tian, L., Dai, Z., Liu, X., Song, B., Ye, Z., & Yuan, J. (2015). Ratiometric Time-Gated Luminescence Probe for Nitric Oxide Based on an Apoferritin-Assembled Lanthanide Complex-Rhodamine Luminescence Resonance Energy Transfer System. *Analytical Chemistry*, *87*(21), 10878–10885. https://doi.org/10.1021/acs.analchem.5b02347

Torchilin, V. P. (2001). Structure and design of polymeric surfactant-based drug delivery systems. In *Journal of Controlled Release* (Vol. 73 pp.137-72) doi: 10.1016/s0168-3659(01)00299-1.). www.elsevier.com/locate/jconrel

Tortorella, S., & Karagiannis, T. C. (2014). Transferrin receptor-mediated endocytosis: A useful target for cancer therapy. In *Journal of Membrane Biology* (Vol. 247, Issue 4, pp. 291–307). Springer New York LLC. https://doi.org/10.1007/s00232-014-9637-0

Toshima, N., & Yonezawa, T. (1998). Bimetallic nanoparticles - Novel materials for chemical and physical applications. *New Journal of Chemistry*, *22*(11), 1179–1201. https://doi.org/10.1039/a805753b

Tourinho, F.A., Franck, R. & Massart, R. (1990). Aqueous ferrofluids based on manganese and cobalt ferrites. In *Journal of Materials Science*, 25, 3249–3254. https://doi.org/10.1007/BF00587682

Treffry, A., & Harrison, P. M. (1984). Spectroscopic Studies on the Binding of Iron, Terbium, and Zinc by Apoferritin. In Journal of Inorganic Biochemistry (V. 21, pp. 9-20) https://doi.org/10.1016/0162-0134(84)85035-7

Truffi, M., Fiandra, L., Sorrentino, L., Monieri, M., Corsi, F., & Mazzucchelli, S. (2016). Ferritin nanocages: A biological platform for drug delivery, imaging and theranostics in cancer. In *Pharmacological Research* (Vol. 107, pp. 57–65). Academic Press. https://doi.org/10.1016/j.phrs.2016.03.002

Vangijzegem, T., Stanicki, D., & Laurent, S. (2019). Magnetic iron oxide nanoparticles for drug delivery: applications and characteristics. In *Expert Opinion on Drug Delivery* (Vol. 16, Issue 1, pp. 69–78). Taylor and Francis Ltd. https://doi.org/10.1080/17425247.2019.1554647

Vetri, V., D'Amico, M., Foderà, V., Leone, M., Ponzoni, A., Sberveglieri, G., & Militello, V. (2011). Bovine Serum Albumin protofibril-like aggregates formation: Solo but not simple mechanism. *Archives of Biochemistry and Biophysics*, *508*(1), 13–24. https://doi.org/10.1016/j.abb.2011.01.024

Vogelsberger, W. (2003). Thermodynamic and Kinetic Considerations of the Formation and the Dissolution of Nanoparticles of Substances Having Low Solubility. *Journal of Physical Chemistry B*, *107*(36), 9669–9676. https://doi.org/10.1021/jp030347z

Wang, X., Wei, F., Liu, A., Wang, L., Wang, J. C., Ren, L., Liu, W., Tu, Q., Li, L., & Wang, J. (2012). Cancer stem cell labeling using poly(l-lysine)-modified iron oxide nanoparticles. *Biomaterials*, *33*(14), 3719–3732. https://doi.org/10.1016/j.biomaterials.2012.01.058

Wang, Y. X. J., Hussain, S. M., & Krestin, G. P. (2001). Superparamagnetic iron oxide contrast agents: Physicochemical characteristics and applications in MR imaging. *European Radiology*, *11*(11), 2319–2331. https://doi.org/10.1007/s003300100908

Wang, Y.-X. J. (2011). Superparamagnetic iron oxide based MRI contrast agents: Current status of clinical application. *Quantitative Imaging in Medicine and Surgery*, *1*(1), 35–40. https://doi.org/10.3978/j.issn.2223-4292.2011.08.03

Wang, Z., Gao, H., Zhang, Y., Liu, G., Niu, G., & Chen, X. (2017). Functional ferritin nanoparticles for biomedical applications. In *Frontiers of Chemical Science and Engineering* (Vol. 11, Issue 4, pp. 633–646). Higher Education Press. https://doi.org/10.1007/s11705-017-1620-8

Watkins, R., Wu, L., Zhang, C., Davis, R. M., & Xu, B. (2015). Natural product-based nanomedicine: Recent advances and issues. In *International Journal of Nanomedicine* (Vol. 10, pp. 6055–6074) https://doi.org/10.2147/IJN.S92162

Weissleder, R., Cheng, H.-C., Bogdanova, A., & Bogdanov, A. (2005). Magnetically labeled cells can be detected by MR imaging. In Journal of Magnetic Resonance Imaging (V. 7 pp. 258-263) https://doi.org/10.1002/jmri.1880070140

Werts, M. H. V. (2005). Making sense of lanthanide luminescence. *In Science Progress* (V. 88 pp. 101-131) doi: 10.3184/003685005783238435.

Wierzbinski, K. R., Szymanski, T., Rozwadowska, N., Rybka, J. D., Zimna, A., Zalewski, T., Nowicka-Bauer, K., Malcher, A., Nowaczyk, M., Krupinski, M., Fiedorowicz, M., Bogorodzki, P., Grieb, P., Giersig, M., & Kurpisz, M. K. (2018). Potential use of superparamagnetic iron oxide nanoparticles for in vitro and in vivo bioimaging of human myoblasts. *Scientific Reports*, *8*(1). https://doi.org/10.1038/s41598-018-22018-0

Wittmaack, K. (2007). In search of the most relevant parameter for quantifying lung inflammatory response to nanoparticle exposure: Particle number, surface area, or what? *Environmental Health Perspectives*, *115*(2), 187–194. https://doi.org/10.1289/ehp.9254

Xu, J., Yang, H., Fu, W., Du, K., Sui, Y., Chen, J., Zeng, Y., Li, M., & Zou, G. (2007). Preparation and magnetic properties of magnetite nanoparticles by sol-gel method. *Journal of Magnetism and Magnetic Materials*, *309*(2), 307–311. https://doi.org/10.1016/j.jmmm.2006.07.037

Yang, C., Fu, L. M., Wang, Y., Zhang, J. P., Wong, W. T., Ai, X. C., Qiao, Y. F., Zou, B. S., & Gui, L. L. (2004). A highly luminescent europium complex showing visible-light-sensitized red emission: Direct observation of the singlet pathway. *Angewandte Chemie - International Edition*, *43*(38), 5010–5013. https://doi.org/10.1002/anie.200454141

Yeh, T.-C., & Zhang, W. (1993). *Intracellular Labeling of T-Cells with Superparamagnetic Contrast Agents*. In Magn Reson Med. (V. 30, pp. 617-25) doi: 10.1002/mrm.1910300513.

Yu, M. K., Park, J., & Jon, S. (2012). Targeting strategies for multifunctional nanoparticles in cancer imaging and therapy. In *Theranostics* (Vol. 2, Issue 1, pp. 3–44). https://doi.org/10.7150/thno.3463

Yuan, X., Zhang, X., Sun, L., Wei, Y., & Wei, X. (2019). Cellular Toxicity and Immunological Effects of Carbon-based Nanomaterials. In *Particle and Fibre Toxicology* (Vol. 16, Issue 1). https://doi.org/10.1186/s12989-019-0299-z

Zarepour, A., Zarrabi, A., & Khosravi, A. (2017). SPIONs as Nano-Theranostics Agents. Springer

Zhang, Z., Hu, Y., Yang, J., Xu, Y., Zhang, C., Wang, Z., Shi, X., & Zhang, G. (2016). Facile Synthesis of Folic Acid-Modified Iron Oxide Nanoparticles for Targeted MR Imaging in Pulmonary Tumor Xenografts. *Molecular Imaging and Biology*, *18*(4), 569–578. https://doi.org/10.1007/s11307-015-0918-5

Zhao, L., Song, W., Wang, J., Yan, Y., Chen, J., & Liu, R. (2015). Mechanism of Dimercaptosuccinic Acid Coated Superparamagnetic Iron Oxide Nanoparticles with Human Serum Albumin. *Journal of Biochemical and Molecular Toxicology*, *29*(12), 579–586. https://doi.org/10.1002/jbt.21731

Zhen, Z., Tang, W., Guo, C., Chen, H., Lin, X., Liu, G., Fei, B., Chen, X., Xu, B., & Xie, J. (2013). Ferritin nanocages to encapsulate and deliver photosensitizers for efficient photodynamic therapy against cancer. *ACS Nano*, *7*(8), 6988–6996. https://doi.org/10.1021/nn402199g

Zhu, L., Zhou, Z., Mao, H., & Yang, L. (2017). Magnetic nanoparticles for precision oncology: Theranostic magnetic iron oxide nanoparticles for image-guided and targeted cancer therapy. In *Nanomedicine* (Vol. 12, Issue 1, pp. 73–87). Future Medicine Ltd. https://doi.org/10.2217/nnm-2016-0316

Zou, W., Liu, X., Zhao, X., Wang, J., Chen, D., Li, J., Ji, L., & Hua, Z. (2016). Expression, purification, and characterization of recombinant human L-chain ferritin. In *Protein Expression and Purification*, *119*, 63–68. https://doi.org/10.1016/j.pep.2015.11.018